Test of the Equivalence Principle in an Einstein Elevator

Annual Report #1

NASA Grant NAG8-1780

For the period 30 April 2001 through 28 February 2002

Principal Investigator

Irwin I. Shapiro

May 2002

The Smithsonian Astrophysical Observatory
is a member of the
Harvard-Smithsonian Center for Astrophysics

Test of the Equivalence Principle in an Einstein Elevator

Annual Report #1

For the period 30 April 2001 through 28 February 2002

Principal Investigator

Irwin I. Shapiro

Co-Investigators

S. Glashow
E.C. Lorenzini
M.L. Cosmo
P. Cheimets
N. Finkelstein (E/PO)
M. Schneps (E/PO)

Ph.D. Students

A. Turner
C. Bombardelli
G. Parzianello

Non-US Collaborating PI

V. Iafolla (IFSI/CNR)

May 2002

The Smithsonian Astrophysical Observatory
is a member of the
Harvard-Smithsonian Center for Astrophysics

TABLE OF CONTENTS

INTRODUCTION

The scientific goal of the experiment is to test the equality of gravitational and inertial mass (i.e., to test the Principle of Equivalence) by measuring the independence of the rate of fall of bodies from the composition of the falling body. The measurement is accomplished by measuring the relative displacement (or equivalently acceleration) of two falling bodies of different materials which are the proof masses of a differential accelerometer. The goal of the experiment is to measure the Eötvös ratio $\delta g/g$ (differential acceleration/common acceleration) with an accuracy goal of a few parts in 10^{15}. The estimated accuracy is about two orders of magnitude better than the present state of the art. The experiment is a null experiment in which a result different from zero will indicate a violation of the Equivalence Principle.

The main goal of the study to be carried out under this grant is the flight definition of the experiment and bread boarding of critical components of the experiment that will enable us to be ready for the following phases of the project. The project involves an international cooperation in which the responsibility of the US side is the flight definition of the experimental facility while the responsibility of the non-US partners is the flight definition and laboratory prototyping of the differential acceleration detector.

In summary, the experiment to be designed is for taking differential acceleration measurements with a high-sensitivity detector (the sensor) during free fall conditions lasting up to 30 s in a disturbance-free acceleration environment. The experiment strategy consists in letting the sensor free fall inside a few meters long (in the vertical direction) evacuated capsule that is falling simultaneously in the rarefied atmosphere after release from a helium balloon flying at a stratospheric altitude.

DESCRIPTION OF EXPERIMENT CONCEPT

Need for Picogravity Environment

The accuracy of the Weak Equivalence Principle (WEP) tests with laboratory proof masses on the ground is limited by the Earth's seismic noise and the weakness of suitable signal sources. Previous experiments include the famous torsion balance experiments of Eötvös (1890-1922)[i] [ii] as well as the classical tests of the Equivalence Principle by Roll-Krotkov-Dicke (1964)[iii] utilizing a torsion balance which had an accuracy of 3 parts in 10^{11} and the I.I. Shapiro et al. (1976)[iv] and Williams et al. (1976)[v] lunar laser ranging experiment with an accuracy of 3 parts in 10^{12}. The present state of the art is at a few parts in 10^{13} both for lunar laser ranging tests (Williams et al., 1996)[vi] and for torsion balance tests (Adelberger et al., 1999)[vii].

By conducting the experiment in free fall, the signal strength increases by about three orders of magnitude because the full strength of the Earth's gravity is sensed in free fall. Seismic noise is also absent in free fall. Seismic noise is replaced in orbit by the noise

sources of the space environment which require drag free stages or drag compensation in order to achieve the promised improvements in the test accuracy. An orbital free fall, with a "drag-free" satellite, is one approach that has been under development for many years. A small number of orbital tests of the WEP has been proposed with estimated accuracies of 10^{-15} [viii], 10^{-17} [ix], and 10^{-18} [x]. An alternative to the free fall in space is the vertical free fall inside a drag-shielding capsule released from a balloon at a stratospheric altitude as proposed in this experiment[xi].

An orbital free-fall has advantages and disadvantages with respect to vertical free fall. On the one hand, orbital free-fall tests can achieve an even higher accuracy than vertical free-fall tests thanks to the longer integration time and lower resonance frequency of the detector. On the other hand, vertical free fall tests have some key advantages over orbital tests. First of all, in a vertical free fall (from a balloon) the experiment can be repeated at relatively short intervals of time (a few weeks) and at a more affordable cost. The ability to repeat the experiment is important for the success because these high-accuracy differential detectors can not be tested on the ground at the accuracy that they can achieve in free fall conditions. Therefore, modifications and improvements have to be expected before the detector/experiment performs at the estimated free-fall accuracy.

Both orbital and vertical free fall are Galilean experiments in which the differential displacement or rate of fall or acceleration is measured between two bodies of different materials falling in a gravitational field. However, classic Galilean experiments, in which the relative displacement of two bodies falling side by side is measured (with drops ranging from 1m to 140m) have yielded an accuracy[xii] in testing the WEP of order 10^{-10}. The limitation mostly stems from relative errors in initial conditions at release which propagate over time due to gravity gradients. This problem can be overcome in orbital and long vertical free falls (i.e., from stratospheric heights) thanks to two provisions: (1) the initial relative motion of the two sensing masses inside the detector is abated during a damping phase preceding the measurement phase and (2) the detector is rotated with respect to the gravity field in order to modulate the signal (at a frequency f_s) and move the frequency of the effect of key gravity gradient components to $2f_s$.

The test of the Equivalence Principle requires a differential measurement of acceleration. This fact has a positive consequence in terms of the rejection of accelerations that affect the two proof masses equally (common-mode type) and their effects on the differential acceleration. Typical values of the common-mode rejection factor of differential accelerometers are of order 10^{-4}. Consequently, for an experiment that aims at measuring differential acceleration of order 10^{-15} g, the acceleration perturbations external to the detector must be of order 10^{-12} g or less.

Drop Facility

The following is a preliminary description of the drop facility the design of which will evolve as a result of the analyses carried out during the flight definition phase. The free fall facility (see Fig. 1) consists of: (1) the *gondola* that stays attached to the balloon; (2) a leveling mechanism that keeps the capsule vertical before release; (3) the *capsule*, which houses a large vacuum chamber/cryostat; (4) the *instrument package* which free

falls inside the cryostat and contains a small, high-vacuum chamber which in turn houses the detector; and (5) the *parachute system* to decelerate the capsule at the end of the free fall run.

The capsule is kept vertically leveled and stabilized in azimuth by the gondola before release. Upon reaching an altitude higher than 40 km, the capsule is released from the gondola and immediately afterwards ($\leq$ 1 s) the instrument package is released from the top of the capsule. The analysis indicates (see later on) that with a 1-3 m long vertical space available inside the capsule, the instrument package will span that space in 25-30 s while the capsule, that is slightly decelerated by the rarefied atmosphere, falls by a few km over the same time. The capsule shields the instrument package from external perturbations and allows it to free fall under acceleration conditions which are close to ideal. The differential accelerations between the two falling test masses are measured during the free fall time. At the end of the free-fall run the capsule is decelerated by a parachute system for recovery in water or over land.
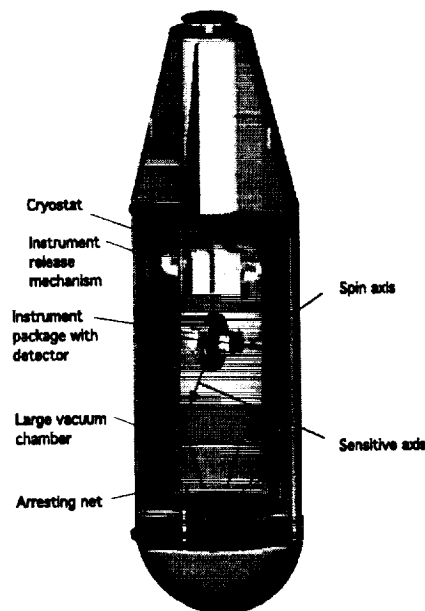
Figure 1 Pre-definition-study configuration of capsule in free fall after detector release

Detector

The following is a preliminary description of the differential acceleration detector, the design of which (carried out in cooperation with our non-US partners) will evolve as a result of the analyses conducted during the flight definition phase.

The detector that we plan to use for the experiment is a differential accelerometer that will be developed at the Institute of Space Physics (IFSI) in Rome (Italy), under the sponsorship of the Italian Space Agency in the framework of the participation in this project of non-US investigators (V. Iafolla, PI). This detector technology[xiii] has been pioneered by V. Iafolla and the late F. Fuligni and applied to the construction of a number

4

of high-sensitivity, low-frequency accelerometers over several years. In the following we give a brief description of the detector conceptual design at this stage of the project.

The differential-acceleration detector (see Fig. 2) measures the relative displacement, along the sensitive axis, between two sensing masses of different materials. The centers of mass of the sensing masses are made to coincide within the attainable values in order to minimize the effect of gravity gradients, rotational motions and linear accelerations upon the differential output signal.
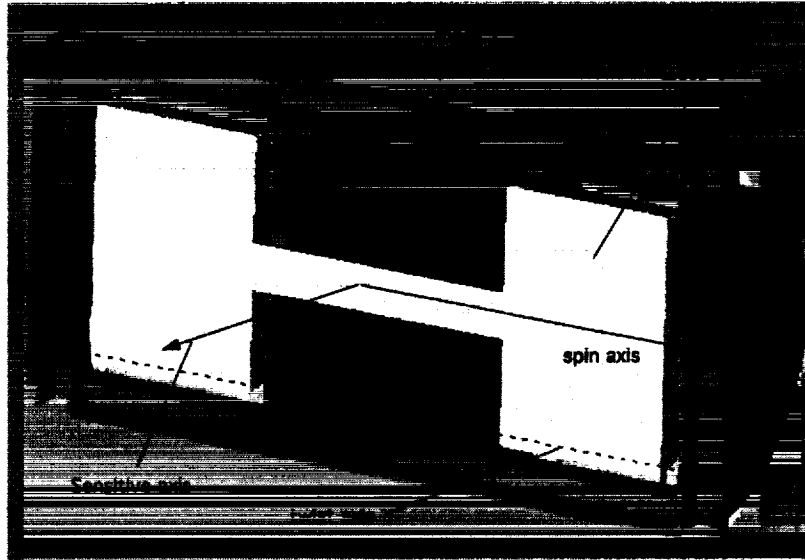
Figure 2 Longitudinal section of instrument and sensing masses.

The two sensing masses are constrained by torsion springs to rotate independently about the twist axis (which is parallel to the spin axis of the instrument) and their resonant frequencies are electrostatically controlled for frequency matching. The displacements generated by the rotations are sensed by the capacitive pick-ups of the instrument as explained later on. Sensing mass 1 (in dark color) is a hollow cylinder mostly made of a given material while sensing mass 2 (in light color) is a dumbbell-shaped cylinder made of a different material. Each sensing mass constitutes the moving part of a capacitor with symmetric fixed plates on either side of the sensing mass (see Fig. 3). Capacitor 1 is formed by sensing mass 1 and the fixed plates marked A and B while capacitor 2 is formed by sensing mass 2 and the fixed plates marked C and D. The fixed plates A and C are used for signal pick-up and the fixed plates B and D for feed-back control. The displacement of sensing mass 1, for example, is detected by the series capacitances As (one fixed plate on each side of the sensing mass). These plates form one branch of a capacitive bridge in which two additional reference capacitors form the other branch. The bridge is pumped by a quartz oscillator at a stable frequency of 10-20 kHz, reducing the relevant noise temperature of the preamplifier. The difference between the output signals from capacitors 1 and 2 is amplified by a low-noise preamplifier, sent to a lock-in amplifier for phase-detection, and then to a low-pass filter.

The cross sections of the ellipsoids of inertia about the spin axis of the instrument are circular so as to minimize, within the construction tolerance, the mass-moment torques[xiv]. In the detector shown in Figs. 2 and 3, the inner cylindrical mass is made mostly of a high-density material (e.g., Platinum-Iridium) while the outer dumbbell-mass is made of a low-density material (e.g., Aluminum).

Figure 3 Interior of differential acceleration detector.

In order to achieve an experimental accuracy of a few parts in 10^{15} in about 25-30 s integration time, the detector must have an intrinsic noise (expressed in terms of acceleration) of less than 10^{-14} $g/Hz^{1/2}$. Earlier analyses indicate that this level of noise is attainable with an instrument refrigerated to a temperature close to that of liquid Helium and with state-of-the-art low-noise preamplifiers.

Experiment Sequence and Communication Links

Figure 4 shows the preliminary timetable of the experiment sequence. The experiment starts with the loading of the sensor into the vacuum chamber/cryostat about 2 weeks before the planned launch. This operation is then followed by the pumping down of the chamber and the refrigeration of the sensor. After connecting the capsule to the gondola and the balloon, the balloon is launched. The estimated time to reach altitude is of order 3 hours. Upon reaching altitude, the attitude of the capsule is stabilized by the leveling mechanism on the gondola, the sensor is spun up, and the dynamics of the system is analyzed. When the dynamics is within the acceptable bounds, the capsule is released from the gondola and the sensor is released from the top of the chamber/cryostat immediately afterwards. The science data is taken during the free-fall phase in which the sensor spans the length of the chamber. Shortly after the sensor has reached the bottom of the capsule, the blut (first stage of the deceleration system) is released and, when the speed has decreased below the required value, the parachute is deployed. The chamber is vented before the capsule hits the surface/water and the locator beacon is turned on.

6

Event	Prelaunch					
	T-2wks				T-1Day	Launch
Mount Sensor in Chamber						
Close Chamber						
Pump Down Chamber						
Chill Sensor						
Connect to Balloon						
Launch						

	To Float					
	T+30m	T+60m	T+90m	T+120m	T+150m	T+180m
Rise to Altitude						
Study Dynamic conditions						
Spin up Sensor						
Check out full comm path						

	Release		Measurement			
	R+1s	R+2s	R+10s	R+20s	R+25s	R+30s
Release Capsule						
Release Sensor						
Take Data						
Sensor at Bottom of Capsule						

	Post Measurement Fall					
	R+40s	R+70s	R+100s	R+130s	R+150s	R+TBD
Release Blut						
Fall under Blut Drag						
Release Main Chute						
Fall under Chute Drag						
Vent Capsule						
Deploy Landing Isolators						
Turn on Locator Beacons						
Touchdown						
Valve down balloon						

Figure 4 Preliminary timeline of experiment

Figure 5 is a schematic of the communication system between the ground, the gondola and the capsule through radio links and the communication between the sensor (during free fall) and the capsule through an infra-red link.
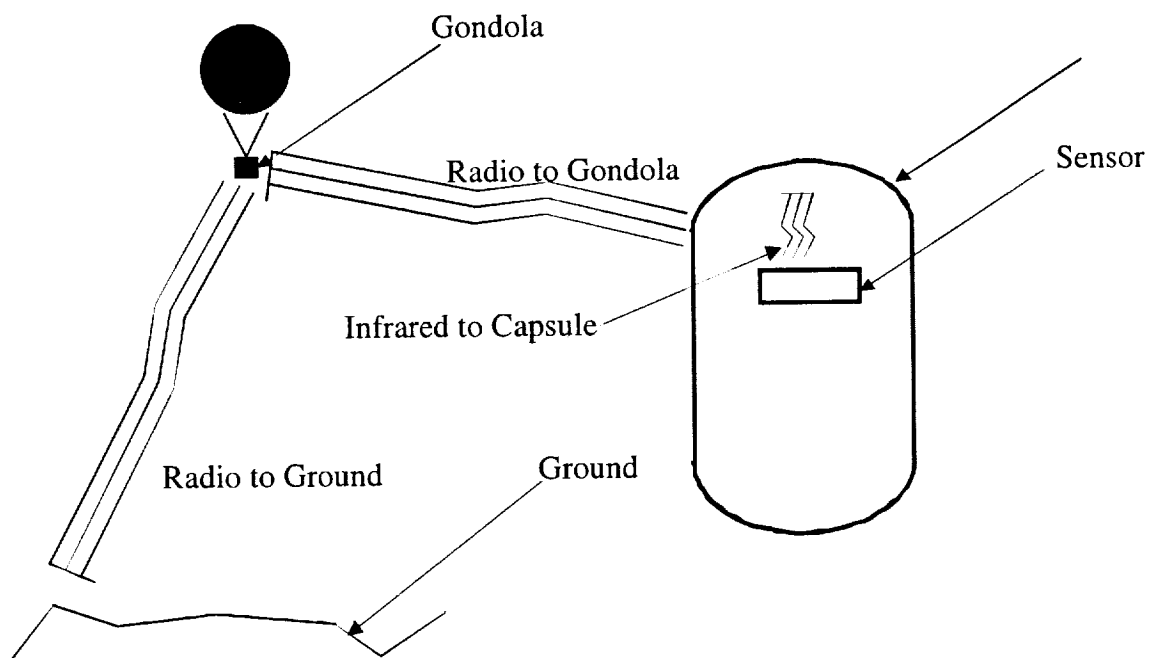
Figure 5 Schematic of communication links.

ANALYSIS OF FREE FALL PHASE

The free fall time of the instrument package inside the capsule can be computed after considering that the capsule is slowly decelerated by the air drag while the instrument package (after release) moves inside the vacuum chamber at low relative speed and consequently it is unaffected by air drag (it is indeed in free-fall conditions).

Free fall time

The free fall time and vertical size of the vacuum chamber/cryostat can be computed from the equations of motion of the instrument package in free fall and the capsule in decelerated fall. The equations of motion are as follows:

$$\ddot{z}_1 = g$$

$$\ddot{z}_2 = g - \frac{1}{2m_2} C_D S \rho \dot{z}_2^2 \tag{1}$$

where z is the vertical distance from the time of release (the subscript 1 stands for instrument package and 2 for capsule), S is the frontal cross section of the capsule, C_D the air drag coefficient of the capsule and $\rho = f(h)$ is the air density with h the altitude above the Earth's surface. Equations (1) can be solved analytically only if C_D is assumed constant and the atmospheric density exponential. We will not spend time on the analytic solution because it is valid only for relatively-short drops.
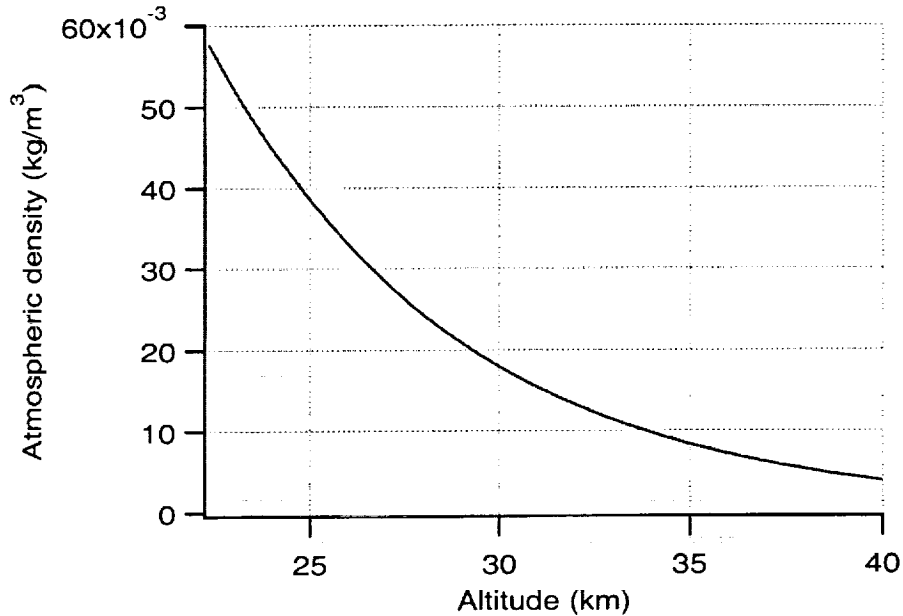
Figure 6 Atmospheric density in the stratosphere per US Standard Atmosphere 1976

9

After adopting a density profile from the US Standard 1976 Atmospheric Model (as shown in Fig. 6) the exponential fit of the density for the altitudes of interest is:

$$\rho = \rho_0 e^{-h/H} \tag{2}$$

Where H is the scale height, ρ_0 is the reference density which is taken at the Earth's surface and h the altitude above the Earth's surface. The relative distance can be obtained as the double integral of the acceleration difference between the capsule and the instrument package $\delta\ddot{z} = \ddot{z}_2 - \ddot{z}_1$ which is equal to the deceleration of the capsule due to aerodynamic drag:

$$\delta\ddot{z} = \frac{1}{2}\frac{\rho_0}{\beta}e^{(z-h_D)/H}g^2t^2 \tag{3}$$

where $\beta = m/(C_D S)$ is the frontal ballistic coefficient of the capsule, h_D is the drop altitude, $z \approx (1/2)gt^2$ the distance traveled by the capsule and g the Earth's gravitational acceleration. The drop velocity of the capsule is assumed equal to the free fall velocity gt *only* for the purpose of computing the air drag deceleration (which is a valid approximation at high altitudes).

The air drag coefficient C_D is fairly constant in the non-compressible regime but then it grows substantially with the Mach number for speeds approaching the transonic regime as shown in Fig. 7 for an aerodynamically-shaped cylinder with fineness ratio $D/L = \delta \approx 0.25$. The Mach number M is the ratio between the actual speed of the capsule and the speed of sound at the local altitude:

$$M = \frac{V}{\sqrt{\gamma RT}} \tag{4}$$

where R = 287 J/(kg-K) is the gas constant of air, T the local air temperature and $\gamma \approx 1.4$. The Mach number vs. the drop time is shown in Fig. 8 together with the drop distance vs. time.

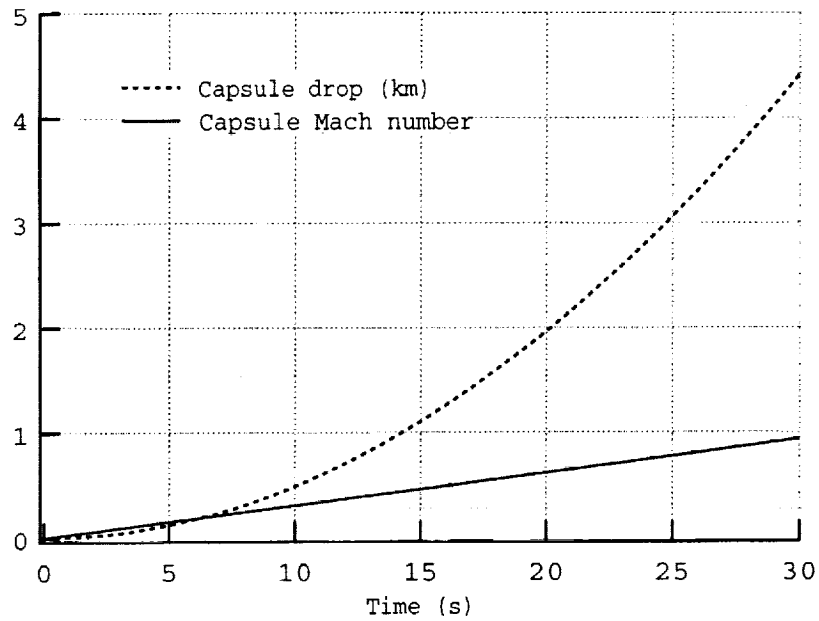As a result of the functional dependence $C_D = f(\text{Mach})$, we can separate the ballistic coefficient into two components as follows:

$$\beta = \beta_0(1 + \Delta\hat{\beta}) \tag{5}$$

where $\beta_0 = m/(C_{D0}A)$ is the low-speed ballistic coefficient (i.e., its minimum value) and $\Delta\hat{\beta}$ is the fractional variation of the ballistic coefficient due to the increase of the Mach number.

10
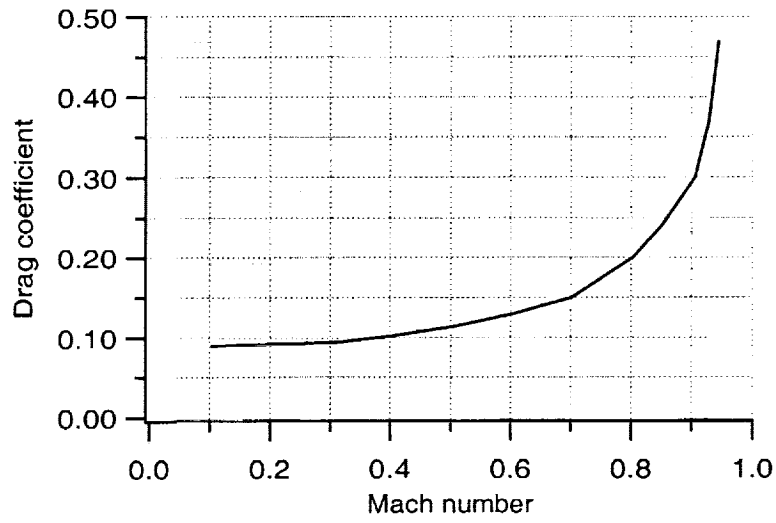
Figure 7 C_D vs. Mach number for an aerodynamically-shaped cylinder with $\delta = 0.25$ (see text)

**Figure 8** Mach number and capsule drop distance vs. time

After taking into account the functional dependence $C_D = f(Mach)$ and integrating eqn. (3) twice for different values of the ballistic coefficient, we obtain the numerical results shown in Fig. 9, for a fineness ratio $\delta \approx 0.25$, a drop altitude of 40 km and a (low-speed) ballistic coefficient β_0 ranging from 2000 kg/m² to 10000 kg/m².

11

The numerical results clearly indicate that it is possible to attain a free fall time between 25 s and 30 s with very reasonable lengths of the chamber and capsule. Appropriate values of the (low-speed) ballistic coefficient in the range of greater interest of 6000-10000 kg/m^2 can be readily obtained with capsule masses ≤ 1500 kg and external diameters smaller than 1.8 m. Designs options will be investigated later on in this report.
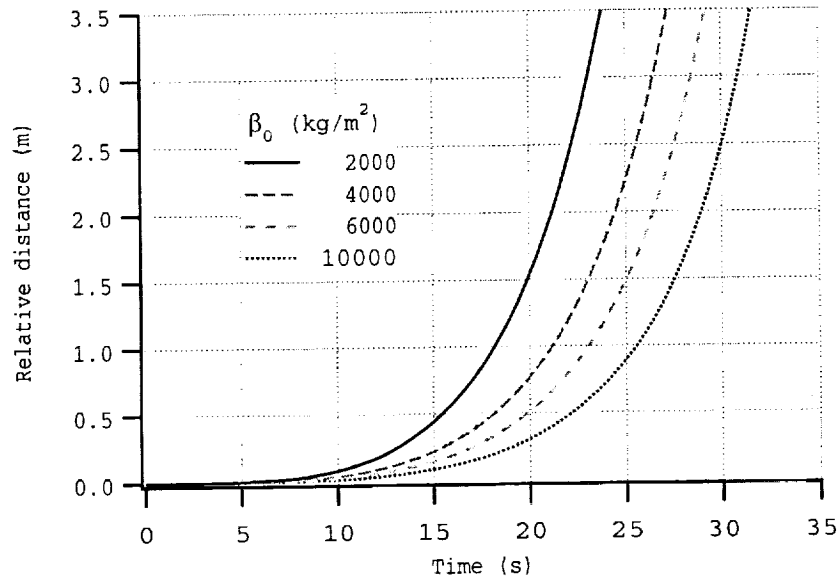
Figure 9 Relative distance for various initial ballistic coefficients
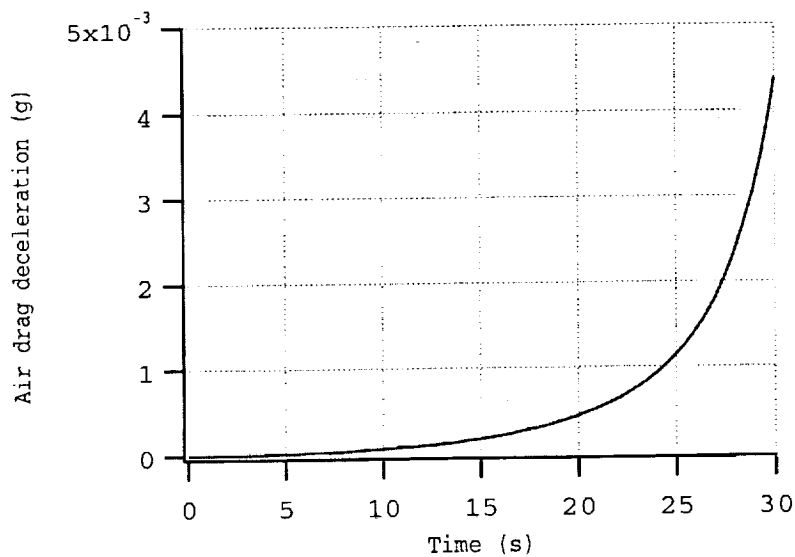
Figure 10 Capsule deceleration due to air drag ($\beta_0 = 6000$)

12
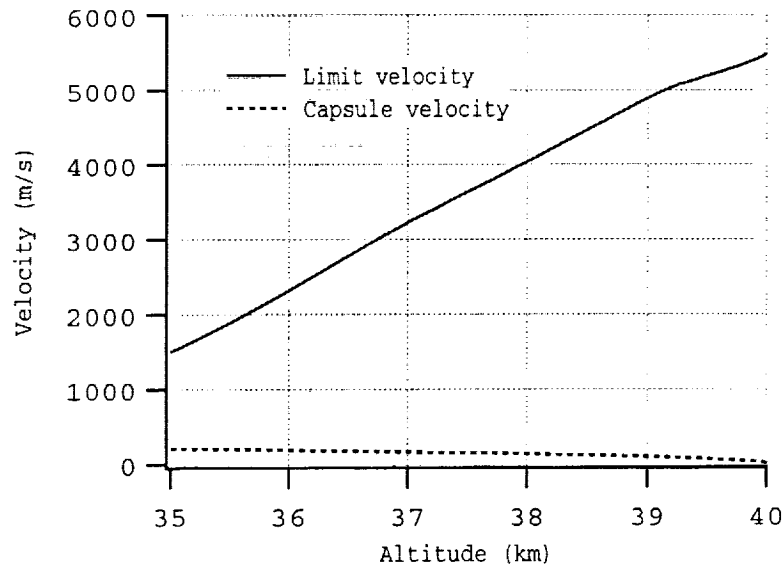
Figure 11 Limit velocity and actual velocity of capsule vs. altitude ($\beta_0 = 6000$)

For completeness the deceleration of the capsule caused by air drag is shown in Fig. 10 for $\beta_0 = 6000$ kg/m^2. Figure 11 depicts the limit velocity and the capsule actual velocity vs. altitude for the same case. The limit velocity is the velocity at which the gravitational and air drag force are equal and, consequently, for a limit velocity much greater than the actual velocity the air-drag deceleration is very small.

Effect of Wind Shear

The horizontal velocities of the capsule and the instrument package (attached to the capsule) are the same at the start of the fall. The inertial horizontal velocity is determined by the rotational velocity of the Earth at the latitude of capsule release and by the local wind. The former (which is much bigger than the latter) simply makes the falling bodies follow a parabolic trajectory rather than a fall along the local vertical. The maximum lateral displacement is of order a couple of hundred meters over a fall distance of 4.4 km which is consistent with a 30-s fall time. It is also worth pointing out that this lateral displacement does not generate any acceleration on board because the displacement is due to an initial non-null velocity and not to external acceleration acting on the falling body.

The diameter of the capsule is important for tolerating vertical gradients (wind shear) of the lateral wind without the need for a propulsion system to compensate for their effect. The balloon will move at the speed of the local wind once the floating altitude has been reached, i.e., the capsule will be at zero relative speed with respect to the local wind. If the wind vertical profile were constant, the capsule and the instrument package would move laterally during the fall with the same initial lateral velocity and hence maintain the same lateral distance with respect to one another. But, if the wind vertical profile changes, the capsule will experience a lateral force that will change its lateral speed while the instrument package will not experience such force.

13

The lateral displacement y of the capsule due to the wind shear $V_z = \partial V/\partial z$ over the vertical drop distance $(Z = 1/2gt^2)$ is as follows:

$$y = \frac{1}{30}\frac{\hat{\rho}}{\beta_l}\frac{Z^3}{g}V_z^2 \tag{8}$$

where ρ is the atmospheric density, $\beta_l = m/(C_{Dl}S_l)$ is the lateral ballistic coefficient of the capsule, S_l the lateral area of the capsule, and g the Earth's surface gravity. Equation (8) is simplified because the atmospheric density has been assumed constant over the drop. The equation, however, provides a good estimate of the lateral displacement of the capsule due to wind shear after adopting the average value of the density along the drop. After calling S the frontal area of the capsule and assuming that $C_{Dl} \approx 10C_D$, $S_l \approx 3S/(\pi\delta)$, which are valid in approximation for a cylinder with aerodynamic nose and tail, we can relate the lateral ballistic coefficient to the frontal (low-speed) ballistic coefficient as follows:

$$\beta_l = \frac{\pi\delta}{30}\beta_0 \tag{9}$$

Consequently, eqn. (8) yields:

$$y = \frac{1}{\pi\delta}\frac{\hat{\rho}}{\beta_0}\frac{Z^3}{g}V_z^2 \tag{10}$$
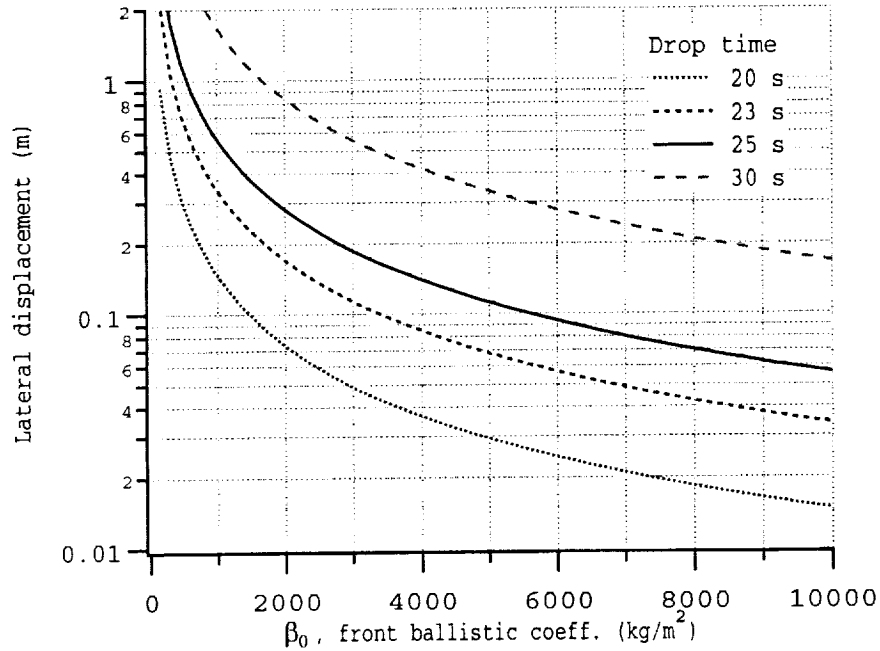
Figure 12 Lateral displacement due to wind shear vs. β_0

For $\hat{\rho} = 6 \times 10^{-3}$ kg/m^3 (i.e., average atmospheric density between 40 km and 35 km of altitude), $V_z = 0.005$ s^{-1}, and $\delta = 0.25$, we obtain the results shown in Fig. 12. A check of the accuracy of eqns. (8) and (10) was also made by means of numerical integration of the equation of lateral motion after assuming an exponential air density profile. The displacement error is less than 5% by using the average density value. The value adopted for the wind shear of 0.005 s^{-1} is equivalent to a vertical gradient of 10 knots per km. This value is twice as high as the maximum wind shear reported[rv] for the Air Force balloon base at Holloman, New Mexico.

The lateral displacements due to wind shear are relatively small for rather conservative values of wind shear, free-fall times and ballistic coefficients greater than 6000 kg/m^2, which are easy to obtain. These results show that there is no need for a thruster system to compensate for the effect of the lateral wind acting on the capsule. The geometry and mass of the capsule can be chosen in a way to accommodate the presence of wind shear. Furthermore, if the balloon is launched during the periodically-occurring wind reversal times (in April-May and September-October) the vertical wind gradient is much smaller than the value adopted for the computations shown here.

The capsule displacement due to wind shear has to be taken into account when computing the internal diameter of the capsule (where the instrument package falls). However, it will be shown later on that other factors (e.g., gravity gradients) are more important in determining the capsule internal diameter.

SCIENCE CONCEPT ANALYSIS

The error analysis has been extended with respect to what is reported in Ref.[xvi] to include a thorough analysis of the gravity gradient generated by the distributed mass of the capsule, the concentrated masses on board the capsule, and the Earth's mass for generic positions and orientations of the sensor. The acceleration noise inside the capsule has also been revisited after considering that in the new reference design (see later on) the chamber is fully cryogenic. The intrinsic noise components of the detector (Brownian and preamplifier noise) were also recomputed based on new information from the IFSI laboratory. As a results of these new analyses, requirements have been derived for: (a) the mass distribution of the capsule; (b) the tolerable mass and location of equipment on board the capsule; (c) the orientation of the sensor during free fall and the centering of the two sensing masses; and (d) the characteristics parameters of the detector that affects its intrinsic noise level.

Acceleration Noise inside Capsule

The experimental package moves at very low speed inside the capsule. Consequently, the residual gas inside the vacuum chamber produces a minute force on the free-falling package with a frequency content centered at $f = 1/t_f$ s^{-1} where t_f is the free-fall time. This gas thus affects the acceleration of the instrument package in a frequency range well removed from the signal frequency. The acceleration, as a function of pressure inside the chamber, is as follows:

$$a_D = \frac{C_D A}{2m} \frac{V^2 p}{RT} \tag{11}$$

where A and m are the frontal area and mass of the instrument package, respectively, V is the maximum velocity of the instrument package with respect to the falling capsule, R is the gas constant, T the temperature of the residual gas, and p the pressure inside the chamber. Because of the new reference design (see later on) with a fully cryogenic vacuum chamber, the residual gas in the chamber is refrigerated Helium. After assuming $C_D = 2.2$ (for a free-molecular regime), $A = 0.1$ m^2, m = 30 kg, V = 0.5 m/s (obtained by integrating eqn. 3 once up to 30 s), R = 2078 J/(kg-K), T $\approx$ 5 K, and p = 10^{-6} mBar, eqn. (11) yields $a_D = 10^{-12}$ g. The spectrum of this acceleration is centered at a frequency 0.033-0.05 Hz for free-fall times t_f in the range 20-30 s. Consequently, the magnitude of the acceleration at the signal frequency f_s, which is in the range 0.2-0.5 Hz, is well smaller than 10^{-12} g. This acceleration is a common-mode acceleration which is further reduced by the common-mode rejection factor (CMRF) of order 10^{-4}.

Furthermore, the vacuum strongly attenuates the propagation of perturbations from the walls of the capsule to the free-falling instrument package. The estimate of the acceleration at the falling instrument package produced by the vibrating walls of the capsule are based on the experimental data measured on board the system Mikroba[xvii]. This system shares the fall from a stratospheric altitude; it is not, however, a free-falling experimental package inside the shielding capsule. In Mikroba, the measurement

16

package or experiment is solidly attached to the walls of the falling capsule. Moreover, Mikroba is not propelled during the first 30 s (like our experiment) although it is propelled downwards during the next 30 s. Once the magnitude of the acceleration at the walls $|a_{wall}|$ is known, the magnitude of the acceleration at the falling package $|a|$ can be readily computed as explained in the following. The motion of the vibrating walls increase the kinetic energy of the gas molecules above the thermal velocity. The kinetic energy variation is then expressed as a pressure variation Δp of the gas after equating the increase in kinetic energy to the work done on the gas molecules by the vibrating walls. We then assume, conservatively, that the pressure perturbation Δp acts on one side only of the instrument package in order to compute an upper bound of the acceleration disturbance imparted to the package. The upper bound of the acceleration at the instrument package is as follows:

$$|a| = \frac{\Delta p}{mv}|u_{wall}| = \frac{\Delta p}{m\omega v}|a_{wall}|$$

(12)
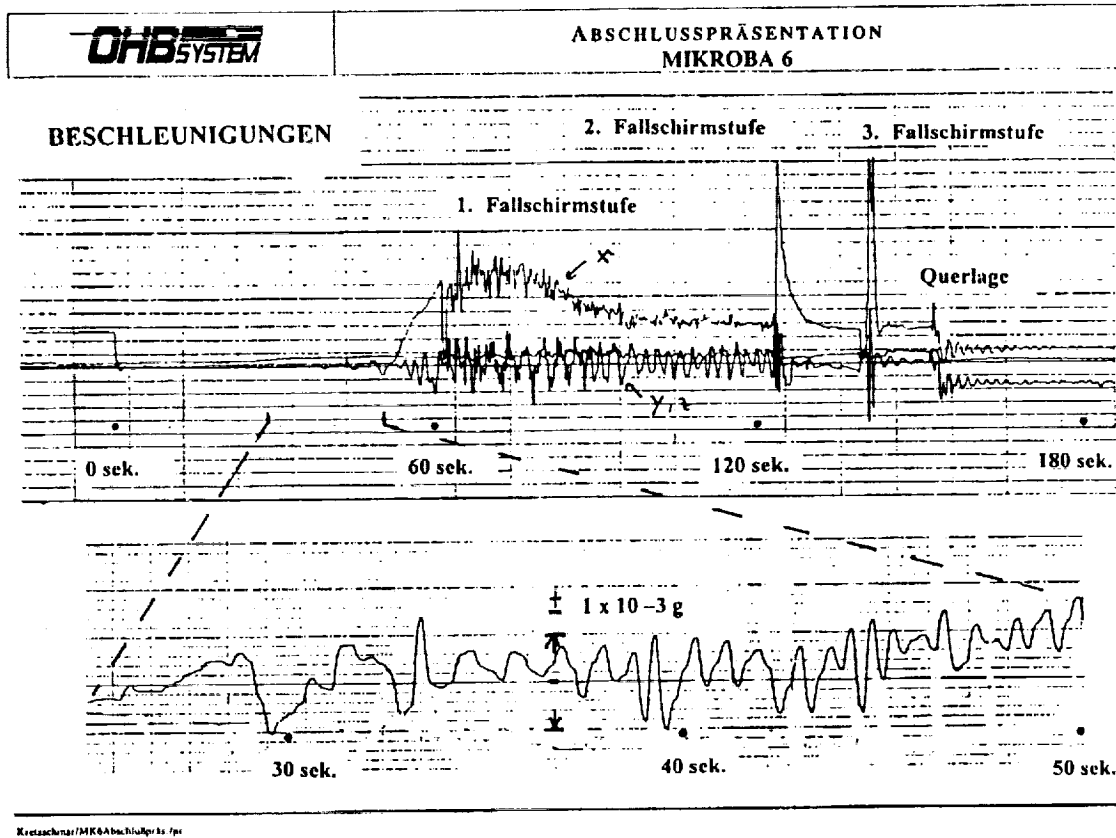
Figure 13 Acceleration measured on board the Mikroba capsule (with accelerometer solidly attached) during the fall [Kretzchmar, 1999]

In equation (12), A and m are the cross section and mass of the instrument package, v is the thermal velocity of the residual gas, a and a_{wall} are the accelerations of the package and the wall, respectively, p is the pressure inside the capsule, $u_{wall} = a_{wall}/\omega$ is the velocity

17

and ω the angular frequency of the vibrating walls. If, for example, p = 10^{-6} mBar and the temperature of the gas inside the capsule is slightly higher than LHe, we obtain an attenuation factor a/a_{wall} = 6×10^{-10} at the signal frequency of our experiment (~0.5 Hz). In other words, the high vacuum provides an excellent attenuation of the wall vibrations. The capsule walls do not necessarily vibrate at the signal frequency of the instrument. The cryostat will be designed with structural frequencies much higher than the experiment signal frequency. However, in this early stage of the design and for conservativeness, we assume that the wall acceleration has a component at the signal frequency with an intensity equal to the largest magnitude of the acceleration recorded on Mikroba during the first 30-s of fall, that is, a_{wall} < 10^{-4} g (although not very visible in Fig. 13). We then obtain an acceleration at the instrument package of order 10^{-13} g under rather conservative assumptions. Consequently, the free-falling capsule reduces the acceleration noise to values unmatched by any other Earth-based drop facility and comparable to values achieved on board the Triad drag-free satellite[xviii].

The acceleration components above are common-mode-type (i.e., they affect equally both sensing masses) thus they can be further reduced by the common-mode rejection fact of the differential accelerometer. With a typical value of 10^{-4} for the CMRF, the influence of these accelerations on the differential measurement is made negligible.

The acceleration noise components produced by the residual gas in the capsule are proportional to the pressure inside the capsule. The pressure can be reduced in successive flights if, for any unanticipated reasons, its influence on the measurement proves to be greater than expected. It is, in fact, well within the state of the art to obtain pressures at room temperature as low as 10^{-8} mBar in large volumes.

Internal noise of detector

The most important internal noise sources for a high accuracy mechanical detector like the one proposed for this WEP test are: (1) preamplifier noise; and (2) thermal noise (Braginsky, 1974[xix]; Giffard, 1976[xx]). The combined effect of these two noise components upon the acceleration spectral density S_a of the detector's output is given by the following equation for an instrument with the measurement frequency smaller than the resonant frequency ω_0, a measurement bridge pumped at the frequency ω_P (of typically tens of kHz) and a preamplifier that matches the transducer impedance[xxi]:

$$S_a = \frac{1}{g} \left[\frac{4 k_B \omega_0}{m_{eff}} \left(\frac{T}{Q} + T_n \frac{2\omega_0}{\beta \omega_P} \right) \right]^{1/2} \quad g/\sqrt{Hz} \tag{13}$$

In equation (13), the two terms in round parentheses correspond to the Brownian noise and the preamplifier noise, respectively; ω_0 is the detector resonant frequency; k_B the Boltzmann's constant; T the ambient temperature; T_n the preamplifier noise temperature; Q the quality factor; m_{eff} the effective mass of the sensing mass; and β the electromechanical transducer factor. The effective mass is used to convert a rotation of the sensing mass into a translation of equal energy. Its relationship to the mass m is: m_{eff}

$= m(\eta_t/l)^2$ where η_t and l are, respectively, the radius of inertia and the lever arm with respect to the rotation axis of the sensing mass. With the geometry of the sensing masses in our detector $m_{eff} \approx 1.8m$.

Clearly, from eqn (13), we see that the sensitivity of the detector increases by decreasing the resonant frequency and the temperature, and by increasing the mass of the sensing masses and the Q-factor. Liquid He (4.2 K) refrigeration will be used to provide low Brownian noise and a high Q-factor. These are necessary conditions to achieve the desired measurement accuracy. In order to derive requirements for the detector, we assume that the contribution of the Brownian noise is about equal to the contribution of the preamplifier noise. In this case, if we set our experiment accuracy goal to a few parts in 10^{-15} (with 95% confidence level and a 20-s integration time) each one of the two noise components should be smaller than 6×10^{-15} $g/\sqrt{Hz}$. These noise requirements imply the following (see also the section on Requirements Development):

$$T < 10 \text{ K}; T_n < 60 \text{ mK}; m > 5 \text{ kg}; \omega_0/Q < 2\pi/ 10^5 \text{ rad/s} \qquad (14)$$

These requirements do not exceed the state-of the-art but they do require a very careful construction of the detector with low dissipation and the use of very-low-noise preamplifier. Key quantities like the Q-factor at low temperature and the preamplifier noise will be measured experimentally by our partners at IFSI once a prototype laboratory detector is built. Noise contributions other than the intrinsic noise components of the detector should be kept at a lower level in order to make them smaller than the intrinsic noise.

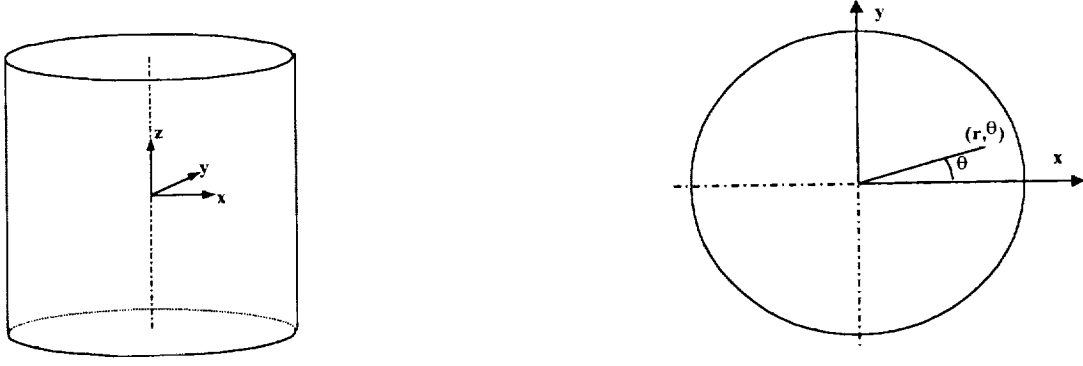## Gravity Gradients

Capsule Gravity Gradients

The gravity gradients generated by the distributed mass of the chamber/cryostat and their effects on the differential measurement are analyzed in the following for a generic position of the detector inside the capsule and a generic orientation of its spin axis with respect to the gradient field.

Gravity gradient for a mass distribution with cylindrical symmetry

For a mass distributed with cylindrical symmetry, the resultant gravitational acceleration has two components:

a_z = acceleration component along the cylinder axis
a_r = acceleration component along the cylinder radius

Figure 14 Reference frames for gravity gradient analysis

After erecting a Cartesian reference system xyz as depicted in Figure 14, the components of the gravity gradient tensor are computed according to the following transformation formulas:

$$
\begin{aligned}
dx &= \cos(\theta) \cdot dr - r \cdot \sin(\theta) \cdot d\theta \\
dy &= \sin(\theta) \cdot dr + r \cdot \cos(\theta) \cdot d\theta \\
da_x &= \cos(\theta) \cdot da_r - a_r \cdot \sin(\theta) \cdot d\theta \\
da_y &= \sin(\theta) \cdot da_r + a_r \cdot \cos(\theta) \cdot d\theta
\end{aligned}
\tag{15}
$$

Setting $\theta = 0$ and indicating the spatial derivative with a second subscript:

$$a_x = a_r$$

$$a_y = 0$$

and

$$
\begin{aligned}
a_{xx} &= a_{rr} \\
a_{xy} &= 0 \\
a_{yy} &= a_r / r \\
a_{xz} &= a_{zx} = a_{rz} \\
a_{yz} &= a_{zy} = 0
\end{aligned}
\tag{16}
$$

Hence the gravity gradient tensor has the form:

$$
\Gamma =
\begin{bmatrix}
a_{rr} & 0 & a_{rz} \\
0 & a_r / r & 0 \\
a_{rz} & 0 & a_{zz}
\end{bmatrix}
\tag{17}
$$

20

As a result of the Laplace equation, the trace of the gravity gradient tensor is equal to zero, that is

$$a_{rr} + a_r / r = -a_{zz} \tag{18}$$

In the singular case of r = 0 the limit calculation yields:

$$\Gamma_{(r=0)} = \begin{bmatrix} a_{rr} & 0 & 0 \\ 0 & a_{rr} & 0 \\ 0 & 0 & -2a_{rr} \end{bmatrix} \tag{19}$$

Gravity gradient matrix of a rotating body

In general a gravity gradient matrix has the form:

$$\Gamma = \begin{bmatrix} \Gamma_{xx} & \Gamma_{xy} & \Gamma_{xz} \\ \Gamma_{yx} & \Gamma_{yy} & \Gamma_{yz} \\ \Gamma_{zx} & \Gamma_{yz} & \Gamma_{zz} \end{bmatrix} \tag{20}$$

The rotated matrix Γ' after a $\theta = \omega t$ rotation is:

$$\Gamma' = R_\theta \Gamma R_\theta^T \tag{21}$$

where R_θ is the rotation matrix and R_θ^T its transpose.

After a rotation about an axis (i.e., the x' axis), the rotated matrix has four components modulated at ω, four components modulated at 2ω and one component that is not modulated.

The ω-modulated components of the transformed matrix are:

$$\Gamma'_{12} = \Gamma'_{21} = \Gamma_{xz} \sin(\omega \cdot t) + \Gamma_{xy} \cos(\omega \cdot t) \tag{22.1}$$

$$\Gamma'_{13} = \Gamma'_{31} = \Gamma_{xz} \cos(\omega \cdot t) - \Gamma_{xy} \sin(\omega \cdot t) \tag{22.2}$$

where x' = 1, y' = 2, z' = 3. In summary, the *off-diagonal components* $\Gamma''_{12} = \Gamma''_{21}$ and $\Gamma''_{13} = \Gamma''_{31}$ of the gravity gradient matrix produce components that are modulated at the rotation frequency.

21

Gravity gradient matrix projected onto body axes

In a general case the body reference frame placed at the CM of a sensing mass of the detector can be identified with respect to the cryostat frame by means of 3 successive rotations as follows:

1 - Rotation $+\alpha$ around z axis (azimuth rotation)
2 - Rotation $+\beta$ around y' axis (elevation rotation)
3 - Rotation $+\omega t$ around x'' axis (spin rotation)

In the computation of gravity gradients, these rotations can either be rotations of the sensing mass with respect to the cryostat or, equivalently, rotations of the cryostat with respect to the sensing mass. In the former case, and solely for the reason of pointing out a typical geometrical situation, the first and second rotations could, for example, be caused by the detector dynamics during free-fall (e.g., precession of its body axes) while the third rotation is the ωt rotation of the detector about its longitudinal axis aimed at modulating the signal.

Clearly, we are mostly concerned about the components of the gravity gradient matrix that contain a frequency ω equal to the modulation frequency of the signal. We can choose the body axis y' = 2 to coincide with the sensitive axis of the accelerometer and, consequently, we are only concerned with the component Γ''_{21} of eqn. (22.1). In general, the moduli of the two components Γ''_{12} and Γ''_{13} are the same and they can be written as follows:

$$\chi = \sqrt{\Gamma_{xy}^{2} + \Gamma_{xz}^{2}} \tag{23}$$

After rotating the original matrix by two rotations α and β (where α is the azimuth of the spin axis with respect to the radial and β is the elevation with respect to the capsule equatorial plane) the expressions of Γ_{xy} and Γ_{xz} in eqn. (23) are as follows

$$\Gamma_{xy} = k_1 \sin(\beta)\sin(\alpha) - k_2 \cos(\beta)\sin(2\alpha) \tag{24.1}$$

$$\Gamma_{xz} = k_3 \sin(2\beta) + k_1 \cos(\alpha)\cos(2\beta) + k_2 \sin(2\beta)\cos^2(\alpha) \tag{24.2}$$

$$k_1 = a_{xz} \tag{24.3}$$

$$k_2 = \frac{1}{2}(a_{xx} - a_{yy}) \tag{24.4}$$

$$k_3 = \frac{1}{2}(a_{yy} - a_{zz}) \tag{24.5}$$

and where the a_{ij} are the matrix components before the rotations are carried out. In the case of a body with cylindrical symmetry and for cylindrical coordinates, eqn. (16) yields $a_{xx} = a_{rr}$, $a_{yy} = a_r/r$, $a_{zz} = a_{zz}$, $a_{xz} = a_{rz}$ and the other components are null.

Using numerical analysis of eqns. (24) and taking into account that inside a cylinder k_2 is always at least one order of magnitude less than k_1 and k_3, we find that the maximum value for χ occurs for $\alpha = 0$. This result implies that the maximum disturbance of the capsule gravity field on the differential accelerometer is produced when the capsule moves radially with respect to the sensor (see Figure 15) in such a way that the spin axis is oriented along the radius of the cylinder through the sensor and the capsule has been displaced radially with respect to the sensor (e.g., by wind shear).
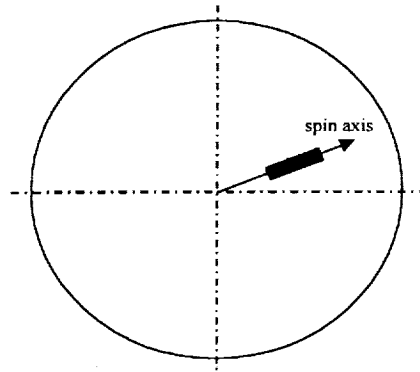
Figure 15 Geometry of sensor and capsule (viewed from the top) for strongest gravity gradient affecting the measurement

On the opposite end, if the motion of the capsule is such as to keep α close to 90°, that is the spin axis is orthogonal to the radial, the disturbance is minimum. In any case since the translational motion of the external capsule is not predictable nor controlled, the worst condition is analyzed setting α equal to zero and varying the angle β. After doing so eqns. (23) and (24) yield:

$$\chi = (k_3 + k_2)\sin(2\beta) + k_1\cos(2\beta) \tag{25}$$

Equation (25) summarizes the disturbances induced by the cryostat mass modulated at the measurement frequency. This equation is important for the cryostat/capsule design. The variations of the quantities k_1, k_2, k_3 inside the cryostat for different shapes and sizes are analyzed numerically in the following subsection.

Variation of k_1, k_2, k_3 in the cryostat/capsule

A numerical code has been developed in Matlab to compute the gravity gradient matrix inside a distributed, massive cylinder. The program, which uses a very large (of order 10^4) number of mass points, can map the desired components of the gravity gradient matrix inside the enclosed surface. The program has been exercised for a

number of cylinders with different H/D ratios (where D is the diameter and H the height) and different caps. Each run takes a couple of hours on a Pentium III PC.

Cylindrical cryostat without caps

We first analyzed the gradient field for various cases of cylinders with various H/D (height over diameter) ratios to conclude that the gradient field is strongly reduced (for the components of interest) for H/D > 1
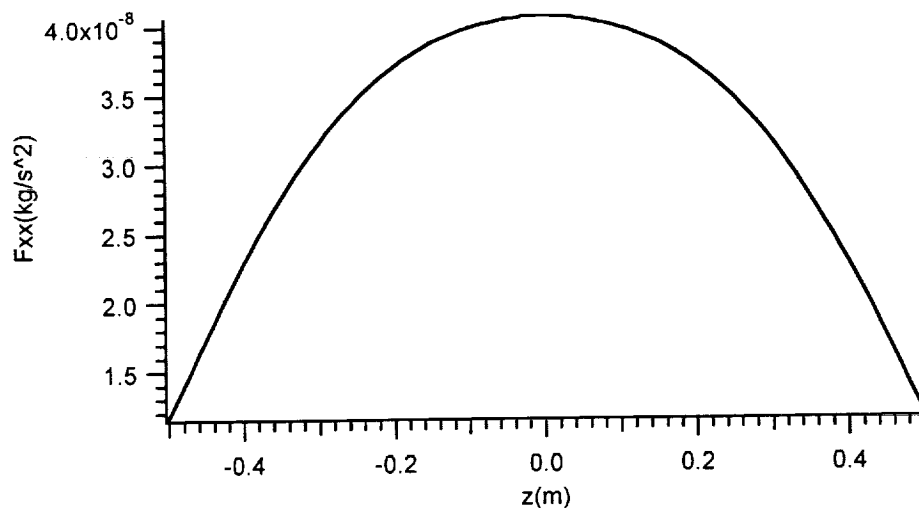
The following results are for a cylinder of uniform mass distribution with the following characteristics:

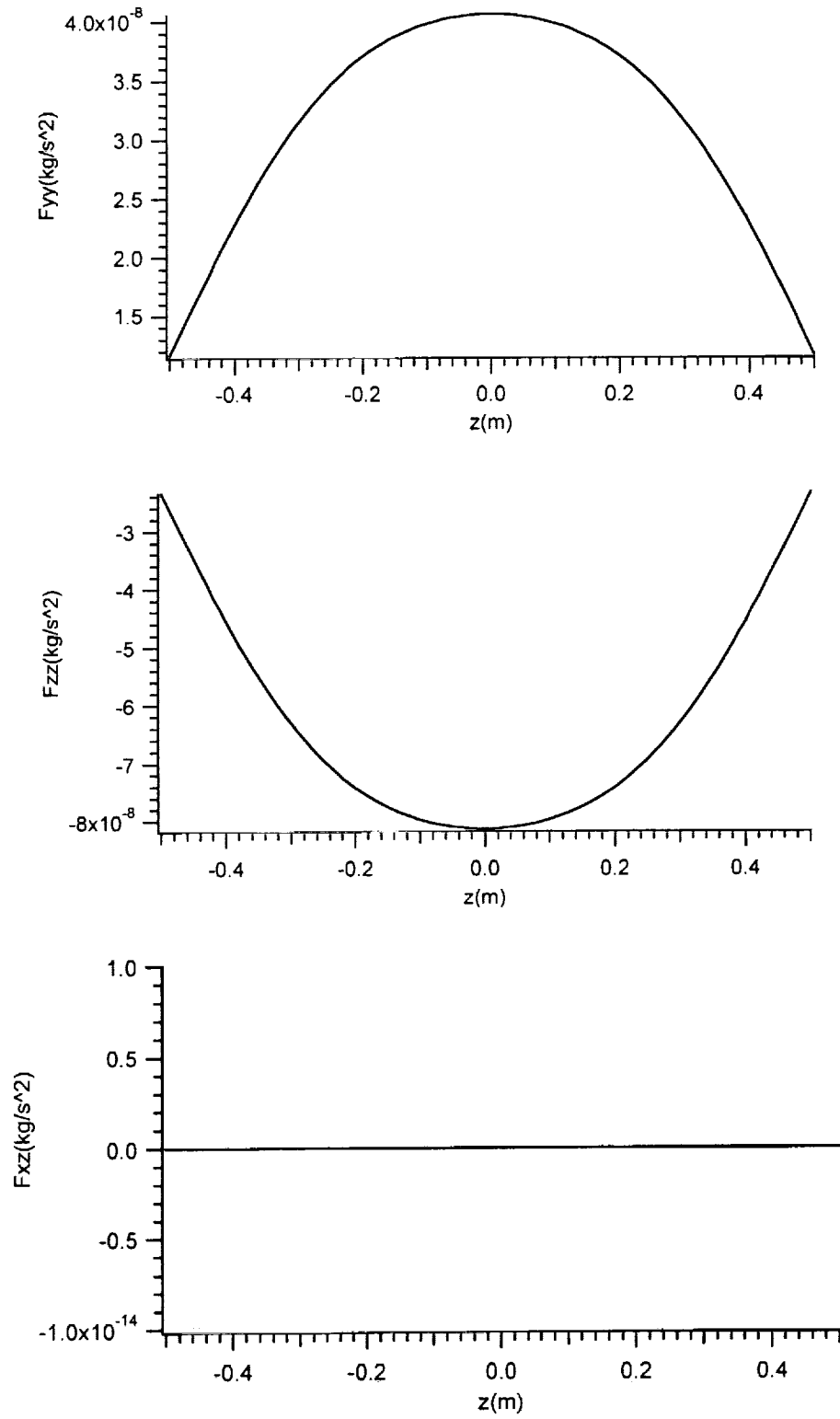Cylinder mass = 500 kg; Dimensions: 1 m (dia) x 1 m (height)
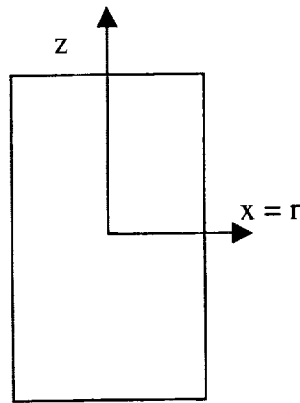
Figure 16 Schematic of cylinder and reference frame
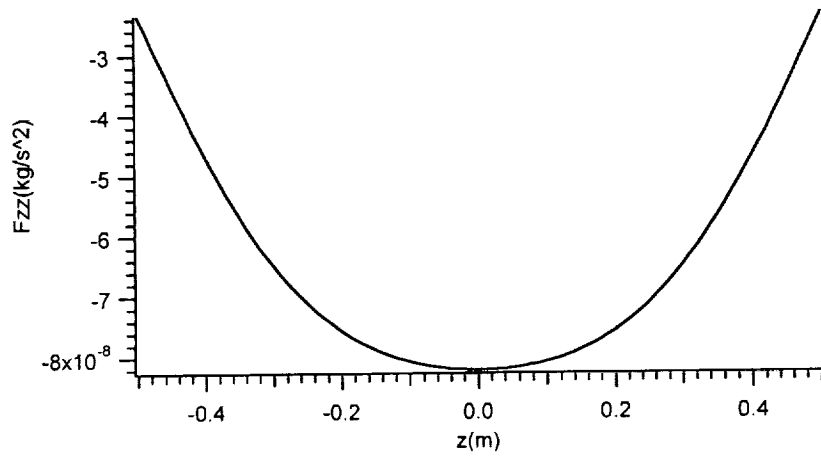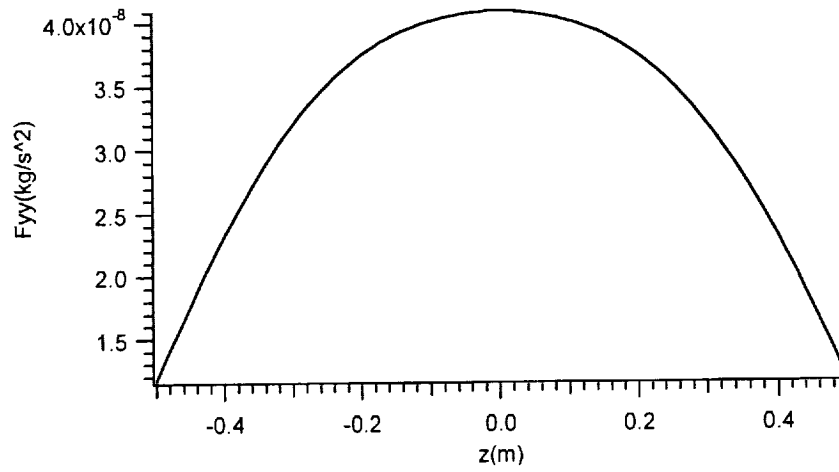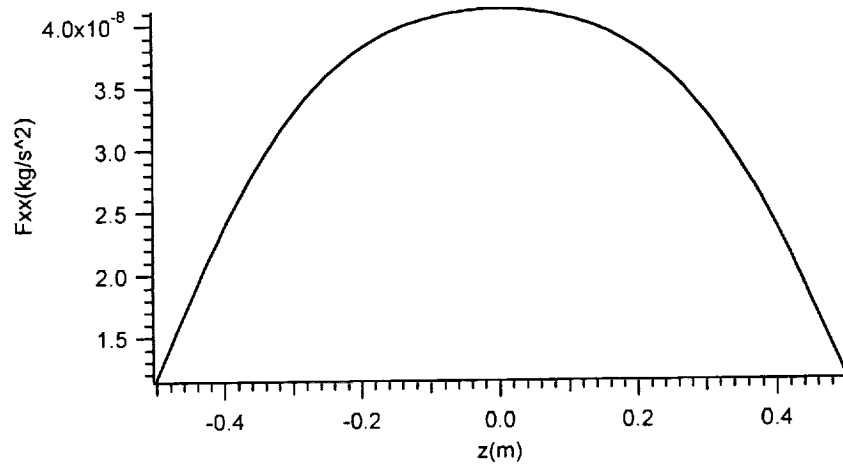
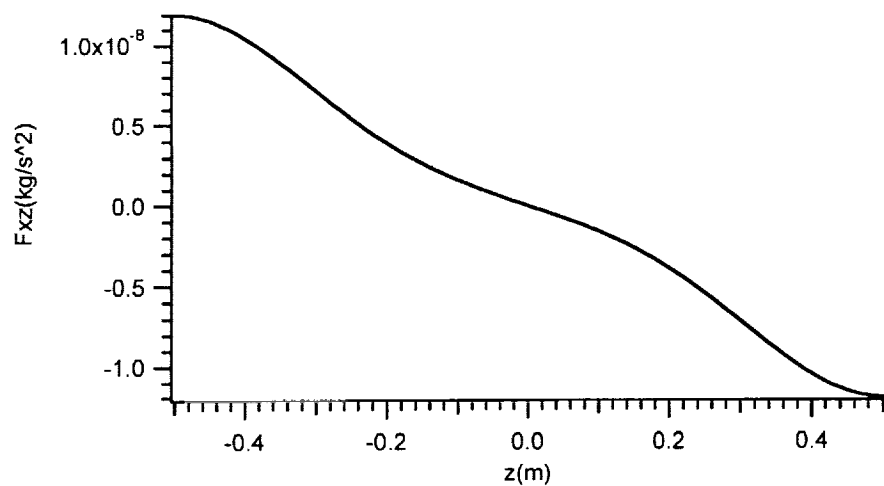Vertical profiles at r = 0 (along centerline)

(continued)

Figure 17 All components of gravity gradient along a vertical profile at r = 0 (units are $f_{rz} = ma_{rz}$ in kg/s² = s⁻² for 1-kg test mass)

Vertical profiles at r = 10 cm

(continued)

Figure 18 All components of gravity gradient along a vertical profile at r = 10 cm (units are $f_{rz} = ma_{rz}$ in $kg/s^2 = s^{-2}$ for 1-kg test mass)

Vertical profiles at r = 20 cm

(continued)

Figure 19 All components of gravity gradient along a vertical profile at r = 20 cm (units are $f_{rz} = ma_{rz}$ in $kg/s^2 = s^{-2}$ for 1-kg test mass)

Vertical profile at r = 30 cm

29
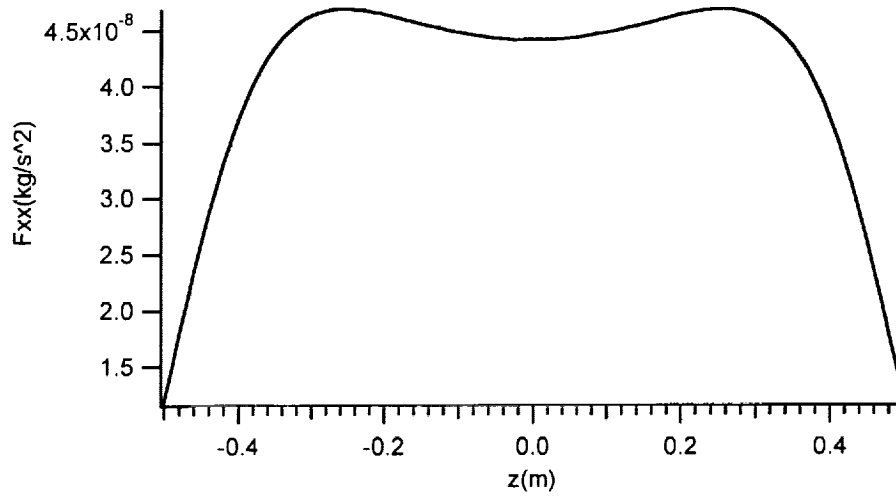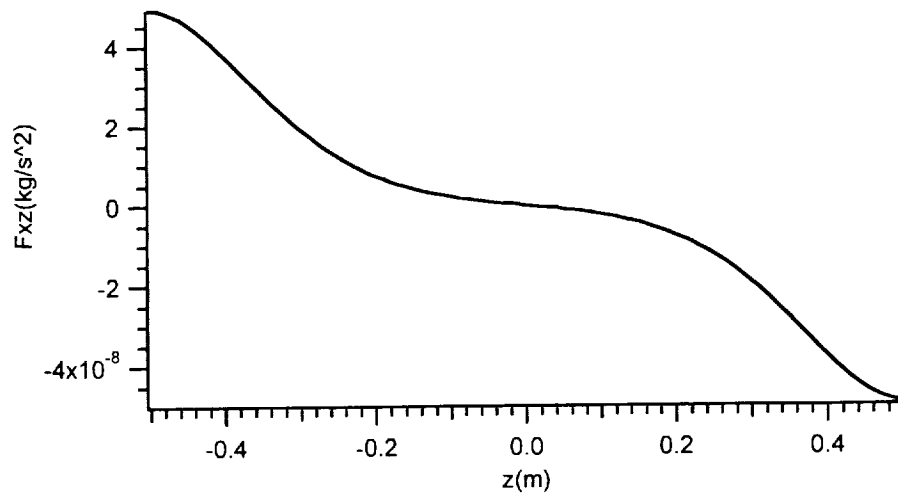
Figure 20 All components of gravity gradient along a vertical profile at r = 30 cm (units are $f_{rz} = ma_{rz}$ in kg/s^2 = s^{-2} for 1-kg test mass)

Vertical profiles at r = 40 cm
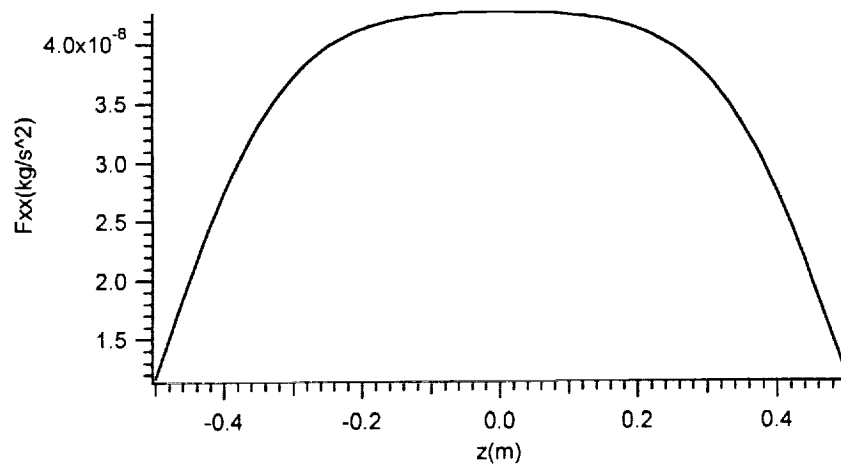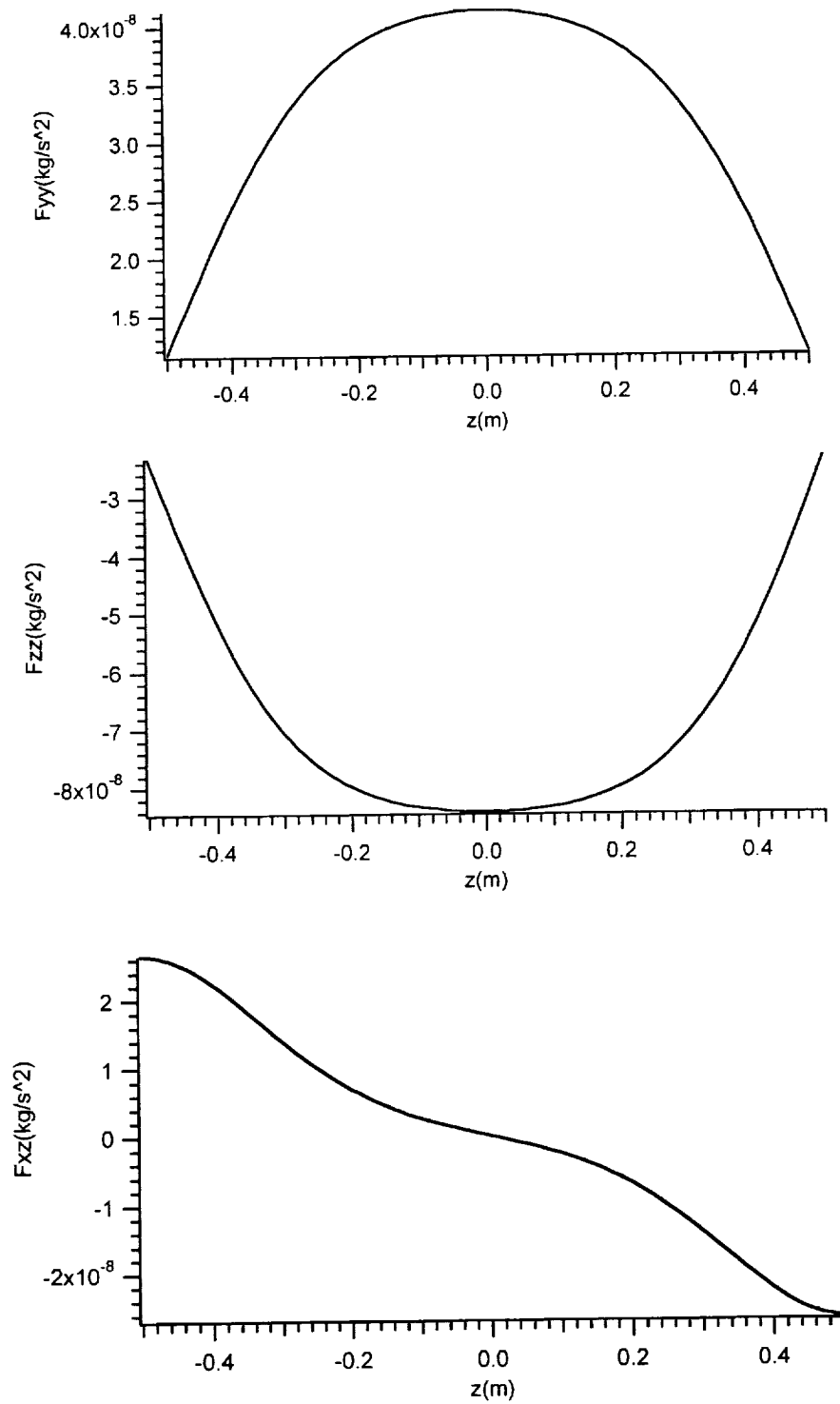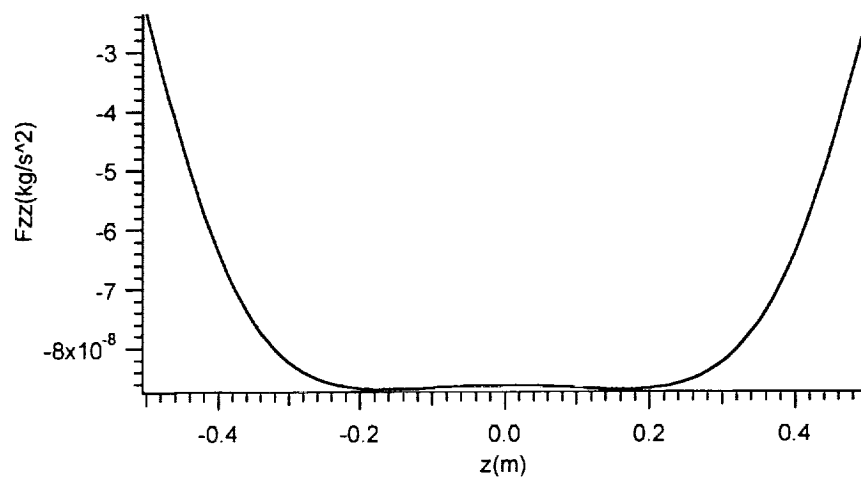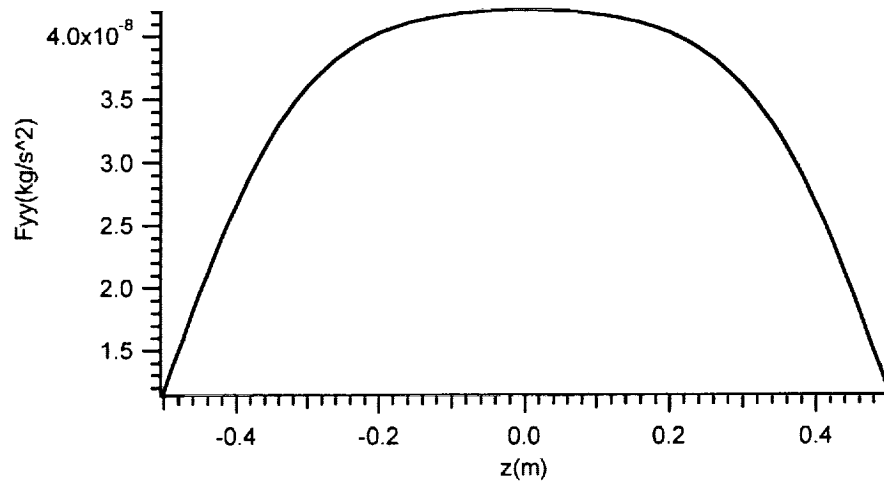

(continued)

30
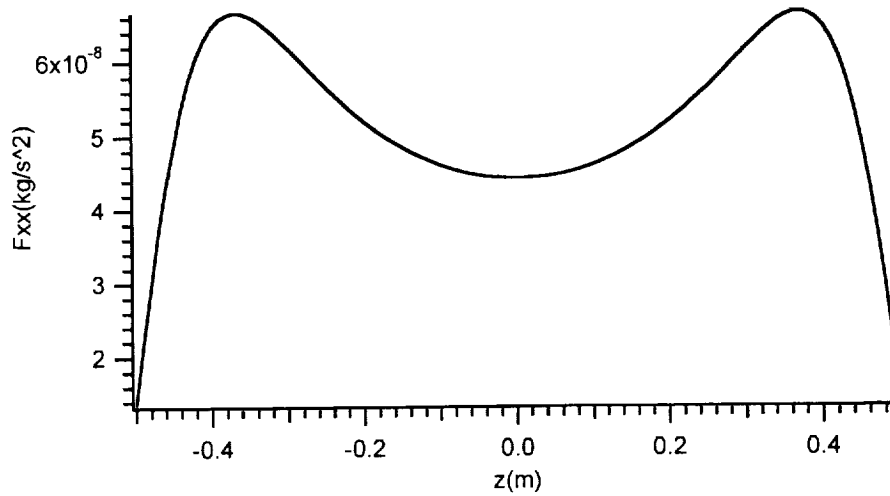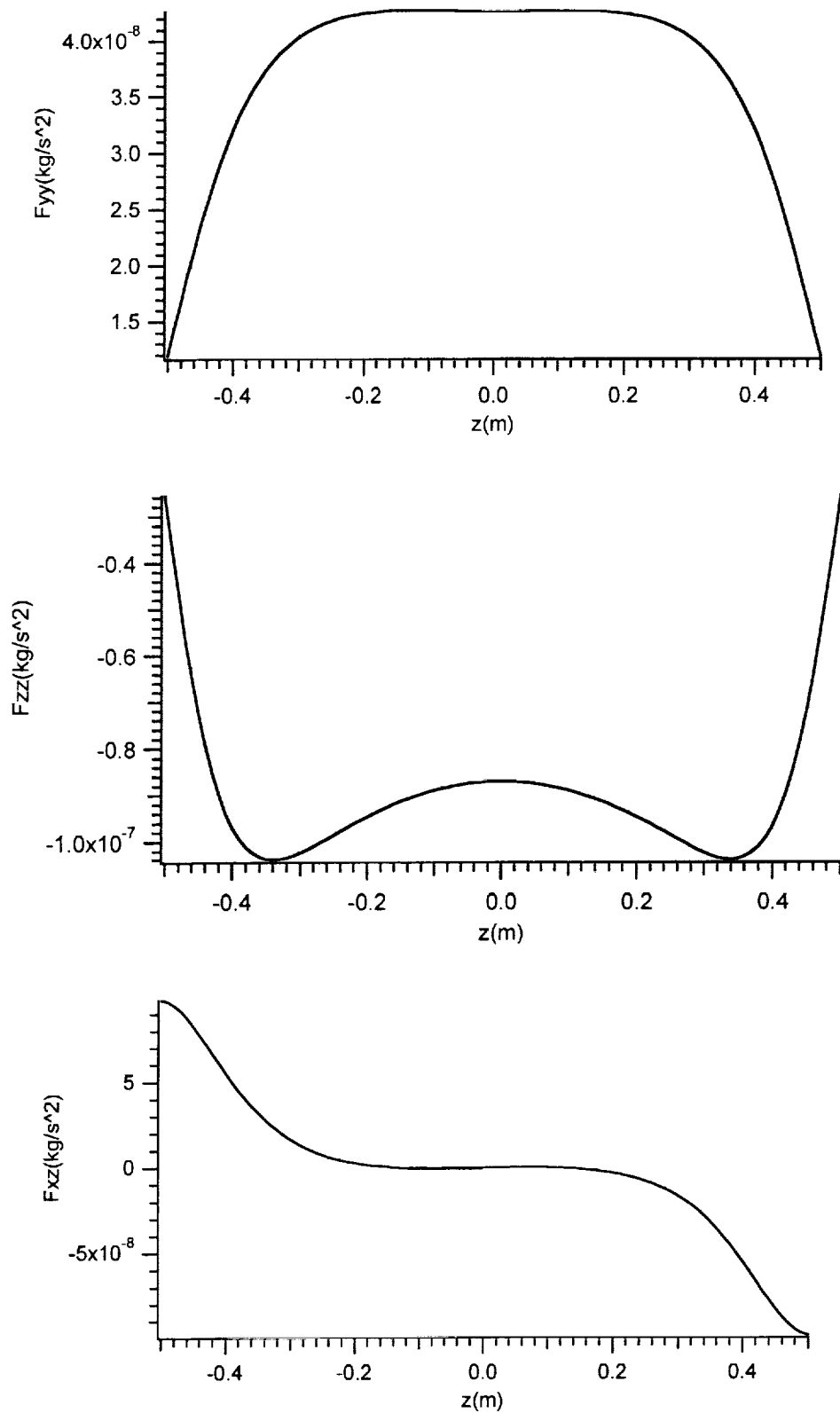
Figure 21 All components of gravity gradient along a vertical profile at r = 40 cm (units are $f_{rz} = ma_{rz}$ in kg/s^2 = s^{-2} for 1-kg test mass)

31

The following is a contour plot of the k_1 component inside the cylinder and the radial profiles of this component along radii at various distances from the cylinder's equatorial plane.

$$k_1 \ (1/s^2)$$
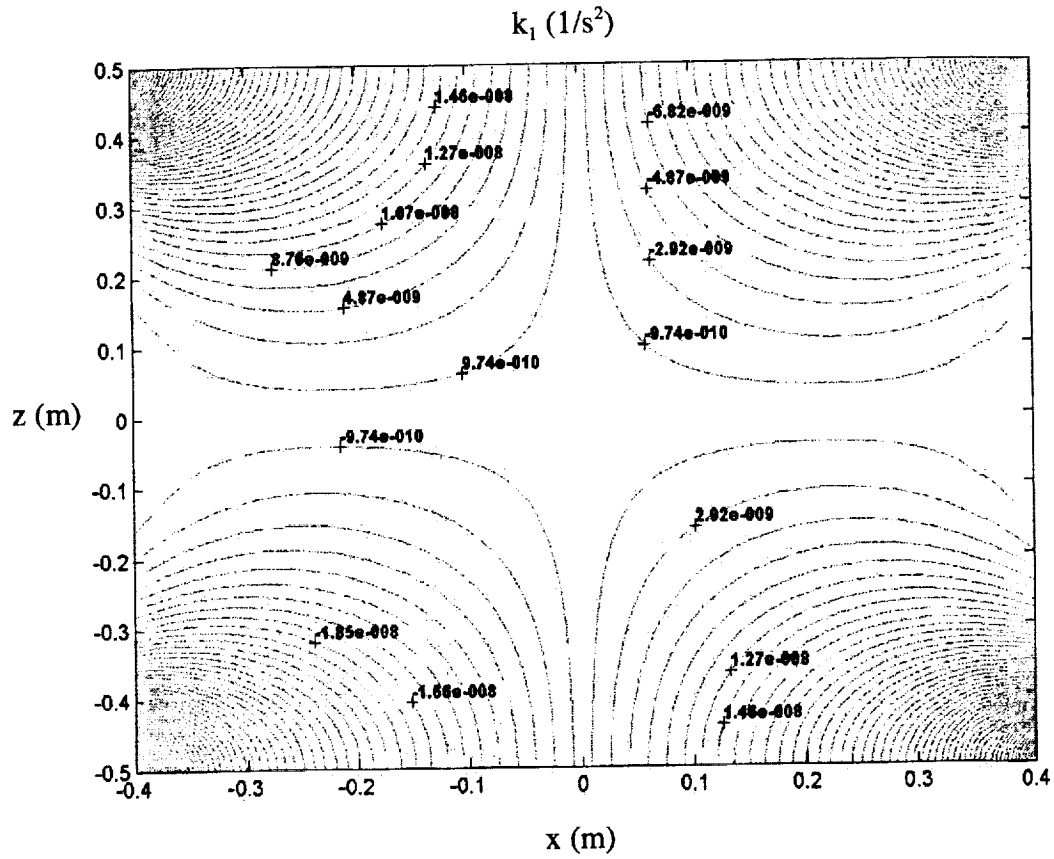
Figure 22 Contour plot of capsule gravity gradient component $k_1 = a_{rz}$ (s^{-2}) for a cylinder with H/D = 1-m/1-m

z = 10 cm (above cylinder's equatorial plane)
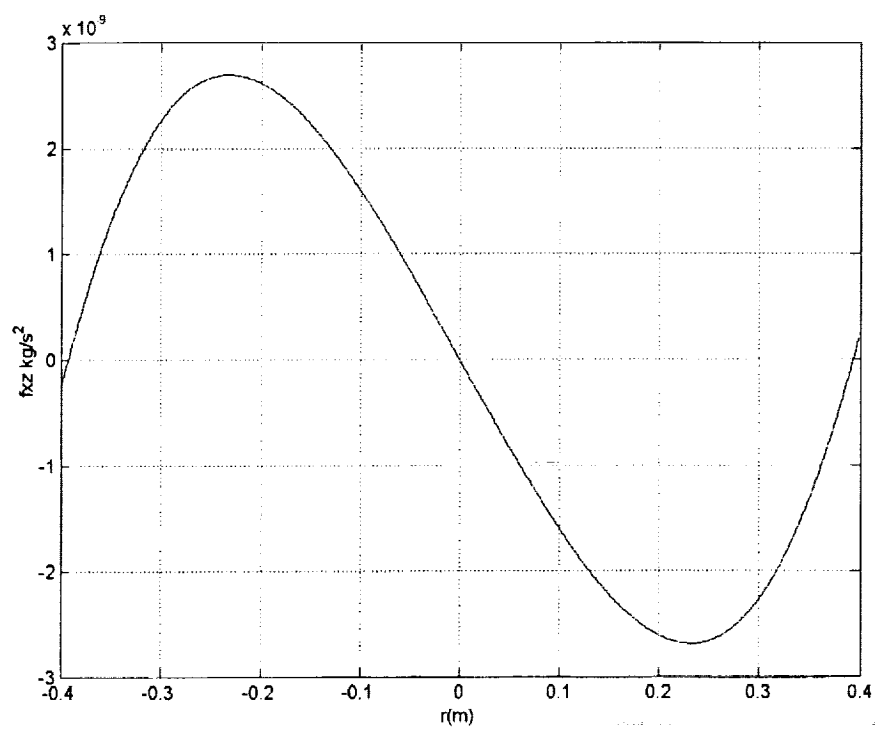
z = 20 cm (above cylinder's equatorial plane)
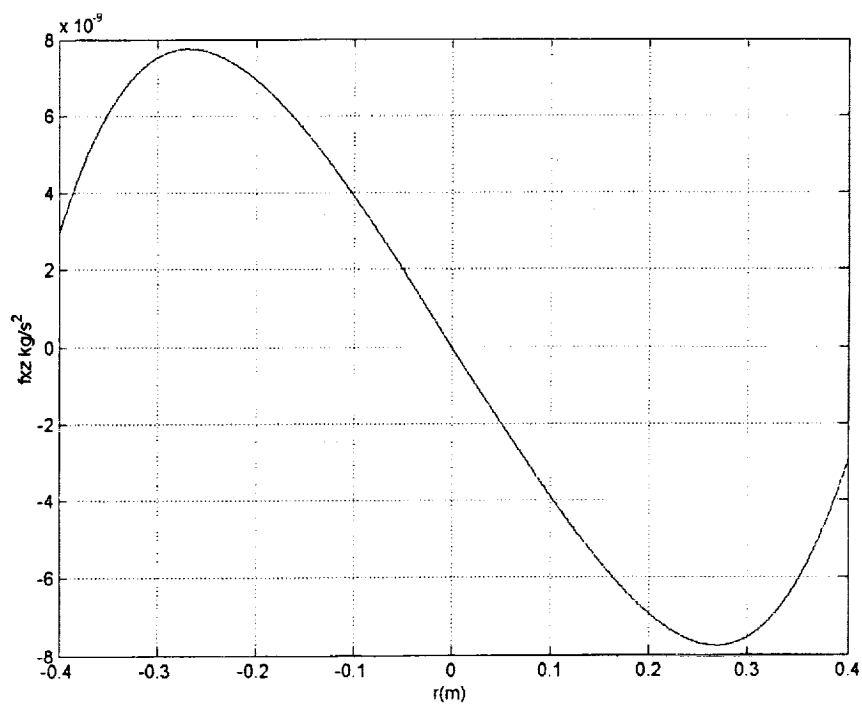
(continued)

z = 30 cm above cylinder's equatorial plane
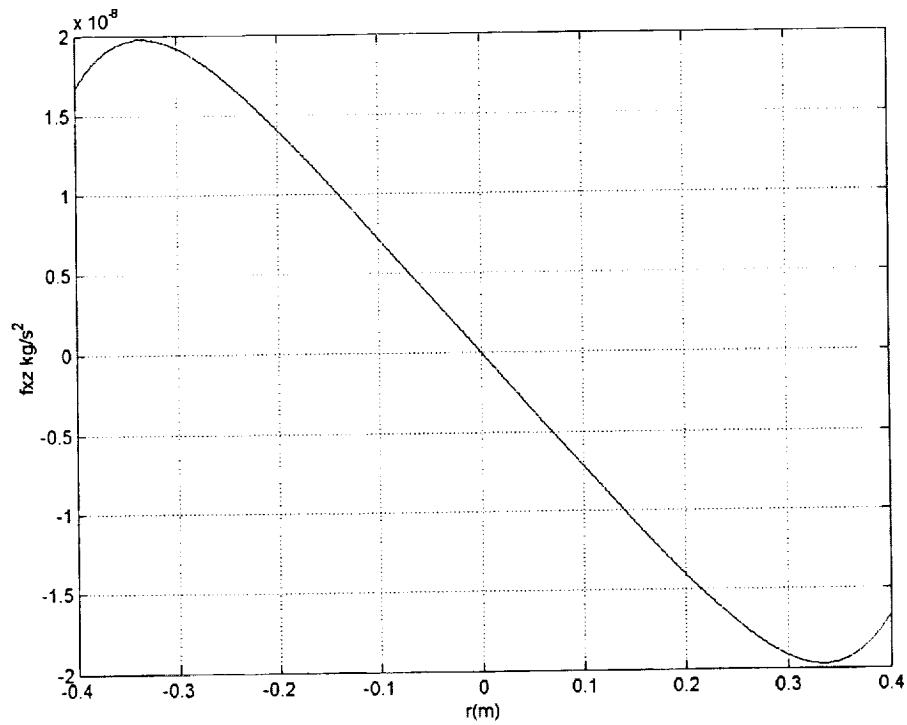
z = 40 cm above cylinder's equatorial plane
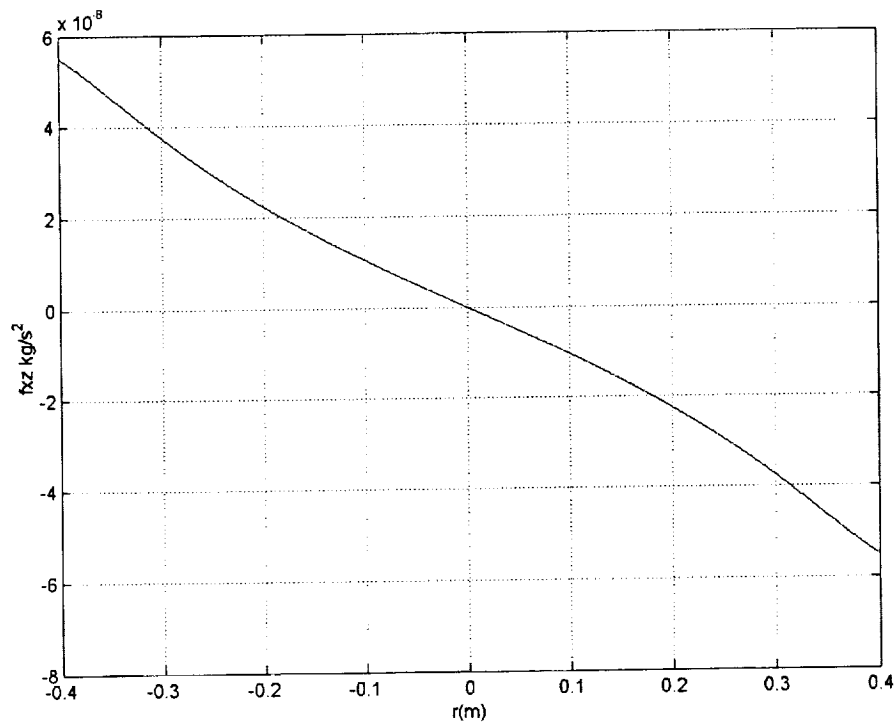
Figure 23 Gravity gradient ($a_{rz} = k_1$ component) for latitudinal sections at different distances above the cylinder's equator (units are $f_{rz} = ma_{rz}$ in kg/s^2 = s^{-2} for 1-kg test mass)
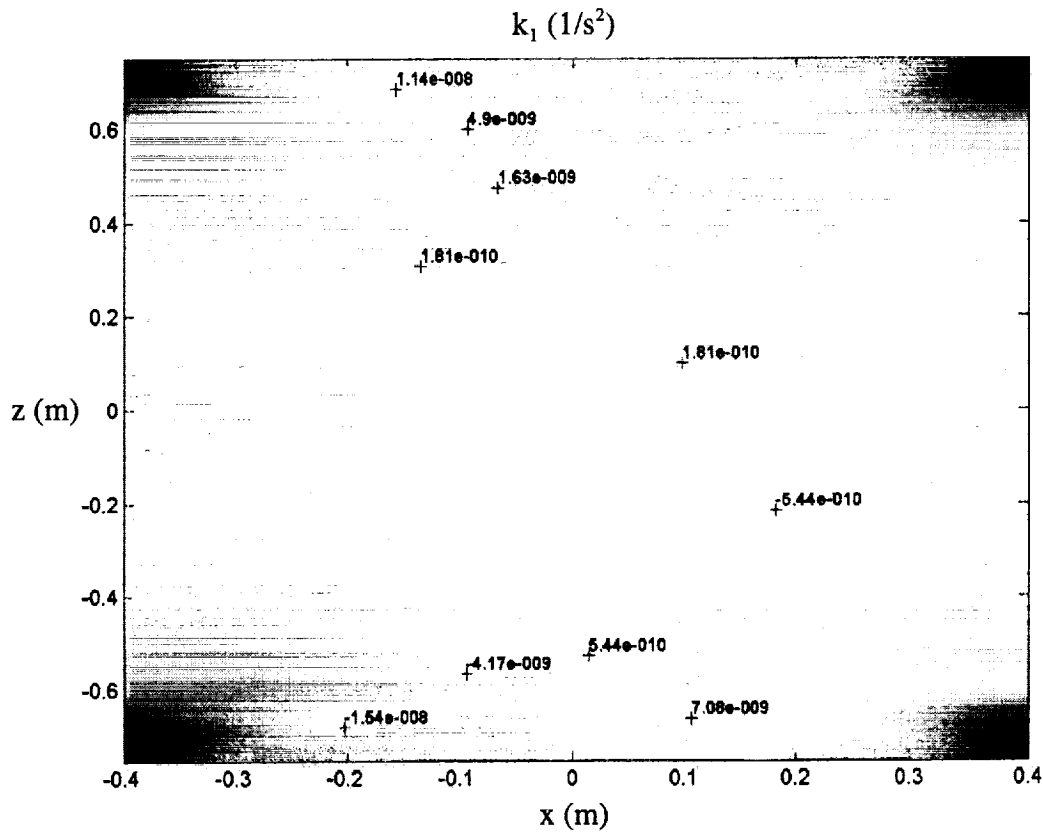
Figure 24 Contour plot of capsule gravity gradient component a_{rz} (s^{-2}) for a cylinder with H/D = 1.5-m/1-m

Figure 24 shows the contour plot of the $k_1 = a_{rz}$ component for a cylinder with H/D = 1.5-m/1-m. Note that the strength of the gravity gradient in the area of interest (near the cylinder's centerline) is strongly decreased thanks to the lengthening of the cylinder in the vertical direction.

As the cylinder is stretched along the vertical, the effect of the cylinder edges (which produce stronger gravity gradients) is smaller the closer the detector is to the cylinder's centerline, where the detector free falls. In the following plots we will show all the gravity gradient terms k_1, k_2 and k_3 (modulated at ω) inside a cylinder with dimensions close to those that we are considering at the present stage of development of the design.

$k1\ (1/s^2)$
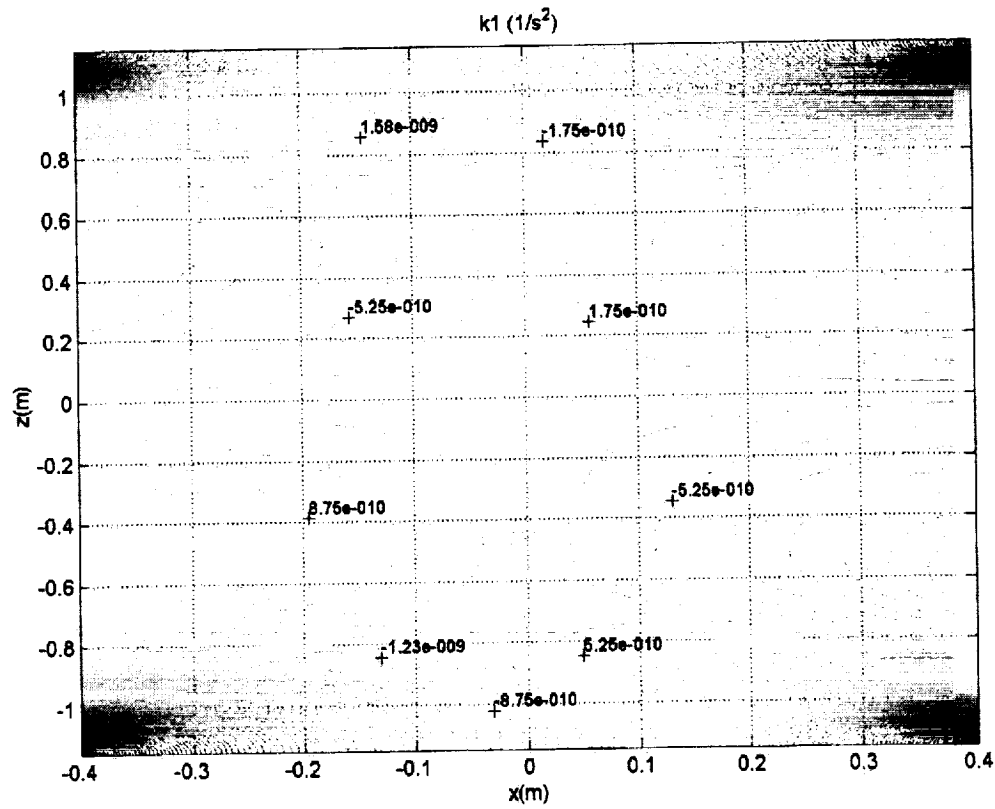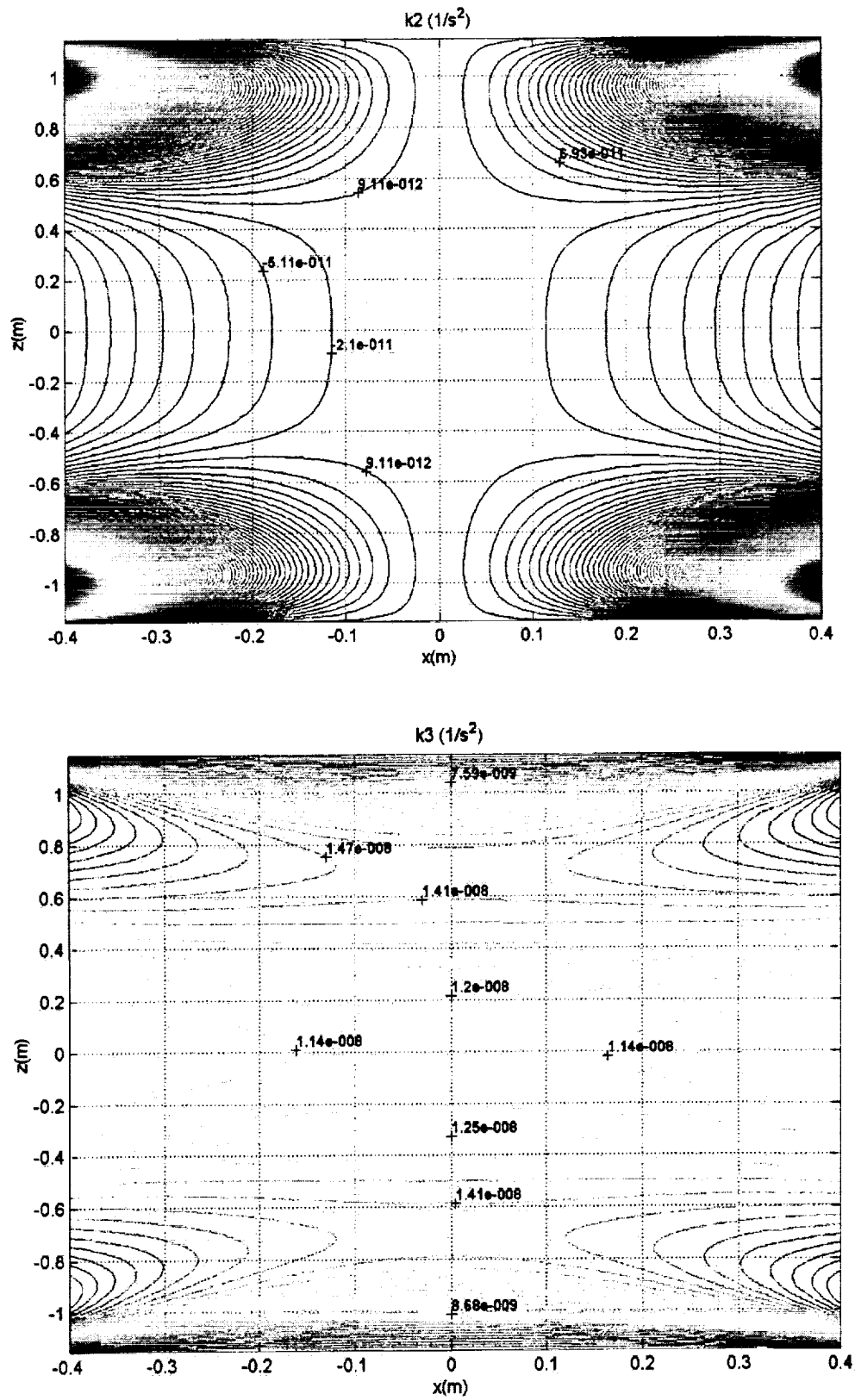
Figure 25 Cylinder without caps and H = 2.3 m; D = 1.2 m; overall mass = 500 kg.

Variation of k_1, k_2, and k_3 along free-fall trajectories

Based on the evaluation of the dynamics of the instrument package relative to the capsule (see also later on), we can map trajectories of the instrument package inside the capsule and evaluate the maximum values of the gravity gradients that the detector will experience during the fall.

It is important to evaluate the strength of the gravity gradient field inside the cryostat along a worst-case trajectory of the instrument package (sensor) that moves with respect to the cryostat/capsule during free fall. Based on worst-case wind shear conditions the trajectory (in z-r coordinates) of the sensor with respect to the cryostat can be expressed as follows:

$$z = z_0 - \frac{a}{\beta_0} t^b \exp(ct^2)$$

$$r = r_0 - \frac{dg^2 t^6}{8\pi\beta_0} + (z - z_0)\sin\gamma$$

(26)

with $a = 0.149636$, $b = 0.001692$, $c = 3.084$, and $d = 6 \times 10^{-7}$ (see section on Optimization). In equation (26), β_0 is the low-speed ballistic coefficient, z_0 and r_0 are the coordinates of the point of release in the cryostat coordinate frame and γ is the angle of the capsule's longitudinal axis with respect to the local vertical which (at this stage of the project) represents a reasonable upper limit for the verticality error of the capsule during the fall..

38

Cylindrical cryostat with flat caps
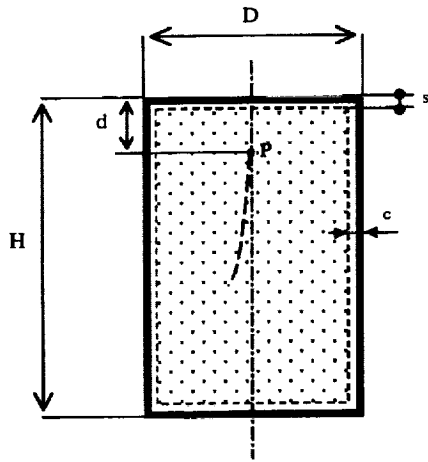
The Matlab routine has been modified to include cryostat caps of different shapes. The routine creates a two-dimensional mesh of point masses uniformly distributed on the average surface of the cylinder and its caps. In the case of flat caps the mass distribution results in a closed cylindrical surface of height H and diameter D. The gravity gradient field has been mapped on the z-x plane where x coincides with the cylinder's radial and z with the longitudinal axis, as far as s = 10 cm from the top and bottom and c = 20 cm from the side walls.

The point of release P lies on the symmetry axis of the cylinder and at d = 40 cm from the top. The sensor trajectory obeys eqns. (26) with β_0 = 10000 kg/m^2 and the capsule verticality error γ = 5° has been conservatively assumed to produce a constant, lateral displacement of the sensor in the same direction of the wind shear. The other parameters in eqns. (26) also represent a worst-case scenario for lateral displacements. The key quantities k_1, k_2 and k_3 are plotted as contour plots on the x-z plane in Figs. 26.

39
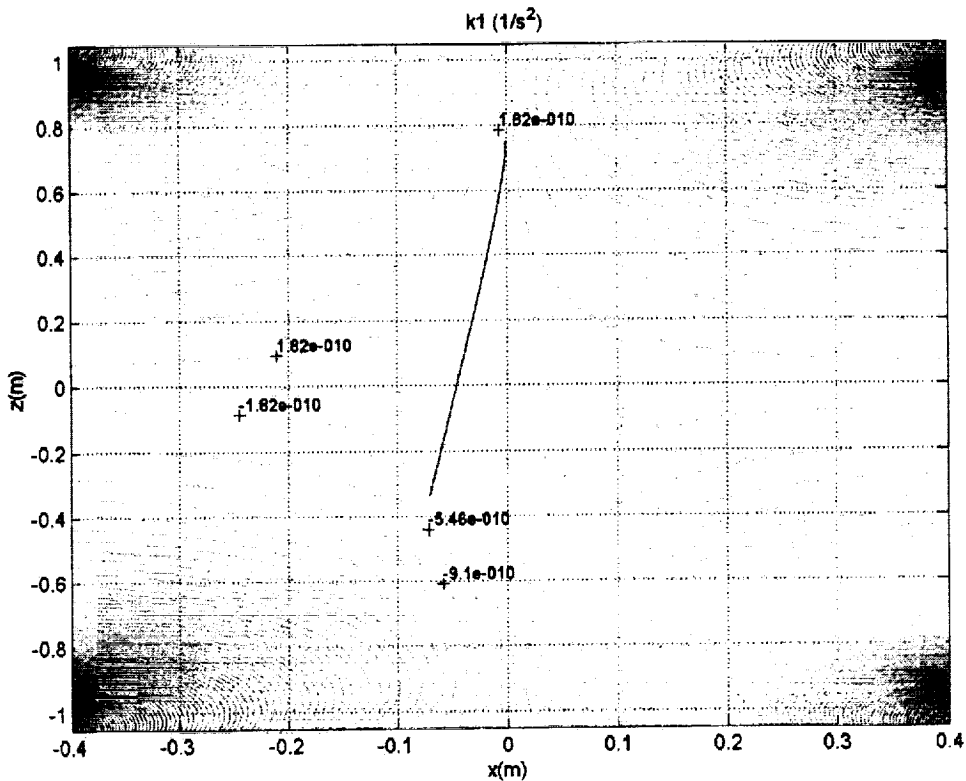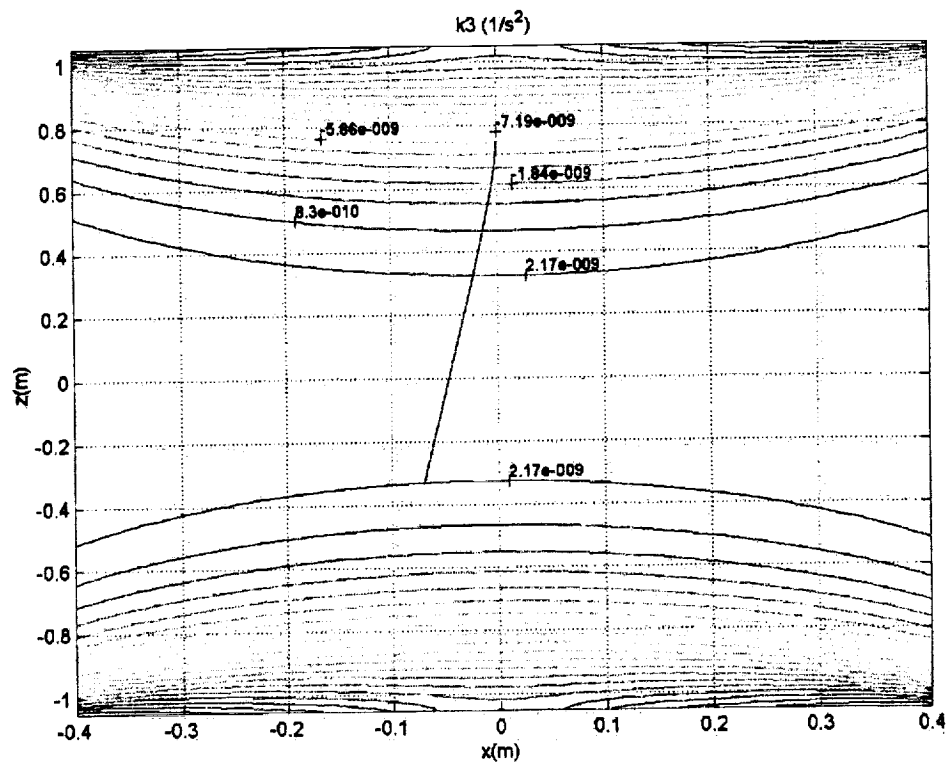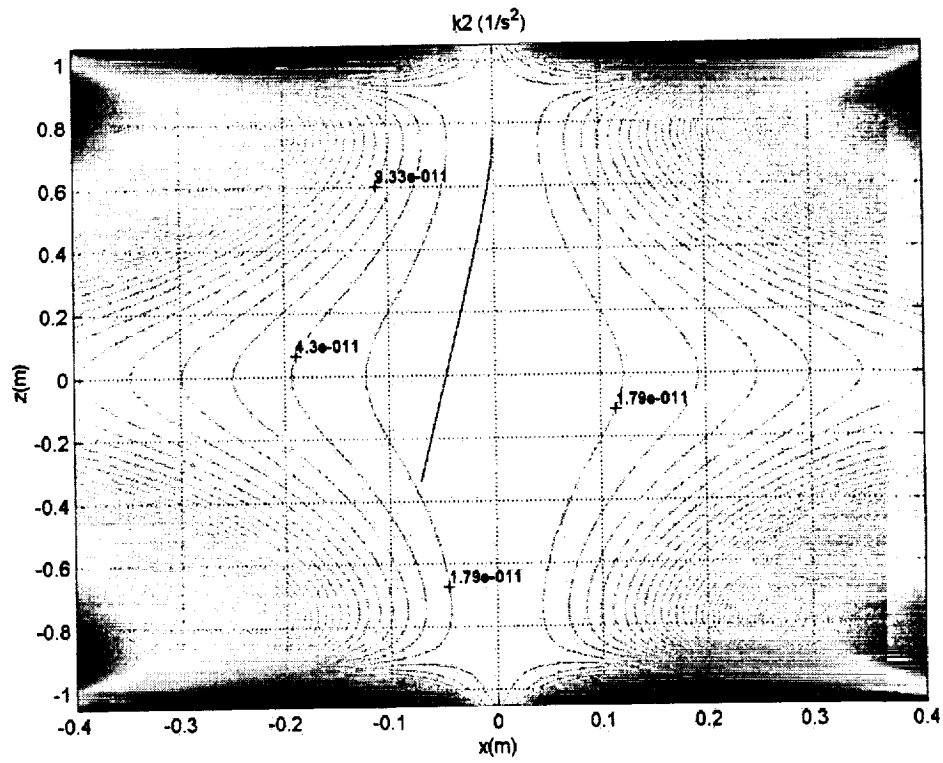
Figure 26 Contour plots of k_1, k_2, k_3 for a cryostat with flat caps and H = 2.3 m, D = 1.2 m and total mass = 500 kg.

The quantities k_1, k_2, k_3 are then computed along the trajectory of the instrument package and the power spectral densities are computed over the free-fall time of 26 s. Results are shown in Fig. 27 where the peaks with frequency $1/t_f = 1/26$ Hz due to the free-fall duration, are clearly visible in the spectra.
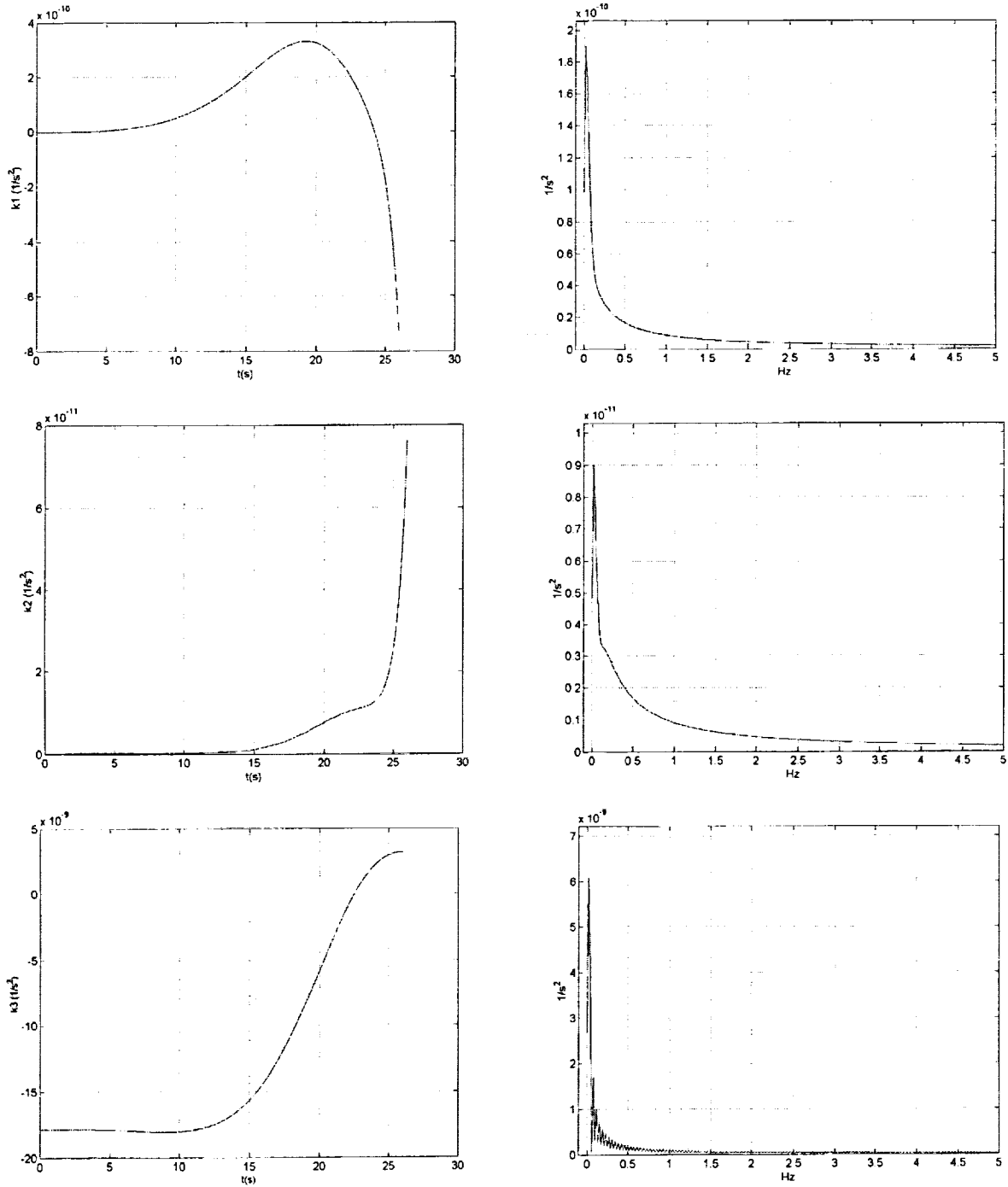
Figure 27 k_1, k_2, k_3 along the trajectory and their spectra.

41

Figure 26 shows that the quantity k_3 is relatively larger than k_1 and k_2. Consequently, eqn. (25) poses a limit for the angle β that defines the capsule attitude with respect to the spin axis of the sensor. After neglecting the much smaller k_2 (and k_1 which depends on $\cos(2\beta)$) we find that the maximum allowable β is:

$$\beta_{max} = \frac{1}{2}\sin^{-1}\left(\frac{\chi_{max}}{k_3}\right) \qquad (27)$$

With a χ_{max} of 10^{-9} s^{-2} and the results shown in Fig. (27), we obtain a limit of 4.8 deg for β, which is a relatively large value.

Cylindrical cryostat with hemispherical caps
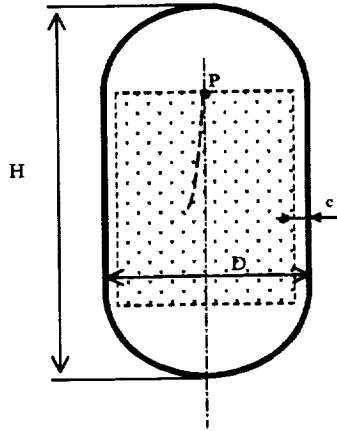
A cylindrical cryostat with hemispherical caps has also been analyzed. The gravity gradient distribution has been mapped on the x-z plane, where x is the cylinder's radial and z the longitudinal axis, between the base of the upper and lower hemispheres and as close as c = 20 cm from the side wall.

The release point P (and starting point for the simulation) lies on the symmetry axis of the cylinder and at the base of the upper hemisphere. The sensor trajectory is the same as in the previous case.

42
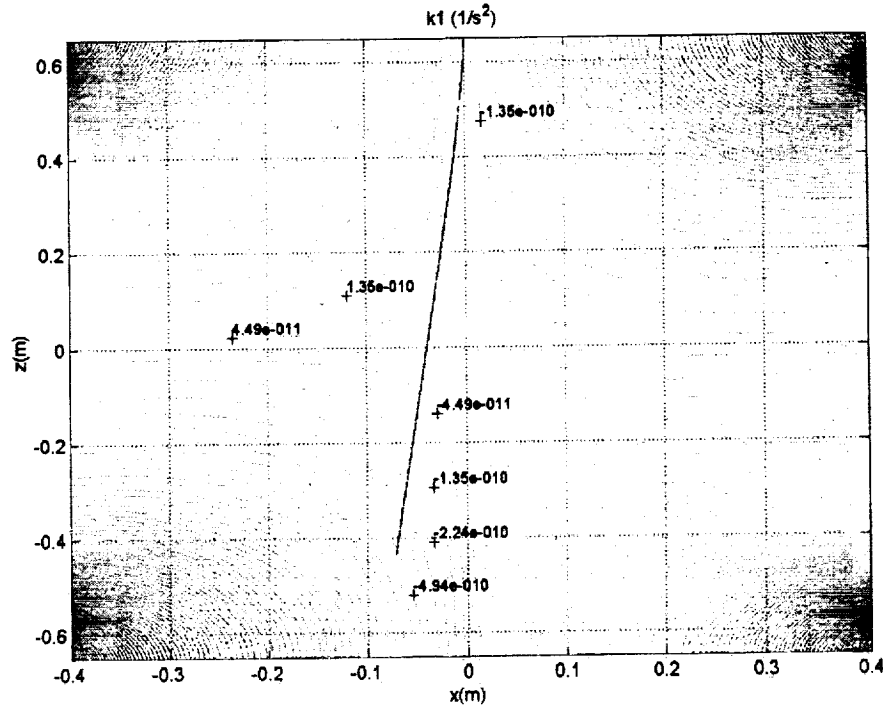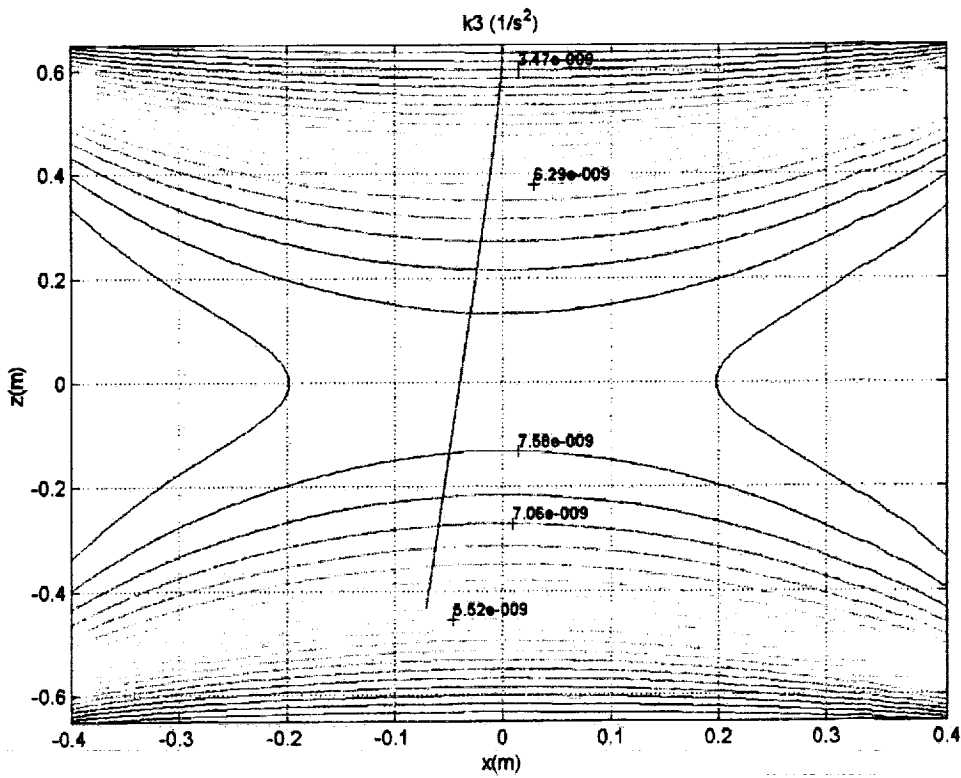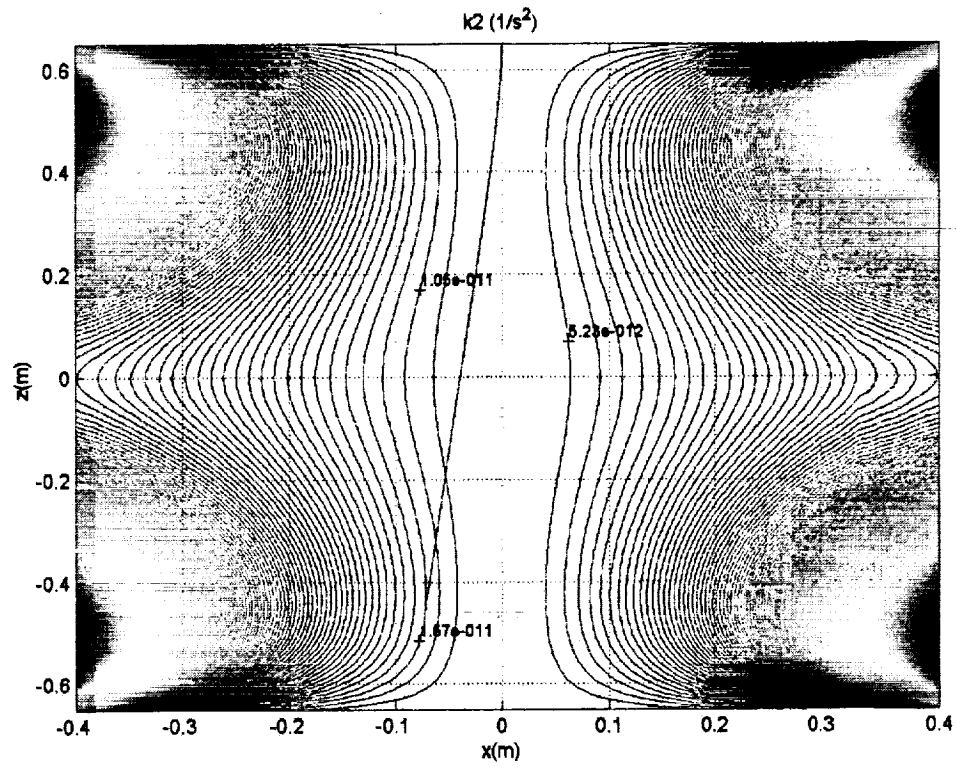
Figure 28 Contour plots of k_1, k_2, k_3 for cryostat with hemispherical caps and $H = 2.5$ m, $D = 1.2$ m and total mass = 500 kg.
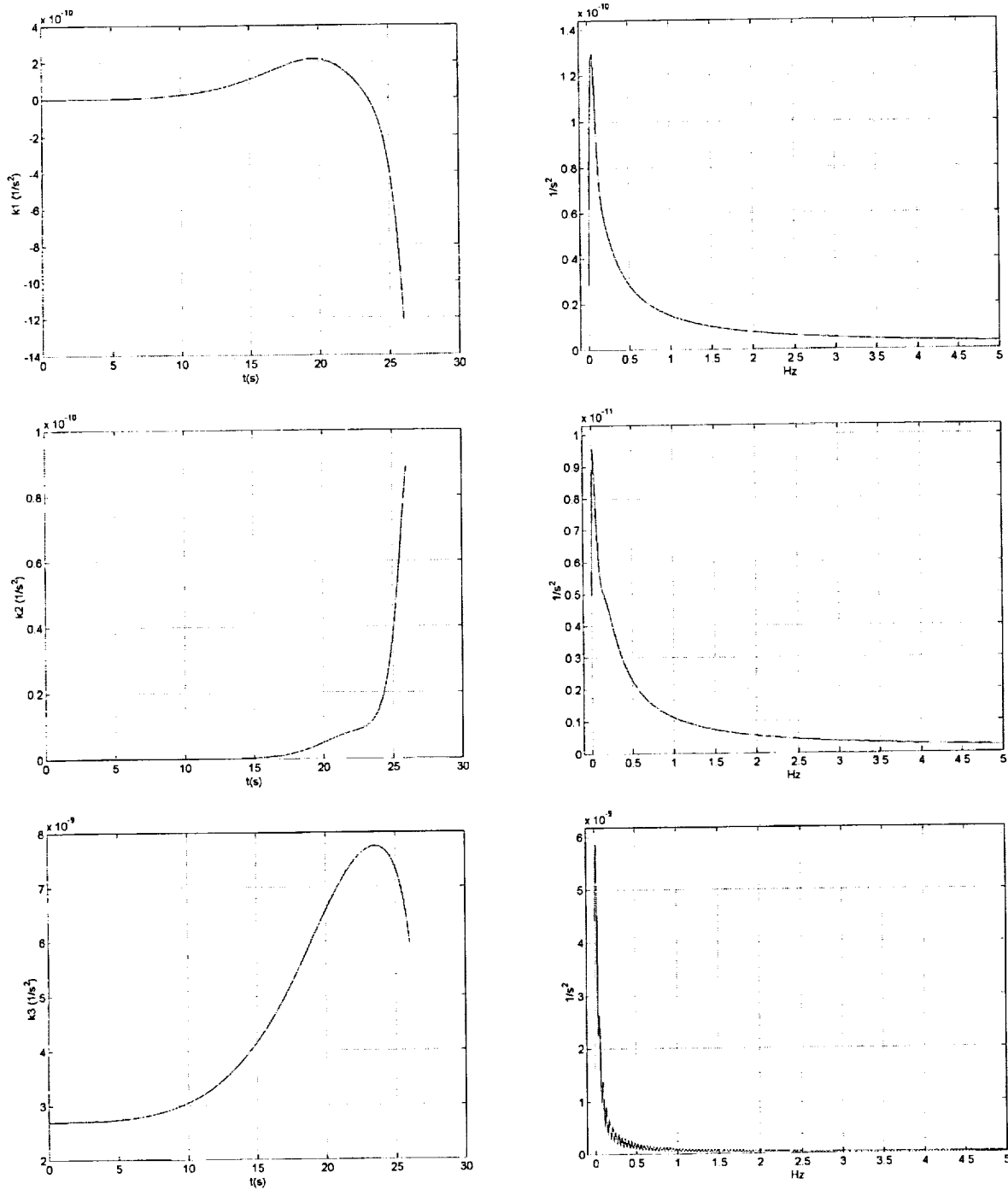
Figure 29 k_1, k_2, k_3 along the trajectory and their spectra.

The analysis carried out here and additional results not shown in this report lead to the definition of a stand-off distance of about 40 cm between the sensor CM and the heavy part of the cryostat walls to provide ω-modulated components of the gravity gradient that are sufficiently low for the sizes and masses relevant to this project.

44

Earth's gravity gradient

We compute here the Earth's gravity gradient tensor and we analyze the effects of Earth's gravity gradient components on a rotating detector with a generic orientation of its spin axis with respect to the gravity gradient field. Let us consider the gravitational potential per unit mass at a point (x, y, z) with respect to the detector's center of mass:

$$V = -\frac{\mu}{\sqrt{(x - R_X)^2 + (y - R_Y)^2 + (z - R_Z)^2}} \tag{28}$$

where R_X, R_Y, R_Z are the components of the radius vector R from the Earth's center to the detector's CM (in which Z is the local vertical) and μ is the Earth's gravitational constant. After projecting about the detector's body axes in which x is the spin axis and calling $\theta = \omega t$ the rotation about the spin axis and ϕ the elevation angle of the spin axis with respect to the horizontal plane:

$$
\begin{aligned}
R_x &= R(t)\sin(\phi) \\
R_y &= R(t)\cos(\phi)\sin(\omega t) \\
R_z &= R(t)\cos(\phi)\cos(\omega t)
\end{aligned}
\tag{29}
$$

The gravitational acceleration in body axes is obtained by substituting eqns (29) into eqn. (28) and computing the gradient:

$$\left(g_x, g_y, g_z\right)^T = -\nabla V \tag{30}$$

The components of the gravity gradient matrix in body axes are finally computed by taking a further derivative with respect to the spatial coordinates, to yield

$$g_{xx} = -\frac{\mu}{R^3}[-2 + 3\cos^2(\phi)] \tag{31.1}$$

$$g_{xy} = 3\frac{\mu}{R^3}\sin(\omega t)\cos(\phi)\sin(\phi) \tag{31.2}$$

$$g_{xz} = 3\frac{\mu}{R^3}\cos(\omega t)\cos(\phi)\sin(\phi) \tag{31.3}$$

$$g_{yy} = -\frac{\mu}{R^3}[1 - 3\cos^2(\phi) + 3\cos^2(\omega t)\cos^2(\phi)] \tag{31.4}$$

$$g_{yz} = 3\frac{\mu}{R^3}\cos(\omega t)\sin(\omega t)\cos^2(\phi) \tag{31.5}$$

$$g_{zz} = \frac{\mu}{R^3}[-1 + 3\cos^2(\omega t)\cos^2(\phi)] \tag{31.6}$$

45

Here again, the components modulated at ω are g_{xy} and g_{xz} (in which x is the spin axis). In other words, if the spin axis lies on the horizontal plane, the detector only sees components modulated at 2ω but if it is not, components modulated at the frequency ω appear. The strengths of these components are proportional to the tilt angle with respect to the local horizon. Note also that the effect of the Earth's gravity gradient on a rotating body can be readily applied to the space-based tests of the Equivalence Principle in which the only difference from the balloon-based experiment is the slightly larger value of the radial distance from the space-based sensor to the Earth's center.

An alternative way of portraying the origin of the ω-modulated components of the Earth's gravity gradient field is by considering the following. If the z-axis of the body reference frame is directed along the local vertical (that is the spin axis x of the sensor is on the horizontal plane) then the gravity gradient tensor is

$$\Gamma^E_{(z=r)} = \frac{GM_E}{R^3} \begin{vmatrix} -1 & 0 & 0 \\ 0 & -1 & 0 \\ 0 & 0 & 2 \end{vmatrix} \tag{32}$$

The tensor does not change under a rotation about the z-body axis due to its structure which reflects a symmetry about the radial line. Consequently, we can choose the azimuth orientation of the spin axis at will (let us call it the y-body axis). A rotation φ about an axis perpendicular to the spin axis produces terms $g'_{xz} = g'_{zx}$ in the transformed tensor:

$$\Gamma^E_\phi = R_\phi \Gamma^E R_\phi^T = \frac{GM_E}{R^3} \begin{vmatrix} g'_{xx} & 0 & g'_{xz} \\ 0 & -1 & 0 \\ g'_{zx} & 0 & g'_{zz} \end{vmatrix} \tag{33}$$

where

$$g'_{xx} = -1 + 3\sin^2\phi$$
$$g'_{zz} = -1 + 3\cos^2\phi \tag{34}$$
$$g'_{xz} = g_{zx} = -3\sin\phi\cos\phi$$

The g'_{xz} and g'_{zx} terms are subsequently modulated at the frequency ω by the rotation θ = ωt about the spin axis as shown previously.

Since there are terms modulated at the signal frequency ω, we have to make sure that they are kept lower than the accuracy with which we want to measure the signal. From the detector point of view, there will be requirements imposed on the centering of the sensing masses and their attitude with respect to the Earth's gravity field as shown in the following section.

46

Disturbances induced by concentrated masses on board the capsule

Let us consider the reference system (x, y, z) fixed to the sensor with origin at the center of mass and with x oriented along the spin axis and let us indicate the position of a point mass m_p in proximity of the sensor in spherical coordinates (δ, γ, ρ) (see Fig. 30).
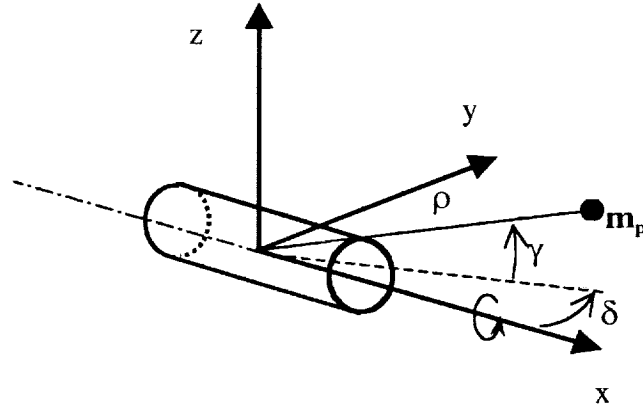
Figure 30 Geometry of the sensing mass and reference frame

The position of m_p is then expressed as:

$$x_p = \rho \cos \delta \cos \gamma$$
$$y_p = \rho \sin \delta \cos \gamma \tag{35}$$
$$z_p = \rho \sin \gamma$$

The gravity gradient matrix at the detector due to the gravity field induced by a mass point m_p is:

$$\Gamma_{m_p} = \frac{G \cdot m_p}{\rho^5} \begin{bmatrix} 3x^2 - \rho^2 & 3xy & 3xz \\ 3yx & 3x^2 - \rho^2 & 3yz \\ 3zx & 3yz & 3x^2 - \rho^2 \end{bmatrix} \tag{36}$$

Considering a sensor that rotates with respect to a fixed point mass in its proximity we obtain the two ω-modulated components already shown in the previous paragraphs:

$$\Gamma'_{12} = \Gamma'_{21} = \Gamma_{13} \sin(\omega \cdot t) + \Gamma_{12} \cos(\omega \cdot t) \tag{37.1}$$

$$\Gamma'_{13} = \Gamma'_{31} = \Gamma_{13} \sin(\omega \cdot t) - \Gamma_{12} \cos(\omega \cdot t) \tag{37.2}$$

47

The moduli of the two ω-modulated gravity gradient components $\Gamma"_{12}$ and $\Gamma"_{13}$ are the same and can be expressed as follows:

$$\chi = \frac{G \cdot m_p}{\rho^5} |x| \sqrt{z^2 + y^2} \tag{38}$$

which shows that the masses located on the plane y-z (i.e., x = 0) do not generate disturbances with the same frequency as the measured signal. Substituting eqn. (35) into (38) and extracting ρ yields the minimum distance for a point mass to produce a disturbing gradient equal to or less than the critical gradient a_{gg-max}:

$$\rho_{min} = \left(\frac{G \cdot m_p}{a_{gg-max}} |\cos\delta\cos\gamma| \sqrt{\sin^2\delta\cos^2\gamma + \sin^2\gamma} \right)^{1/3} \tag{39}$$

Setting a limit of 10^{-9} s^{-2} for a_{max} we plot the locus $f(\rho,\gamma,\delta) = 0$ of the points in space with $a_{gg} = a_{gg-max}$ in Figure 31 for a disturbing point mass of 1 kg. Next, meridian sections (rotated about the z-axis by the meridian angle δ) of the same locus are plotted for different values of the angle δ in Fig. 32 where r is the radial direction.
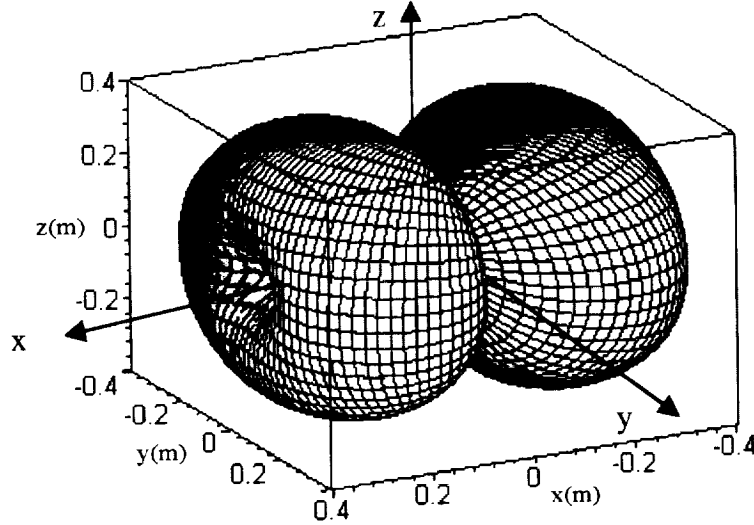
Figure 31 Locus of ω-modulated gravity gradient component with strength = 10^{-9} s^{-2}
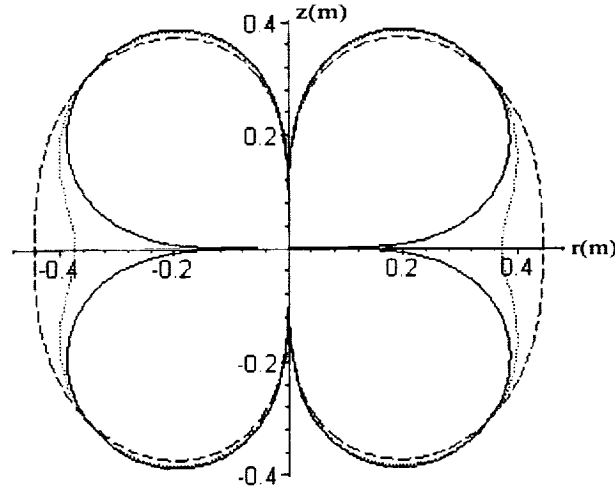
Figure 32 Meridian sections of locus in Fig. 31 for different angles δ [δ = 0 (i.e., y-z plane) - solid black line; δ = 15° - blue dots; δ = 30° - red dash; δ = 45° - gray dash dot]

The worst case meridian section at δ = 45° is plotted for different values of the perturbing mass in Fig. 33.
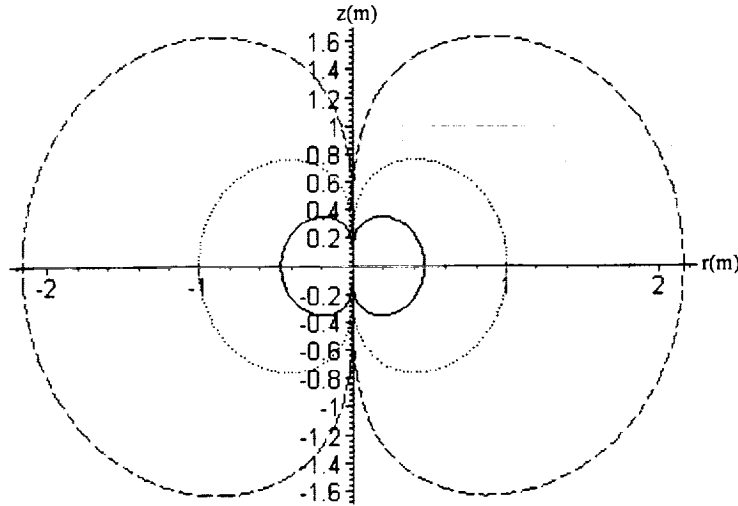
Figure 33 Meridian sections for δ = 45° and different values of perturbing mass m_p (m_p = 1 kg - solid black line; m_p = 10 kg – blue dots; m_p = 100 kg - red dash)

The previous analysis defines exclusion zones for concentrated masses on board the capsule. In general, masses can be placed rather freely on the y-z plane (perpendicular to the sensor spin axis). Masses lying on this plane generate only 2ω-modulated components whose strength only needs to be reasonably smaller than the upper bound of the dynamic range of the sensor. The Earth itself produces such 2ω-modulated components with a strength equal to 3×10^{-6} s^{-2} that is well stronger than the sensor sensitivity (for realistic

values of the sensing mass CMs errors), but is about 3-orders of magnitude lower than the dynamic range of the sensor. For the 2ω-modulated term, the equivalent Earth is a mass of 22,500 kg at 1-m or a 22.5 kg at 10 cm from the sensor.

Requirements related to the ω-modulated components are more stringent and, consequently, we will concentrate on these components which have been dealt with in this analysis. In summary, concentrated masses should be placed as close as possible to the y-z plane (perpendicular to the sensor spin axis). For masses away from the y-z plane, Fig. 33 defines the exclusion zones from the sensor for different mass values under the worst possible condition of masses placed on the 45° meridian plane.

Effect of Gravity Gradients on Differential Acceleration Measurement

The differential accelerometer consists (from the mechanical point of view) of two sensing masses with ideally coincident centers of mass (CM). The equivalence violation signal is measured as a differential displacement along the y-body axis of the sensor which is orthogonal to the spin axis along the x-body axis. In reality the two centers of mass (or more appropriately centers of gravity) do not coincide and CM_2 (i.e., the CM of mass 2) is displaced by a position error vector δ with respect to CM_1 as follows

$$\delta = \begin{vmatrix} \delta_x \\ \delta_y \\ \delta_z \end{vmatrix} \tag{40}$$

We can place the body reference frame at CM_1 and compute the differential acceleration due to gravity gradients by simply multiplying the gravity gradient matrix in body axis , that is

$$\begin{bmatrix} \delta a_x \\ \delta a_y \\ \delta az \end{bmatrix} = \left(\Gamma^E + \Gamma^C + \Gamma^M \right) \begin{vmatrix} \delta_x \\ \delta_y \\ \delta_z \end{vmatrix} \tag{41}$$

where Γ^E, Γ^C, Γ^M are the gravity gradient matrices of the Earth, the distributed capsule mass and concentrated masses on board the capsule, respectively. Since the differential accelerometer measures only the component along the y-body axis, we obtain finally:

$$\delta a_y = (\Gamma^E_{yx} + \Gamma^C_{yx} + \Gamma^M_{yx})\delta_x + (\Gamma^E_{yy} + \Gamma^C_{yy} + \Gamma^M_{yy})\delta_y + (\Gamma^E_{yz} + \Gamma^C_{yz} + \Gamma^M_{yz})\delta_z \tag{42}$$

in which Γ^E_{yx}, Γ^C_{yx}, and Γ^M_{yx} are the components modulated at the signal frequency ω while the other terms in eqn. (42) are modulated at 2ω. In conclusion, the disturbing differential acceleration along y produced by gravity gradients can be expressed as follows:

50

$$\delta a_y < 3\frac{\mu}{R^3}\cos(\phi)\sin(\phi)\sin(\omega t)\delta_x + [(k_2 + k_3)\sin(2\beta) + k_1\cos(2\beta)]\sin(\omega t)\delta_x$$
$$+ a_M(\omega) + f_y(2\omega, \delta_y) + f_z(2\omega, \delta_z) \tag{43}$$

where k_1, k_2, and k_3 are the gravity gradient terms (see previous subsections) generated by the capsule in the capsule-body reference frame, ϕ is the elevation of the spin axis with respect to the local horizon, β is the elevation of the spin axis with respect to the equatorial plane of the capsule, $a_M(\omega)$ is the ω-modulated disturbing acceleration (in functional form) produced by concentrated mass on board the capsule (see previous subsection) and $f_y(2\omega, \delta_y)$ and $f_z(2\omega, \delta_z)$ represent all the other 2ω-modulated components which have been separated in eqn. (43) according to the centering error components. Note that the 2ω-components depend only on the centering errors δ_y and δ_z while the ω-components depend only on the centering error δ_x. The less-than sign in eqn. (43) is due to the fact that, on the right hand side of the equation, we have adopted the strongest value of the ω-modulated gravity gradient component of the capsule, that is, for $\alpha = 0$ (see Fig. 15). Moreover, from the analysis of the capsule gravity gradients, we have concluded that if we keep the sensor (at the CM) about 40 cm away from the heavy part of the chamber/cryostat walls, the ω-modulated gravity gradients are well below the critical value of about 10^{-9} s^{-2}. Based on similar reasoning, we assume that the concentrated masses on board the capsule are placed outside of the exclusion zones (defined in the previous subsection) in order to keep them below the critical value. In other words, an appropriate design and a careful mechanical construction of the sensing masses (δ_x of order microns) will make the gravity gradient contribution of the capsule and the concentrated masses on board the capsule negligible.

To attenuate the effect of the gravity gradient of the Earth we have to make sure that the product $\sin(\phi)\cos(\phi)\delta_x$ is sufficiently small. In other words we can trade the position error between the CMs of the sensing masses along the spin axis δ_x for the tolerable angle ϕ of the spin axis with respect to the local horizontal. For small values of ϕ, we readily compute that for the first term on the right hand side of eqn. (34) to be smaller than, let us say, 10^{-15} g, the product $\phi\delta_x$ must be smaller than 0.1 deg-μm. This requirement must be considered in the design of the detector, the release mechanism, and the capsule leveling system of the capsule. The complexity of some subsystems can be traded for the simplicity of other subsystems among those three.

Following the procedure of the *STEP* project, we have estimated the pressure requirement inside the detector casing (small vacuum chamber) for keeping the radiometer effect and the damping due to residual gas to tolerable levels.

Effect of residual gas

A limit on the tolerable pressure difference Δp inside the instrument package can be obtained by requiring that the acceleration $a = A\Delta p/m_{eff}$ produced by the air piston effect (*dc* signal) on the surface A of each sensing mass[xxii] be at least three orders of magnitude smaller than the dynamic range of the differential accelerometer. Consequently, for A $\approx$ 0.012 m^2 and $m_{eff} = 9$ kg, the tolerable pressure difference should be less than 10^{-9} Pa (10^{-11} mBar).

Radiometer effect

The maximum tolerable pressure is also related to the maximum allowable thermal gradient through the radiometer effect, i.e., the acceleration produced by gas molecules emitted from regions with different temperatures [Ref. x]. This effect is likely to produce an acceleration error modulated at the signal frequency because, as the instrument package rotates, it could face regions with slightly different temperatures. The acceleration produced by the radiometer effect is $a = p \ (\Delta T/\Delta x)/(2\rho T)$ [Ref. x] where p is the pressure, T the temperature and ρ the density of the sensing mass. For $\rho = 2800$ kg/m^3 (Aluminum), $p = 10^{-9}$ Pa is required for an acceleration error of 10^{-15} g and a temperature gradient of 0.2 K/m.

A thermal gradient across the detector also affects the resonant frequencies of the sensing masses through variations of: the Young's modulus of the material, the geometry of the torsional springs, and the moments of inertia of the sensing masses. Consequently, a thermal gradient changes differentially the resonance frequencies of the sensing masses and ultimately affects the common mode rejection factor.

The common-mode rejection factor is related to the temperature variation ΔT across the detector as follows CMRF $\approx |\alpha + \alpha_E|\Delta T$ where α is the thermal expansion coefficient and α_E the thermal coefficient of the Young's modulus. For Aluminum at low temperatures $\alpha \ll \alpha_E$, $\alpha_E \sim -3.5 \times 10^{-4}$ K^{-1} [xxiii] while CMRF is required to be $\leq 10^{-4}$. Consequently, the tolerable temperature gradient for a 0.4-m-long detector must be smaller than 0.7 K/m. This value is somewhat less stringent than the tolerable value of the thermal gradient dictated by the radiometer effect and consequently is superseded by the previous effect.

Thermal issues and design

Thermal issues, however, are not solved by simply meeting the thermal gradient requirement and lowering the pressure. The experiment has two cold parts, that is, the

proof masses plus casing (i.e., the sensor) and the preamplifier and a component at almost room temperature (inside its case), that is, the electronics box which includes battery and various housekeeping functions.

The sensor has negligible thermal dissipation while the preamplifier and electronic boxes have non-negligible thermal dissipations. We need to evaluate the following: (1) cooling down time for the sensor and preamplifier before launching the balloon; (2) the tolerable temperature drifts of the detector, the preamplifier and the electronics during the measurement phase after release; and (3) the tolerable temperature drifts of the same units before release during the check out phase.

Experimental data was provided by our partners at IFSI on the power consumption of the units involved and their sensitivity to temperature variations. Not surprisingly, the sensor and the preamplifier have the highest temperature sensitivity, of order 10^{-8} g/K and 10^{-9} g/K, respectively, followed by the electronics which is a few orders of magnitude less sensitive. If the two sensitivities quoted above are taken at face value, the temperature variation over the measurement time should be less than 0.1 μK! In reality, the sensor and preamplifier will be grounded to the cryostat temperature before release and then they will rely on their own thermal inertia during the 25-30 s measurement phase. The temperature drift is slow, with a time constant that is typically two orders of magnitude bigger than the measurement time. Since variations of less than μK are unrealistic to obtain, the question can be put as follows: how well an acceleration signal at the expected sensitivity can be extracted from a slow varying background (dependent on the temperature drifts) which increases by several orders of magnitude over the measurement time?

Answering this question is important to define more realistic requirements for the thermal design, in general, and for solving point #2 outlined above, in particular. In order to answer this question we have investigated techniques of signal extraction from a noisy signal which also drifts by a very large amount due to temperature variations.

This exercise is not meant to be a comprehensive work on the techniques that will be adopted for extracting the signal from noise but rather it is limited to the issue described previously. In summary, we have taken a sample 0.5-Hz signal with a strength of 2×10^{-15} g (at 95% confidence level), added to a random noise with $\sqrt{30} \times 10^{-15}$ g rms and to a double-exponential (other functions have also been tested) drifting acceleration that ramps up to an acceleration intensity many orders of magnitude bigger than the signal. The double exponential (or similar function) represents the different heating rates of the sensor and the preamplifier with two different time constants TC_1 and TC_2 where we have assumed $TC_1 > TC_2$ to account for the sensor's bigger thermal inertia We have practiced a basic technique to extract the signal, without assuming any knowledge of the functional expression of the thermal drift, for increasing steepness of the thermal ramp (that is the rates of change of the two temperatures).

Fig. 34 shows a conservative situation in which the thermal-induced acceleration ramps up to 2×10^{-8} g, that is, its maximum value is 7-orders of magnitude bigger than the expected signal. The signal could be extracted with reasonable ease by detrending the

signal + noise with a 6-order polynomial and computing the FFT of the detrended signal. This extraction process would not succeed for much stronger thermal drifts, although no additional effort was devoted to improving the process because the results obtained were already satisfactory. After considering these results, we can establish thermal drift requirements for the relevant units as follows:

Sensor temperature drift: < 0.0067 K/s (i.e., ~0.2 K in 30 s)

$$(44)$$

Preamplifier temperature drift: < 0.017 K/s (i.e., ~0.5 K in 30 s)

For the temperature of the electronic box we can safely assume that it is sufficient to keep the temperature variation below a few degrees over a 30 s maximum free-fall time.
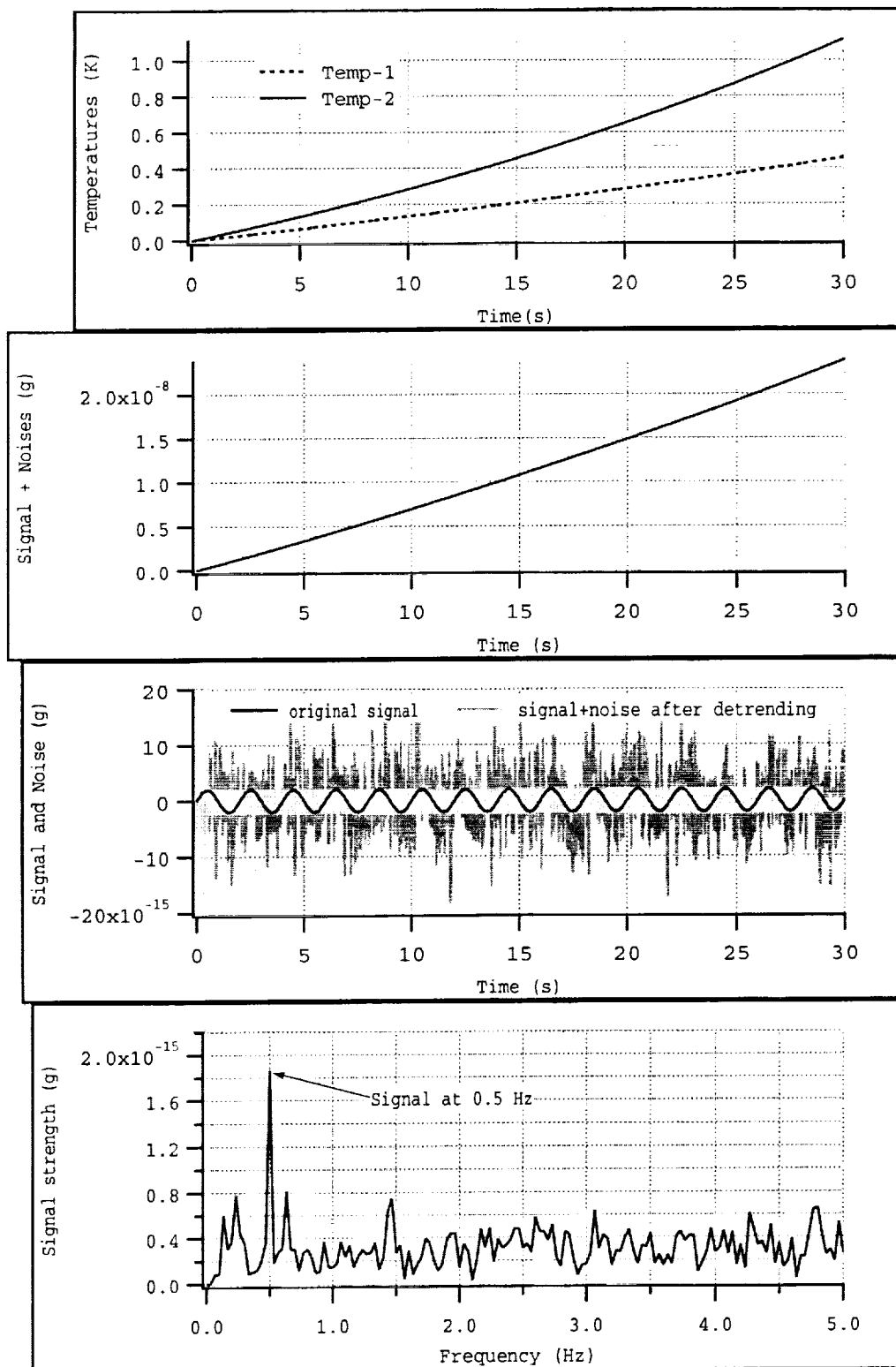
Figure 34 Example of extraction of signal from random noise plus a strongly-dominant slow-drifting acceleration noise (Temp-1 = sensor and Temp-2 = preamplifier).

55

Preliminary Thermal Results

There are 3 elements that operate at different internal temperatures in the instrument package, namely, the detector, the preamplifier and the electronic box. The detector should be at the lowest possible temperature with an upper limit of 10 K. The Gallium Arsenide FET preamplifier can operate from low temperature (> 10 K) up to room temperature with slightly reduced performance at high temperature. The electronic box must be kept close to room temperature. The three boxes also dissipate different amounts of power. The power dissipated by the detector W_1 is in the nW range which is negligible. The power dissipated by the preamplifier and the electronic box are typically $W_2 \approx 100$ mW and $W_3 \approx 500$ mW which are both non negligible. A simplified thermal scheme of the three elements is shown in Fig. 35.
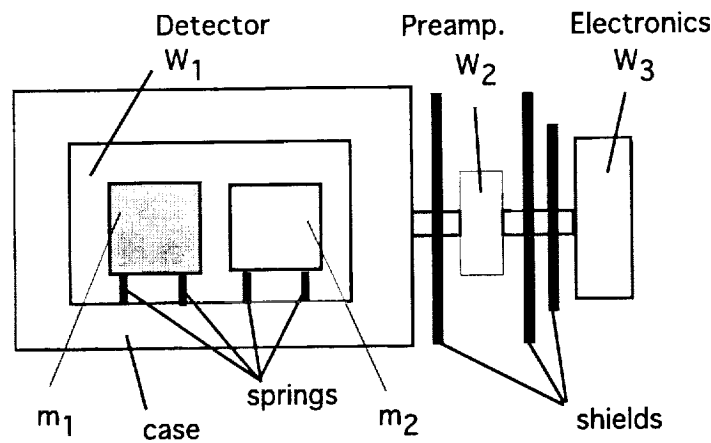
Figure 35 Simplified thermal scheme

A preliminary thermal analysis was carried out by using a finite-difference thermal analysis code to address the two more critical thermal issues, that is: (a) the cooling down of the detector and (b) the temperature rise of the preamplifier during the measurement phase.

Results of the cooling down are shown in Fig. 36 under different assumptions of radiation and conduction through a cold strap with a conductance of 0.02 W/K connecting the case of the detector to the cryostat. The most relevant results are those shown in Fig. 36(a) while Figs. 36(b) and 36(c) represent cases that were run to assess the relative contributions of radiation and conduction, respectively. As shown by Fig. 36(a) the cooling time needed, with the cold strap, to reduce the temperature below 10 K is shorter than a week.
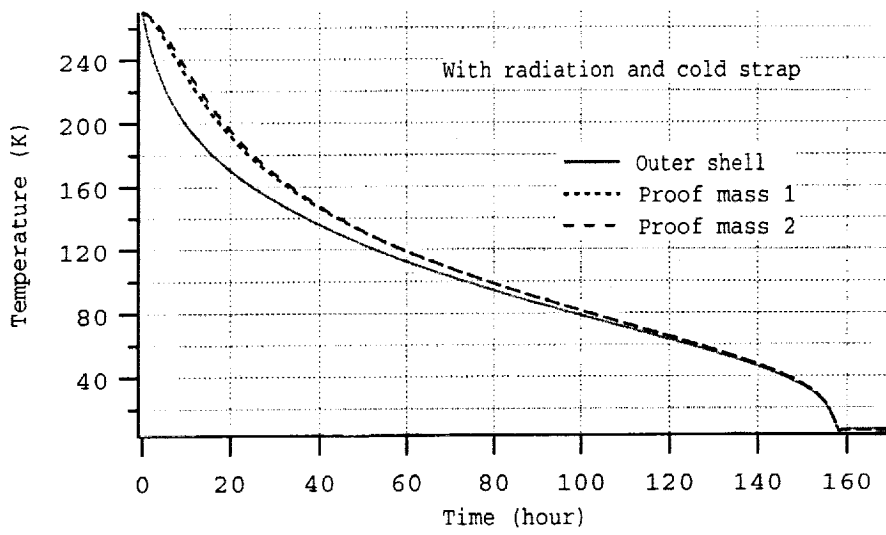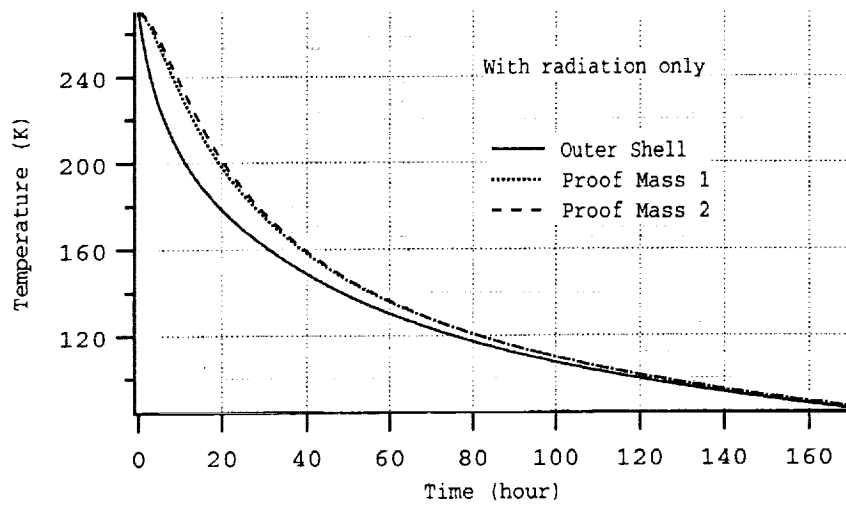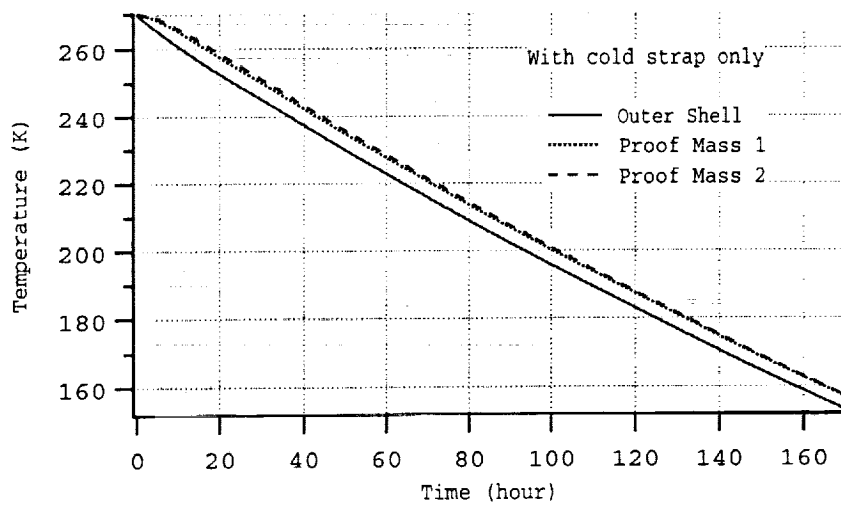
Figure 36 Temperatures of detector during cool down under various assumptions

The second critical issue that we addressed is the temperature rise of the preamplifier during free fall (i.e., the measurement phase). The preamplifier was singled out as more critical, from the thermal point of view, than the detector because it has high power and low mass while the detector has negligible power dissipation and higher mass. We assumed that the preamplifier is at its desired temperature value (between 10-20 K) before the instrument package release and that a thermal shield is interposed between the preamplifier box, which is attached to a thermal radiator, and the detector.

(a)

(b)
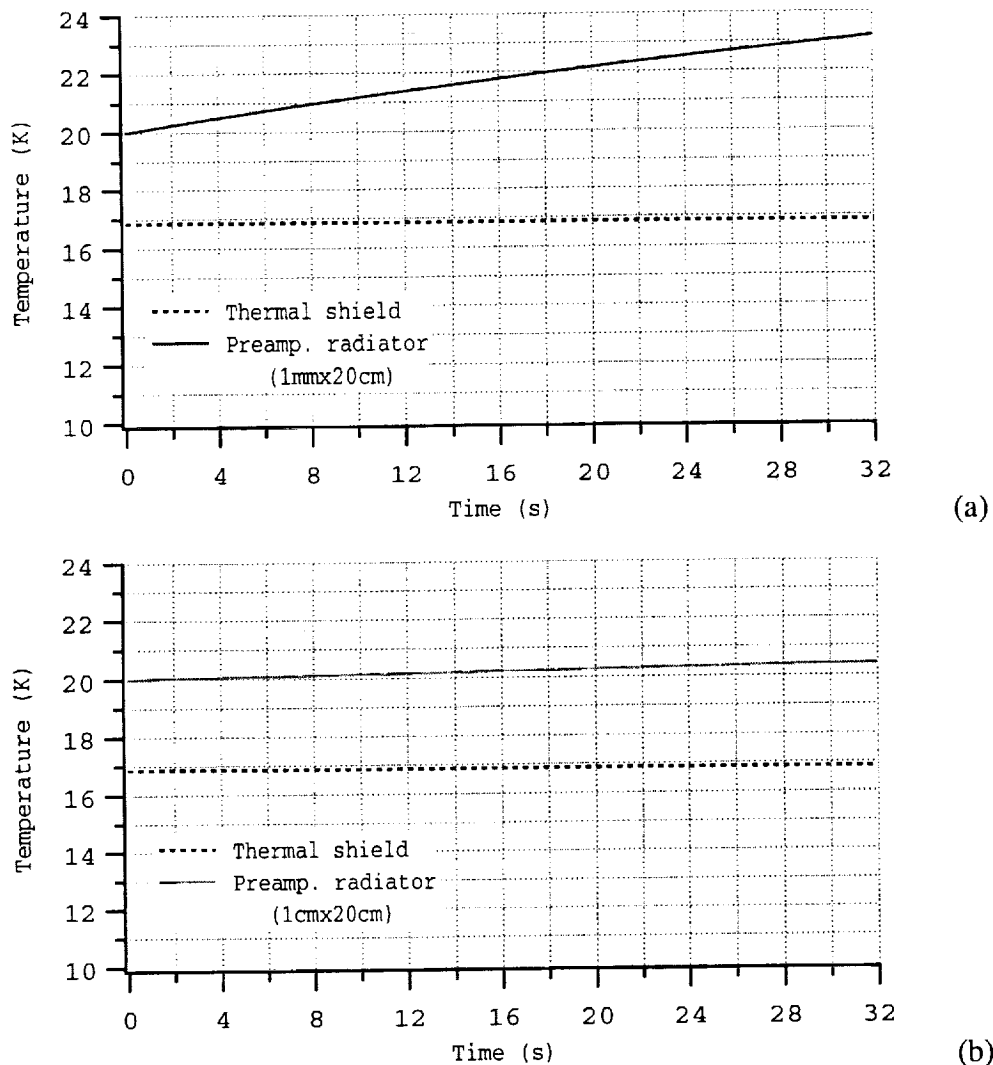
Figure 37 Temperature of preamplifier and thermal shield during free-fall phase

Fig. 37 shows the results for different thicknesses of the thermal radiator. Clearly, in order to keep the temperature variation below 0.5 K during a 30-s time, a 1-cm (thick) x 20-cm (dia.) radiator is required. Additional thermal analyses will be performed to compute temperature variations of the three connected boxes and, consequently, define in more detail the thermal design beyond this preliminary analysis of critical issues.

CAPSULE/CRYOSTAT DESIGN APPROACH

Introductory Remarks

During the early conceptual development of this experiment, we were focusing our attention mostly on free-fall spans of a few meters to achieve free-fall time as long as possible. This situation, however, precluded the use of a fully cryogenic capsule because of mass considerations and pushed us towards the adoption of a small cryostat at the top of the vacuum chamber to refrigerate the instrument before release. However, the small cryostat creates additional problems which are highlighted by the previous analyses as follows: (1) the small cryostat is a concentrated mass very close to the detector which produces relatively strong gravity gradients; and (2) the instrument package spends most of the free-fall time in the vicinity of the small cryostat and distances itself from the small cryostat only in the later portion of the fall.
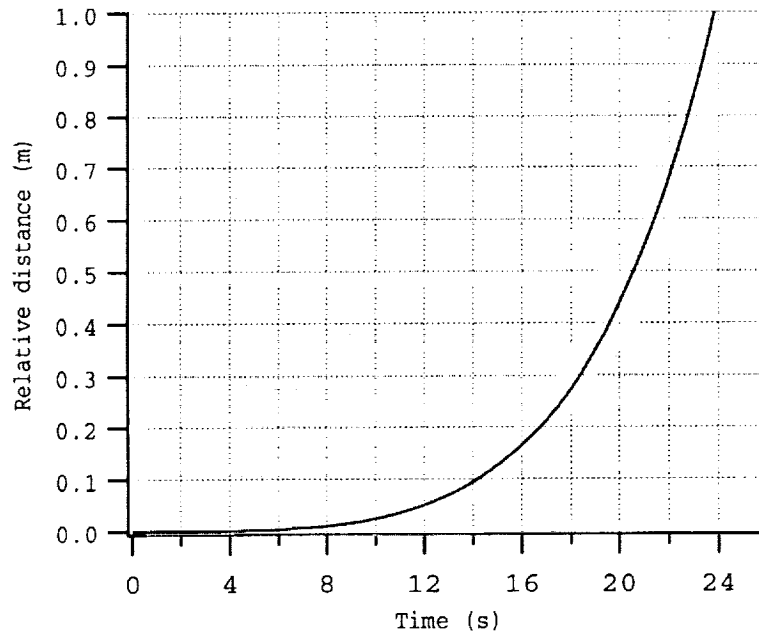
Figure 38 Vertical motion of package relative to capsule for $\beta_0 = 7000$ kg//m^3 (shown for distances < 1 m)

Fig. 38 shows clearly that the relative distance between the instrument package and the capsule (for a typical $\beta_0 = 7000$ kg/m^2) is less than 10 cm during the first 14 s, increases to about 1 m at the 24 s mark and becomes greater than 3 m at the 30 s mark (not shown in the figure). In other words, the small cryostat can not be small either from the point of view of reducing the self-generated gravity gradients and also for allowing for lateral motions of the capsule with respect to the falling package. The free fall time (once several seconds are spent in attenuating the initial transient motion of the sensing masses after release) affects the experiment accuracy only through its square root (i.e., a weak function). Consequently, it is sensible to sacrifice a few seconds of free-fall time in order

to make the experimental area sufficiently short to open up the option of a fully cryogenic vacuum chamber for the detector to fall in.

These considerations are formalized in the next section by developing an optimization process aimed at identifying the size and mass of the experimental chamber and the capsule.

Optimization of Capsule Size and Mass

A design optimization would appear premature at this point of the flight definition study. This optimization process, however, is aimed exclusively at evaluating consistently the size of the capsule and its overall mass. The goal of the optimization process is to devise a mathematical formulation for evaluating capsule sizes and masses that satisfy: (1) geometrical/dynamical constraints and (2) engineering constraints. The first category includes the constraints determined by the strength of the gravity gradient inside the vacuum chamber (generated by the capsule mass itself) and from the motion of the instrument package with respect to the capsule during free fall. The second category includes size constraint due to transportability and handling of the capsule and also minimum and maximum allowable mass. The minimum mass is related to the ability of building a vacuum chamber that does not buckle under the atmospheric pressure while the maximum mass is limited by the carrying capacity of the helium balloon.

The independent variables to work with (as it will become clearer in the following) are the (frontal) low-speed ballistic coefficient of the capsule and the free-fall time. The output variables are the capsule diameter and related capsule length, free-fall span, cryostat mass, and capsule mass.

In more detail, we first need an expression of the free-fall span of the package inside the capsule as a function of the ballistic coefficient β_0 and the free-fall time T_f. The free-fall distances were derived numerically because the relevant functions are not integrable. Consequently, we have to fit the numerically-derived function over the two parameter space (β_0, T_f). The fitting was done successfully over the range of interest of the parameters by starting from the analytical formulation that approximates the solution for a constant ballistic coefficient and then evaluating the fitting coefficients for the general case with variable C_D. The two-parameter fitting process yields:

$$z_f = a T_f^{\,b} \exp(c T_f^{\,2}) / \beta_0 \tag{45}$$

where a = 0.149636, b = 3.084, and c = 0.001692 are the fitting parameters. The results are accurate within a few percent for ballistic coefficients varying from 2000 kg/m^2 to 20000 kg/m^2 and free-fall times from 0 to 30 s.

The free fall vertical distance readily determines the minimum length of the experimental chamber which must at least equal the free-fall span plus the vertical size (outer diameter) of the instrument package, that is:

$$L_{min} = \eta z_f + D \tag{46}$$

where D is the outer diameter of the instrument package and η is a safety coefficient (typically equal to 1.5) that takes into account the uncertainties in estimating the drag deceleration due to the rarefied atmosphere.

The next step is to evaluate the minimum internal diameter of the chamber/cryostat that can accommodate the lateral and attitude dynamic of the capsule and also provide low values of the gravity gradients along the free-fall trajectory. In order to keep the equations manageable we adopt for this analysis the constant stand-off distances which were derived previously and boundary values for the capsule attitude dynamics, rather than using integration of capsule dynamics and on-line numerical computations of the gravity-gradient field (as done in the previous section). The goal is to compute a minimum value of the internal diameter and external diameter (where the two are related through the cryostat thickness) that keep the free-falling package close to the capsule center-line (far away from the cryostat walls) under the action of a maximum wind shear and for reasonable assumptions about the capsule attitude (pitch or roll) dynamics during the fall. The point above can be translated into the following equation for the external capsule diameter:

$$D_{min}^{ext} = 2\left(y_{pitch} + y_{shear} + y_{gg} + y_{cryo}\right) \tag{47}$$

$y_{pitch} = z_f \sin(\theta_{max})$ where z_f is given by eqn. (45) and θ_{max} can be interpreted as either a limit value of the maximum pitch motion of an uncontrolled capsule or a requirement imposed on the control system of the capsule attitude during the fall. The lateral displacement due to wind shear $y_{shear} = f(\beta_0, T_f)$ is given by eqn. (10) while y_{cryo} is the thickness of the cryostat wall of 10-15 cm (i.e., typical values for large-size helium cryostats). The stand-off distance y_{gg} is the upper bound of the minimum distance between the detector CM and the heavy walls of the cryostat that defines an area (cylindrical and centered at the cryostat center-line) where the gravity gradients generated by the cryostat are sufficiently low. An upper bound of 0.4 m can be adopted across a variety of cylindrical cryostats for sizes and masses of interest to this project.

One obvious consideration is that the internal diameter must be large enough to contain the instrument package. This constraint, however, is already accounted for by the fact that $2y_{gg} > w_P$ where w_P is the width of the instrument package that is presently estimated at about 40 cm. The overall length of the capsule is related to the external diameter through the fineness ratio that, as explained previously, needs to be about 1:4 in order to keep low the value of the drag coefficient, especially in the compressible flow regime.

The next step is to estimate the minimum mass required for the cryostat. Most of the cryostat mass is for the metal of the vacuum chamber that has to withstand the external atmospheric pressure (at ground level). From engineering formulas for the buckling of cylindrical vacuum chambers we obtain that the critical thickness of the vacuum chamber walls (at buckling) is given by:

$$\frac{s_{crit}}{R} = \left[\frac{p_e(L/R)}{0.92E}\right]^{\frac{1}{2.5}} \tag{48}$$

where R and L are the radius and length of the vacuum chamber, s_{crit} is the (minimum) thickness of the load-bearing shell, E is the Young's modulus of the material and p_e the external pressure. The cryostat length is readily computed as:

$$L = \eta z_{ff} + 2y_{gg}$$ (49)

The minimum cryostat mass is then computed as follows:

$$M_{cryo}^{min} = vs_{crit}\pi\rho D(D/k + L)$$ (50)

where ρ is the density of the material, D the cryostat average diameter, v is a load safety factor and k is a shape factor that is equal 2 for flat cryostat caps and 1 for hemispherical caps. After adopting $v = 3$ and eqn. (48) to compute the thickness, we find that eqn. (50) provides masses which are in line with actual values of large cryostats (as verified with Janis Research). Since the cryostat is the heaviest component of the capsule, we can estimate the overall (minimum) mass M_{crit} of the capsule as a proportion of the cryostat mass $M = \gamma M_{cryo}$.

The actual mass of the capsule M, however, is defined by the ballistic coefficient β_0 once the external diameter of the capsule is determined as follows:

$$M = \beta_0 C_{D0} A$$ (51)

where A is the frontal area of the capsule computed through eqn. (47).

Consequently, we must verify that $M > M_{crit}$. If the inequality is true we can simply add ballast to the capsule in order to preserve the values of the geometrical variables and meet the actual mass requirement. In this case, the vacuum chamber of the ballasted capsule will satisfy the strength requirements captured by eqn. (48). If the inequality is violated, the total mass determined by the ballistic coefficient is too small to build a cryostat that is strong enough to withstand the atmospheric pressure. The violation of this inequality will be dealt with in the optimization process as a (strong) penalty on the cost function as explained later on.

Fig. 39 shows an example of a contour plot of two of the key output variables, that is, the capsule mass and the capsule external diameter vs. the low-speed ballistic coefficient and the free-fall time for realistic values of parameters.
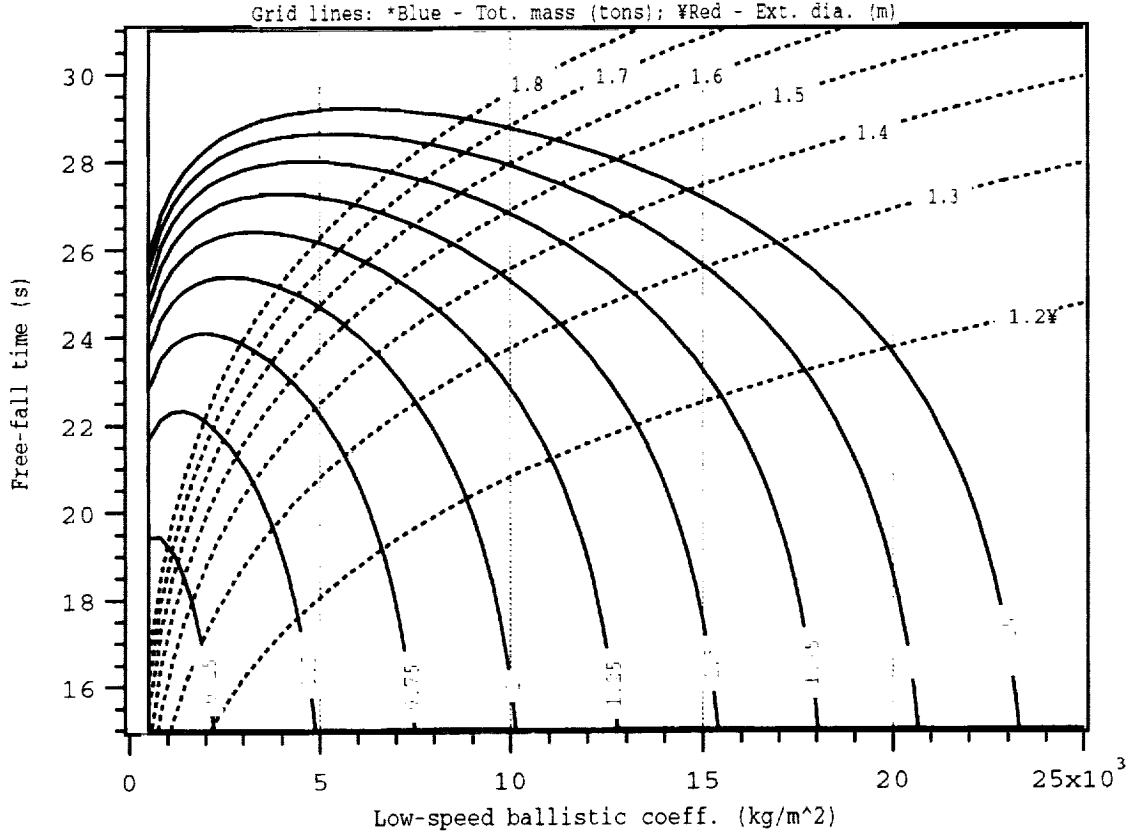
Figure 39 Contour plot with grid lines showing capsule mass and external diameter vs. low-speed ballistic coefficient and free-fall time.

The goal of the optimization process is to define the size and mass of the capsule that minimize the value of a cost function. The cost function consists of the overall capsule mass, the capsule diameter (which is related to the overall capsule length), and the free-fall time. The cost function for this optimization problem can be expressed (and the choice is not uniquely defined) as follows:

$$CF = \frac{a_1 M + a_2 D_{ext}}{\sqrt{t_f - t_{min}}} + P_M + P_D \qquad with \quad t_f \neq t_{min} \tag{52}$$

where M and D_{ext} are the overall mass and external diameter of the capsule, z_f is the free-fall span inside the capsule (which defines the cryostat length), t_{min} the minimum desired free-fall time, t_f the free-fall time, a_1 and a_2 are weighting coefficients and P_M and P_D are penalty functions. P_M is the penalty function for the total mass and P_D for the external diameter.

The structure of the cost function is readily understood after considering that the experiment accuracy depends on the square root of the integration time. The minimum free-fall time has to include the time required to damp initial transients (a few seconds) and also a minimum number of cycles needed for a reliable extraction of the signal from noise. The weighting coefficients adjust the relevant weights of the two quantities at the

63

numerator by making them comparable and/or making one component more important than the other one. By adopting meters for the units of length and metric tons for the units of mass, the two weighting coefficients have the same order of magnitude.

Going back to the penalty functions, obviously the overall mass of the capsule must be greater than the minimum (or critical) mass M_{crit} determined previously and smaller than the maximum mass M_{max} than a reasonable size balloon can carry to an altitude of 40 km. Note that M_{max} is a fixed value while the critical mass depends upon the optimization parameters.

In a similar manner, the external diameter (which also determines the overall length of the capsule according to $L_c = D_{ext}/\delta$) must be large enough to accommodate the instrument package plus the cryostat walls (i.e., larger than D_{min}) and smaller than a maximum value D_{max}. In this case both values are fixed and moreover the first inequality (larger than) is superseded by eqn. (47) if $2y_{gg} > w_p$.

The penalty functions are bowl-shaped functions which are equal to zero for values within the two boundaries of the inequality and whose value rapidly increases as the input variable approaches the boundary values. Fig. 40 shows the mass penalty function for two values of M_{crit} = 0.3 ton and 1.0 ton, respectively, and M_{max} = 2.2 tons. The maximum value of the penalty function is quite arbitrary. It simply needs to be quite a bit larger than the expected range of values of the first term that appears on the right hand side of the cost function in eqn. (52).
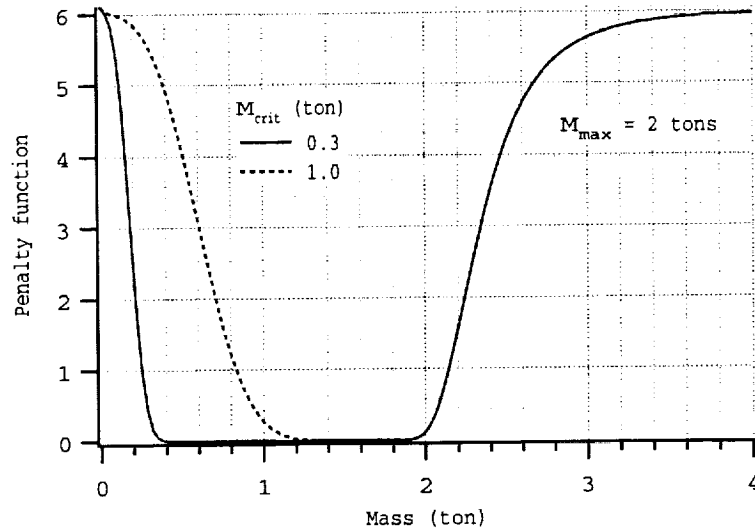
Figure 40 Example of mass penalty function with M_{crit} = 0.3 ton and 1.0 ton, and M_{max} = 2.2 ton.

A similar penalty function with fixed-valued left and right boundaries was derived to penalize the external diameter of the capsule. Without going into excessive details, the penalty functions are obtained from a pair of exponential functions with a set of parameters and power exponents that shapes the function appropriately.

Optimization Results

The optimization routine has been exercised for a large number of cases in order to inspect the influence of any given input parameter on the output/design parameters and the cost function. In the following we will show only the most important results relevant to: (a) a cryostat made of Aluminum and (b) a cryostat made of Steel. The numerical parameters adopted for computing the results shown in Figs. (38) and (39) are as follows: instrument package width $w_P = 40$ cm; low-speed drag coefficient of the capsule $C_{D0} = 0.1$; fineness ratio of the capsule $\delta = 0.25$; wind shear $= 0.005$ m-s^{-1}/m; wall thickness of cryostat $= 15$ cm; stand-off distance for reducing gravity gradients $y_{gg} = 40$ cm; uncertainty factor on drag deceleration $\eta = 1.5$; strength safety factor for vacuum chamber $v = 3$; mass ratio capsule-mass/cryostat-mass $\gamma = 2$; density of material $\rho = 2800$ kg/m^3 (Aluminum) and 7800 kg/m^3 (Steel); Young's modulus $E = 80$ GPa (Aluminum) and 200 GPa (Steel). Moreover, the maximum capsule mass for a mass penalty in the cost function is equal to $M_{max} = 2200$ kg. The maximum external diameter of the capsule for a penalty is $D_{max} = 2.2$ m (which implies a maximum capsule length of 8.8 m). The weight coefficients have been as follows: $a_1 = 1$ (mass) and $a_2 = 1.5$ (external diameter) in which masses are expressed in metric tons and diameters in meters. More weight has been given to the diameter rather than to the total mass because as it will be seen later on there is a fairly large mass margin (large balloons can carry a few tons) while a large external diameter leads to long capsules that are difficult to handle and transport.

In Figs. 41 and 42, the value of the cost function is shown as black contour lines and the contour regions are colored with the deep blue color corresponding to the minimum of the cost function. The grid lines of the free-fall span are also added to the figures in green color. The figures provide a host of useful information as the grid lines specify the values of key variables such as capsule mass, external diameter, and free-fall span (of the instrument package inside the capsule) for any point identified by the coordinate β_0 and t_f. The equations shown previously then enable us to compute readily other key design parameters: the cryostat length L from eqn. (49) and its mass by dividing the capsule mass by γ.

Fig. 38 shows the results for a cryostat made of Aluminum and Fig. 39 for a Steel cryostat. The cost function identifies the area on which to focus the selection of the key design parameters. In the (desirable) deep blue area (inside the smallest circular contour lines) the cost function is rather shallow and, consequently, the region for selecting the design parameters is reasonably large. In the dark color region, one of the mass or geometrical constraints has been violated and consequently the penalty functions bound the *design area*. Note that the maximum capsule mass limits the *design area* on the right-hand side of the plots while the (critical) cryostat mass and the maximum external diameter of the capsule limit the *design area* on the left side of the plots. In the Steel-cryostat case the (critical) cryostat mass is the leading boundary condition on the left side of the *design area*. In the lower side of the plot, the *design area* is limited by the minimum free fall time that has been set equal to 15 s in order to allow for a reasonable numbers of signal cycles.

65
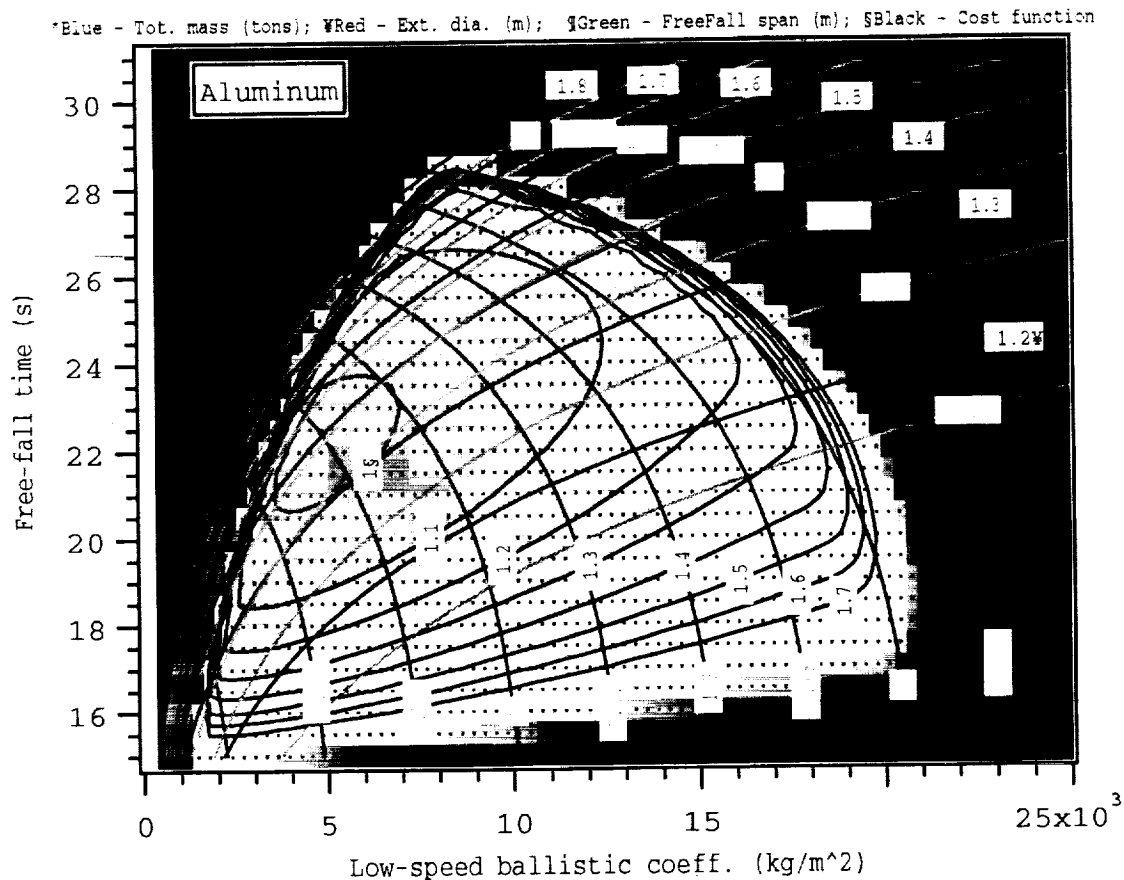
Figure 41 Cost function in the capsule parameter space (Aluminum cryostat)

The figures show that an external diameter in the neighborhood of 1.4 m is a valid selection for the capsule based on the assumptions of this analysis. The 1.4-m diameter contour line cuts across the region of the minimum value of the cost function. Furthermore, the minimum-value region is larger for an Aluminum cryostat than for a Steel cryostat because in the latter case the boundary of the minimum (and critical) cryostat mass encroaches into the low-valued area of the cost function. Consequently, Aluminum is preferable to Steel as it allows wider margins to work with in the capsule design. After focusing on Figure 41, an "optimal" design choice could be an external capsule diameter of 1.4 m (with an overall capsule length of 5.6 m). The overall capsule mass could start at a minimum value of about a 1000 kg which provides a free fall time of 23.5 s. Note from the figures that the free-fall span contour line is about parallel to the 1.4-m external diameter line. This situation implies that we could move the design point along those two lines by increasing (with ballast) the capsule mass and increasing the free-fall time. Consequently, a cryostat of given length (see eqn. (49)) can provide longer free fall times by simply making the capsule heavier with ballast. The free-fall time can be increased by 1 s for every 250-kg ballast (or other equipment) added to the capsule up to the point where the upper mass limit is reached. The low-speed ballistic coefficient β_0 of the capsule will vary from about 6500 kg/m^2 for a capsule mass = 1000 kg to 13,000 kg/m^2 for a capsule mass of 2000 kg.
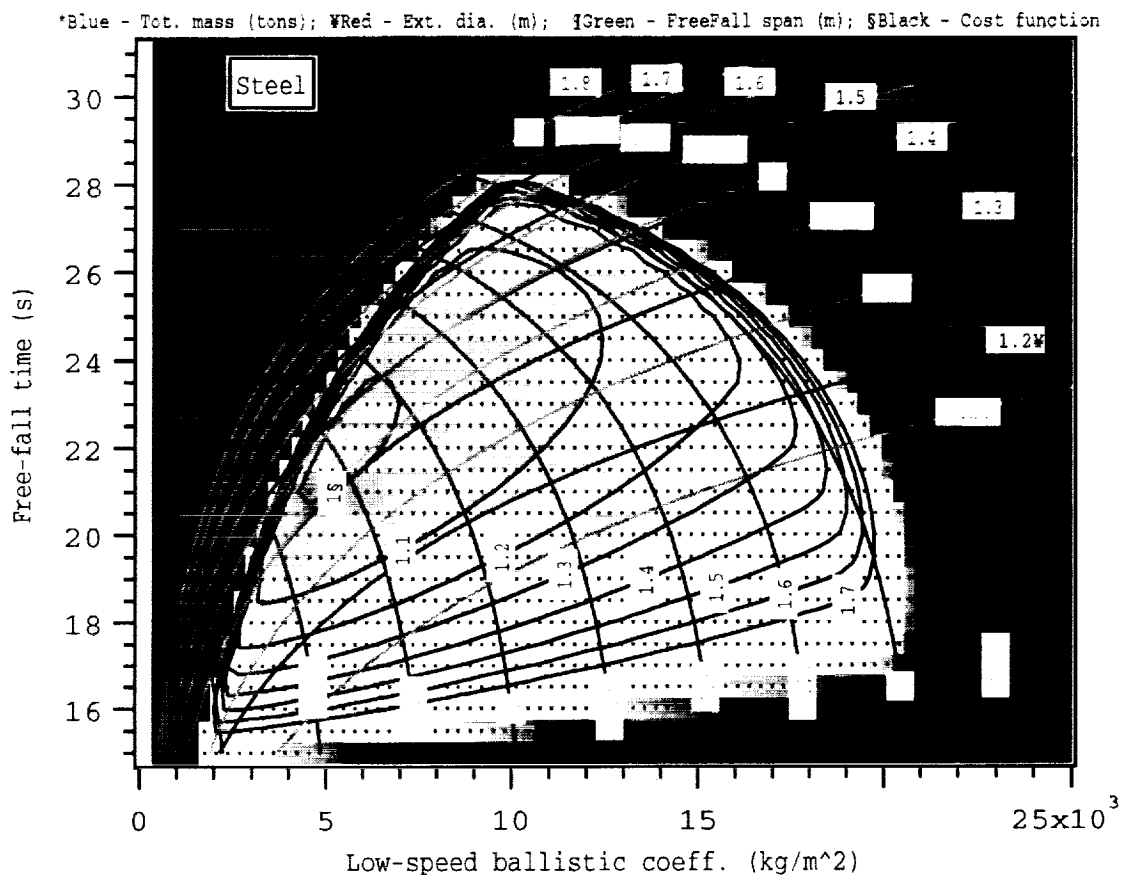
Figure 42 Cost function in the capsule parameter space (Steel cryostat)

This "design concept" optimization does not intend to exhaust the design option for the capsule which will have to be revisited many times before the design is frozen based on additional system analyses. However, this process is a valid starting point to provide preliminary numbers for the analysis to be conducted by our cryostat subcontractor Janis Research. The optimization process also provides a framework that lends itself to future refinements for evaluating system design parameters vis a vis performance input requirements and engineering constraints.

REQUIREMENTS DEVELOPMENT

Table 1 Development of Requirements vs. Design Drivers (version #1)

Design Driver	Science-originated Reqmt.	Engineering Requirements		
	Tolerable differential acceleration	Detector/ Package	Cryostat	Drop System
Free-fall (time > 20 s)	N/A	Transient damping time < 5 s	Limit LHe sloshing in 0 g	$\beta_0 > 5000$ kg/m^2
Amplifier noise (white)	$< 6 \times 10^{-15}$ g/$\sqrt{Hz}$	Preamp. $T_N < 60$ mK proof mass > 5kg	N/A	N/A
Brownian noise (white)	$< 6 \times 10^{-15}$ g/$\sqrt{Hz}$	$\omega_0/Q < 2\pi/10^5$ rad/s T < 10 K	LHe cryostat High-Q proof masses	N/A
Viscous drag on proof masses (dc)	$< 10^{-12}$ g	$p_d < 10^{-9}$ mBar	N/A	N/A
Temperature gradients [Radiometer effect, (ω)]	$< 5 \times 10^{-16}$ g	$\Delta T/\Delta x < 0.1$ K/m	T uniformity inside cryostat	N/A
Acceleration noise inside capsule in free fall	$< 10^{-12}$ g	CMRF $< 10^{-4}$	$p_c < 10^{-6}$ mBar	Structural and attitude freqs. >> ω
Earth's gravity gradients	$< 10^{-12}$ g (2ω) $< 10^{-15}$ g (ω)	Requires centering of proof masses (δ_x) along spin axis	N/A	Verticality before release $\delta_x\phi < 0.1$ μm-deg
Cryostat's gravity gradients (distributed mass)	$< 10^{-12}$ g (2ω) $< 10^{-16}$ g (ω)	Centering of proof masses within 10 μm	Cryostat internal dia. > 1 m	N/A
Gravity gradients of lump masses on board capsule	$< 10^{-12}$ g (2ω) $< 10^{-16}$ g (ω)	Centering of proof masses within 10 μm	N/A	Mass-distance exclusion zones (see Fig. 33)
Magnetic disturbances	$< 10^{-16}$ g	Use Niobium alloy blanket around detector. Degauss proof masses	Temperature of package T < Tc (T_c = critical temperature)	Limit magnetic moments outside sensor package $M_m < $ TBD A-m^2 and r > TBD m
Higher-order mass moments	$< 10^{-16}$ g	Evaluate reqm. on cylindrical symmetry of sensing masses	Evaluate effect of distributed mass of cryostat	N/A
Centrifugal gradients due to skewed rotation axis	$< 10^{-15}$ g	Evaluate reqm. on centering of proof masses	N/A	Evaluate reqmts. on leveling and release mechanisms

ω = signal angular frequency; ω_0 = detector resonant angular frequency

Table 1 shows key requirements of major subsystems that have been identified thus far or that will be evaluated during the next year research activity. Table 1 is a work in progress (presently version #1) which will evolve over the duration of the definition study.

UPDATED REFERENCE CONFIGURATION

One of the important results of the analysis carried out is that the small vacuum chamber at the top of the capsule has been eliminated in favor of a fully cryogenic vacuum chamber (see Fig. 43). The new solution eliminates the problem of the gravity gradient produced by the small cryostat in the proximity of the detector and also provides more clearance to the instrument package during the early stage of free fall.
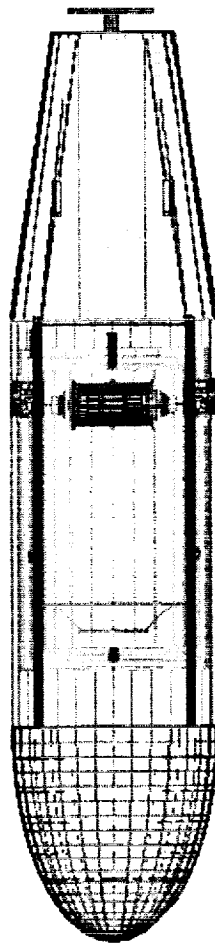
Figure 43 Sketch of new reference configuration of capsule.

The new configuration also has the advantage of using a conventional design of the cryostat rather than a custom made one with doors opening at the bottom as in the previous reference design.

A preferred size of the vacuum chamber has also been identified as a cylinder of 1.2-m diameter and 2.3-m length which results in an external diameter for the capsule of about 1.4 m. Preliminary data on large cryostats (from Janis Research), indicate that the mass of a cryostat of the size considered above will fit well within the mass limit of the system. Such chamber/cryostat will allow free fall times in the range 23-27 s depending on the amount of ballast added to the capsule.

The preliminary results of the thermal analysis also brought changes to the reference design of the instrument package. The preamplifier has been moved close to the sensor and the electronic box is placed farther away from the sensor. These two boxes are mounted on the longitudinal axis of the instrument package (see Fig. 44) instead of placing them on a Saturn-like ring that was more strongly thermally coupled to the sensor. The boxes are thermally weakly linked to one another thanks to thermal shields, interposed among them, which through radiation reduce the heat exchanges. The preamplifier and electronic boxes are mirrored on the opposite side of the sensor by equal-mass dummy boxes for dynamic balancing.
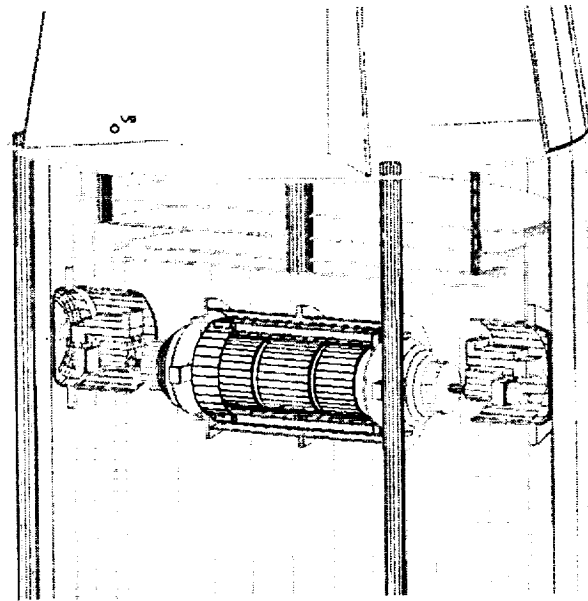
Figure 44 Schematic of instrument package with sensor cut up and electronic boxes.

The reference design will evolve as more analysis is conducted on a number of issues that can potentially affect the system conceptual design and ultimately the experiment performance. The last section of this report summarizes critical areas to be investigated during the next year of activity on this project.

THEORETICAL IMPACTS

Contribution of Parity Non-conserving Weak Interactions

Introduction

A theoretical question that we sought to address can be simply stated: What is the contribution to the mass-energy of each material due to the parity non conserving part of the weak interaction? The reason that we sought an answer to this question was to find out if our experiment would be sensitive enough to determine whether or not this contribution obeys the weak principle of equivalence.

Unfortunately, the present level of development of physics does not allow us to address our question reliably. Knowledge of the physics of nuclear matter is too primitive. We have therefore had to make a number of "reasonable," but nonetheless somewhat arbitrary, assumptions to carry out the calculations. The discussion below mentions each of these assumptions. The results of the calculations indicate that our experiment will not be sensitive to the contribution to mass-energy of the parity non conserving part of the weak interaction.

Evaluation of contribution

The materials to be compared in the experiment should have binding energies stored in forms which are as different as possible. For example, if gravity couples differently to protons and neutrons, we should compare elements with different proton to neutron ratios. A new long range force could also be detected by comparing such elements. A force coupling to baryon number would cause an acceleration proportional to the total number of protons and neutrons divided by the mass, or for a single nucleus, to

$(Z+N)/(m_p Z + m_n N) \sim 1/m_N(1 - \dfrac{(m_p - m_n)}{m_N} x)$. Here x is the ratio Z/A and Z, N and A are

the number of protons, neutrons, and combined nucleons. The mass m_N is used for the common mass of protons and neutrons. In order to observe this effect, it is best to compare heavy elements with $x \sim 1/3$ to light elements with $x \sim 1/2$.

As we will see below, the energy of a nucleus can depend very sensitively on the wave functions of the protons and neutrons. We will discuss a force coupling to the product of proton and neutron densities. Such a force is more significant for nuclei in which proton and neutron wave functions have greater overlaps. This suggests choosing a nucleus with a magic number to compare to a less stable nucleus. The filled shell structure of a nucleus with a magic number may imply greater overlap of the wave functions of the protons and neutrons.

Suppose gravity couples differently to the energy produced by the parity violating part of the weak force. We must calculate what fraction of a nucleus's energy is stored in this form, although we will see that it is not very well defined. First of all, right-handed neutrinos do not appear to exist, so it is not just the weak force which violates parity. The model used in Ref [xxiv] to calculate the total weak force energy of a nucleus is a current-current interaction. To discuss this, let us consider the Lagrangian for the interaction of the weak force with quarks and leptons. Schematically, it is $A_\mu(J_5^\mu + J^\mu)$, where J and J_5 are the weak vector and axial currents, and A is the field of the weak force. (This expression must be summed over the three types of W particles; this formula ignores the fact that the observed W and Z particles are actually linear combinations of these three fields with a fourth field.) By including both terms, we ensure that the coupling to right-handed particles cancels. The first term here is the parity violating term. However, if we use a contact interaction, taking into account the large mass of the W particles, we find an interaction of the form $L_{eff} = (J_\mu + J_\mu^5)(J^\mu + J^{5\mu})$. Multiplying this out, we get four terms—only the terms coupling the axial current to the vector current seem to violate parity in this description of the weak force. Another difficulty is that the separate vector and axial currents are not actually well defined if right-handed neutrinos do not exist.

Since the parity conserving parts of L_{eff} contribute one part in 10^8 to the mass of a nucleus, current limits imply that gravity's coupling to these terms must differ by less than 10^{-4} from its coupling to other matter. The parity violating terms of L_{eff} contribute much less to the mass of a nucleus. If |i> is the state of the nucleus with weak forces neglect, then the first order perturbation of its energy due to these terms is $<i|J^\mu J_\mu^5|i>$, which vanishes by symmetry. (|i> is a parity eigenstate, so the operator changes its parity, and gives a state orthogonal to <i|.) This ensures that the contribution of the parity violating terms is second order in perturbation theory, and therefore small enough to be unconstrained by previous experiments. However, L_{eff} is only useful for calculations. It would be strange for gravity to couple differently to the parity violating part of the weak force unless it coupled differently to $J_\mu^5 A^\mu$ in the original Lagrangian. In this case $J_\mu^5 J^{5\mu}$ would also couple differently to gravity, and this would be a much larger effect.

While we are deciding which terms of the effective Lagrangian will be considered to be parity violating, we should notice that there are other parity violating interactions involving pion exchange[xxv,xxvi]. Ref. xxiv probably overestimated the contribution of $J_\mu J^\mu$ to the weak energy of a nucleus, because of the assumption that the nucleons are distributed independently of one another in a nucleus. In fact, protons and neutrons are generally not closer to one another than their radius of 10^{-15} m, or $(160 \text{ MeV})^{-1}$ as compared to the range 1 GeV^{-1} of the weak force. Thus, the weak interaction of nucleons occurs only very rarely. The pion exchange force has a range larger than the size of a nucleon, so the assumption that nucleons are independently distributed is more accurate when considering this force.

The interaction between nucleons and pions is described by the Lagrangian

$$L_{int} = -ig_{\pi NN} \, \overline{N}\gamma_5\vec{\tau} \cdot \vec{\pi}N - \tfrac{i}{2}f_\pi \, \overline{N}(\vec{\tau}\times\vec{\pi})_3 N$$

(Ref xxv) where we have used isospin notation, so that N is an isospinor of proton and neutron fields: $N = \begin{pmatrix} p \\ n \end{pmatrix}$, $\vec{\tau}$ is a vector of three Pauli matrices, and $\vec{\pi}$ is the vector of pion fields, which are usually written as $(\dfrac{\pi^+ + \pi^-}{\sqrt{2}}, i\dfrac{\pi^+ - \pi^-}{\sqrt{2}}, \pi^0)$. The first term in the Lagrangian represents pion exchange due to the strong force ($g_{\pi NN} = 13.45$), the second to the weak force ($f_\pi = 4.54\times10^{-7}$). This term violates parity. We will calculate contributions to the energy of a nucleus arising from this term.

Any interaction in which a light particle like the pion is exchanged can be approximated by interaction potentials. For example, we begin with a simplified model of spin zero protons and neutrons which can exchange a neutral spin 0 pion (of mass m_π). Let the interaction Hamiltonian be $g(n^\dagger n + p^\dagger p)\pi$. Then the amplitude for pion emission is $-ig$. Let us calculate the potential acting between protons and neutrons. The Feynman diagram is:
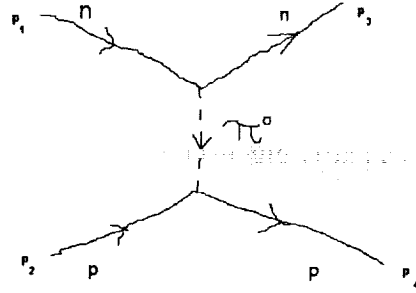
The amplitude associated with this is $A = \tfrac{1}{i}(-ig)^2 \dfrac{i}{q^2 - m_\pi^2} \approx \dfrac{g^2}{\vec{q}^2 + m_\pi^2}$. We have omitted the time-like component of q, since this is the energy transferred between the nucleons, and is small compared to the momentum in the non-relativistic limit.

Compare this to the calculation of scattering under the influence of a potential V. Let the initial and final states be $|\psi_i> = \dfrac{e^{i(\vec{p}_1\cdot\vec{r}_n + \vec{p}_2\cdot\vec{r}_p)}}{(2\pi)^3}$ and $|\psi_f> = \dfrac{e^{i(\vec{p}_3\cdot\vec{r}_n + \vec{p}_4\cdot\vec{r}_p)}}{(2\pi)^3}$. In time independent perturbation theory, we solve for the coefficient

$$c_f = <f|T(-\infty,t)|i> \approx \int_{-\infty}^{t} <f|V|i> e^{i(E_f - E_i)t'}dt' \xrightarrow{t\to\infty} V_{fi} 2\pi\delta(E_f - E_i) \,.$$

It is not hard to check that $V_{fi} = \tfrac{1}{(2\pi)^3}\delta(\vec{p}_1 + \vec{p}_2 - \vec{p}_3 - \vec{p}_4)\int d^3\vec{x} V(\vec{x})e^{i\vec{q}\cdot\vec{x}}$.

73

The Feynman amplitude is closely related to this coefficient; however, it is calculated with the wave functions normalized so that $<p_3p_4 \mid p_1p_2> = 4E_1E_2(2\pi)^3\delta(\vec{p}_1 - \vec{p}_3)\delta(\vec{p}_2 - \vec{p}_4) \approx 4m_N^2(2\pi)^6\delta(\vec{p}_1 - \vec{p}_3)\delta(\vec{p}_2 - \vec{p}_4)$. Thus we must multiply our value for c_f by $4m_N^2(2\pi)^6$. The relationship between c_f and A is thus

$$iA(2\pi)^4\delta(E_3 + E_4 - E_1 - E_2)\delta(\vec{p}_1 + \vec{p}_2 - \vec{p}_3 - \vec{p}_4) = 4m_N^2(2\pi)^6 c_f.$$

Therefore

$A = -4m_N^2 i\int V(\vec{x})e^{i\vec{q}\cdot\vec{x}}d^3\vec{x}$, and the inverse Fourier transform of this gives V. We find that $V(\vec{x}) = \dfrac{-g^2 e^{-m_\pi|\vec{x}|}}{(4m_N^2)4\pi \mid \vec{x} \mid}$, where the transform is evaluated using spherical coordinates. This is the Yukawa potential, but it is not actually the true interaction potential of the protons and neutrons, since protons and neutrons really have spin 1/2, and have axial couplings to the pions.

Expanding the Hamiltonian given above, we find the parity conserving and parity violating pion-nucleon interactions

$$H_{PC} = ig_{\pi NN}\int d^3\vec{x}(\overline{p}\gamma_5 p - \overline{n}\gamma_5 n)\pi^0 + \sqrt{2}(\overline{p}\gamma_5 n\pi^+ + \overline{n}\gamma_5 p\pi^-)$$

and

$$H_{PV} = \frac{if_\pi}{\sqrt{2}}\int d^3\vec{x}\,\overline{p}n\pi^+ - \overline{n}p\pi^-.$$

The π's are pseudoscalar particles and $\overline{p}\gamma_5 p$ and similar terms are scalars, and so it is the first of these interactions which is parity conserving. This is actually a convention, since if the second interaction had been discovered first, the pions would have been called scalar particles. A consequence is that an interaction between nucleons by exchange of pions is equivalent to a parity conserving potential as long as both pion-nucleon vertices are governed by the same interaction. If the pion is emitted according to the parity conserving interaction and absorbed according to the parity violating interaction, then the equivalent potential distinguishes between left and right. We call the three potentials

$V_{PCPC}, V_{PVPV}, V_{PVPC}$, where the subscripts indicate the nature of the pion exchanges (parity violating or parity conserving).
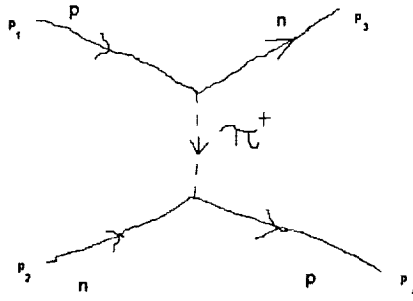
Since the PVPV interaction is mediated only by charged pions, the only possible interaction is the above. The proton turns into a neutron when it emits the π^+ in order to conserve charge. The calculation of the potential associated with this interaction is very similar to the calculation above for the simplified model. There are two differences. First, the extra factors proportional to the mass which arise from normalization conventions do not occur for spinors. Second, since the proton and neutron have two spin states, we must determine how the interactions affect their spins. Since the pions are spinless, a nucleon's spin does not flip when it emits a pion. Thus if the proton initially has spin up and the neutron is spin down, then the scattered proton has spin down and the scattered neutron has spin up. The effective potential for this interaction is

$$V(\vec{r}_1 - \vec{r}_2) = \frac{f_\pi^2}{2} \frac{e^{-m_\pi|\vec{r}_1 - \vec{r}_2|}}{4\pi |\vec{r}_1 - \vec{r}_2|} X , \text{ where X is an operator which turns protons into neutrons}$$

and neutrons into protons.

Since particles can change types, we will use second quantization. The operator $n_\uparrow^+(\vec{r}_1)p_\uparrow(\vec{r}_1) + n_\downarrow^+(\vec{r}_1)p_\downarrow(\vec{r}_1)$ turns a proton at point r_1 into a neutron at the same point with the same spin. So the operator X is equal to $[p_\uparrow^+(\vec{r}_1)n_\uparrow(\vec{r}_1) + p_\downarrow^+(\vec{r}_1)n_\downarrow(\vec{r}_1)][n_\uparrow^+(\vec{r}_2)p_\uparrow(\vec{r}_2) + n_\downarrow^+(\vec{r}_2)p_\downarrow(\vec{r}_2)]$.

The interaction Hamiltonian is therefore

$$H_{PVPV} = -\iint d^3\vec{r}_1 d^3\vec{r}_2 \frac{f_\pi^2}{8\pi} \frac{e^{-m_\pi|\vec{r}_1 - \vec{r}_2|}}{|\vec{r}_1 - \vec{r}_2|} [p_\uparrow^+(\vec{r}_1)n_\uparrow(\vec{r}_1) + p_\downarrow^+(\vec{r}_1)n_\downarrow(\vec{r}_1)][n_\uparrow^+(\vec{r}_2)p_\uparrow(\vec{r}_2) + n_\downarrow^+(\vec{r}_2)p_\downarrow(\vec{r}_2)].$$

This interaction does not seem to mediate a force between two separated nucleons, since the nucleons can't retain their identity. In particular, it cannot mediate a force between two separate nuclei, even though it does contribute to the binding energy of a single nucleus. Suppose the nucleus can be modeled as consisting of two Fermi seas, one of protons and one of neutrons. (Of course H_{PCPC}, which is much larger than any parity violating interactions, produces correlations in nuclei.) There are protons of both spins and of every momentum less than k_p, and there are neutrons up to k_n. We will assume the nucleus is very large so that we can approximate the waves by plane waves, and we will calculate the energy density due to H_{PVPV}. Then since the proton and

75

neutron which interact are in the same nucleus, the interaction does not change the nucleus type.

The energy shift is $<i| H_{p\nu p\nu} |i>$. Consider the action of $H_{p\nu p\nu}$ on the Fermi sea. It acts on two particles—a proton of momentum $\vec{k}_1$ and a neutron of momentum $\vec{k}_2$, changing their momentum and interchanging their particle types. Since the resulting state is multiplied by $<i|$, it must have the same occupied states as $|i>$ in order to give a nonzero contribution to the energy. Thus the final proton must have the same momentum as the initial proton, as in the following diagram:
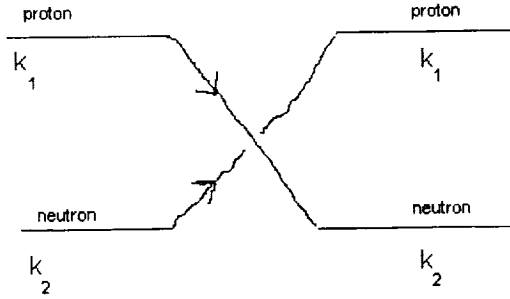
Also, the particles must have the same spin, since the interaction does not flip spin.

In order to see at least one failure of our approximations, we consider two general wave functions for a proton and neutron and calculate their interaction in these states. We ignore the spin wave function, and set

$$| \psi >= \tfrac{1}{\sqrt{2}}(f_1(\vec{r}_1)f_2(\vec{r}_2) | pn > - f_2(\vec{r}_1)f_1(\vec{r}_2) | np >).$$

The wave function here is antisymmetric in space and isospin, according to the Pauli exclusion principle for multiple types of fermions. Thus neither $\vec{r}_1$ nor $\vec{r}_2$ is the coordinate of the proton. But f_1 must be the wave function of the proton. Assuming both spins are up,

$$H_{p\nu p\nu} | \psi >= -\tfrac{f_\pi^2}{2\sqrt{2}}\iint V(\vec{x}_1 - \vec{x}_2)d^3\vec{x}_1 d^3\vec{x}_2 p_\uparrow^\dagger(\vec{x}_1)n_\uparrow(\vec{x}_1)n_\uparrow^\dagger(\vec{x}_2)p_\uparrow(\vec{x}_2)[f_1(\vec{r}_1)f_2(\vec{r}_2) | pn > - f_2(\vec{r}_1)f_1(\vec{r}_2) | np >]$$

$$= -\tfrac{f_\pi^2}{2\sqrt{2}}[V(\vec{r}_2 - \vec{r}_1)f_1(\vec{r}_1)f_2(\vec{r}_2) | np > - V(\vec{r}_1 - \vec{r}_2)f_2(\vec{r}_1)f_1(\vec{r}_2) | pn >].$$

In evaluating the integrals, we must choose $\vec{x}_1$ and $\vec{x}_2$ to coincide with $\vec{r}_1$ and $\vec{r}_2$ in one order, so that $\vec{x}_1$ represents the location of the initial neutron. Now, noticing that $<pn|pn>=<np|np>=1$ while $<pn|np>=<np|pn>=0$, we obtain

$$< \psi | H_{p\nu p\nu} | \psi >= \tfrac{f_\pi^2}{4}\iint d^3\vec{r}_1 d^3\vec{r}_2 V(\vec{r}_1 - \vec{r}_2)[f_1(\vec{r}_1)^* f_2(\vec{r}_2)^* f_2(\vec{r}_1)f_1(\vec{r}_2) + f_2(\vec{r}_1)^* f_1(\vec{r}_2)^* f_1(\vec{r}_1)f_2(\vec{r}_2)]$$

$$= \tfrac{f_\pi^2}{2}\iint d^3\vec{r}_1 d^3\vec{r}_2 V(\vec{r}_1 - \vec{r}_2)f_1(\vec{r}_1)^* f_2(\vec{r}_1)f_1(\vec{r}_2)f_2(\vec{r}_1)^*,$$

where the two terms can be combined by exchanging $\vec{r}_1$ and $\vec{r}_2$ in the second term.

This has the form of an exchange force—notice that if f_1 and f_2 are never nonzero at the same point, then the integrand vanishes. This is why we claimed above that the shell structure might affect the parity violating energy; a simple form with plane wave states ignores all the structure of the nucleus.

In order to find the total energy, we must sum over all occupied proton and neutron states f_1 and f_2 respectively. There is also a self-interaction due to H_{PVPV} in which a nucleon changes type and then changes back. This gives an infinite contribution to the energy, and is also more significant because a particle is certain to be at the same location as itself, so the comment about overlap at the end of the last paragraph doesn't apply. We will discuss self-energy contributions at the end.

Substituting $V(\vec{r}_1 - \vec{r}_2) = \frac{1}{4\pi} \dfrac{e^{-m_\pi |\vec{r}_1 - \vec{r}_2|}}{|\vec{r}_1 - \vec{r}_2|}$ and plane waves which are normalized so that their integral over the volume V of the nucleus is 1, we obtain an energy proportional to the Fourier transform of the Yukawa potential. It is equal to

$$< H_{PVPV} > = \frac{f_\pi^2}{2V} \frac{1}{m_\pi^2 + |\vec{k}_1 - \vec{k}_2|^2} \text{ , and the sum over all pairs of nucleons is}$$

$$\delta E_{PV} = 2 \frac{f_\pi^2}{2V} \sum_{|\vec{k}_1| < k_p} \sum_{|\vec{k}_2| < k_n} \frac{1}{m_\pi^2 + |\vec{k}_1 - \vec{k}_2|^2}$$

where the factor of 2 arises because the proton and neutron can be both spin up or both spin down. Converting the sum to an integral in the usual way, we obtain

$$\delta E_{PV} = \frac{f_\pi^2}{V} \left(\frac{V}{(2\pi)^3} \right)^2 \int_{|\vec{k}_1| < k_p} \int_{|\vec{k}_2| < k_n} \frac{d^3\vec{k}_1 d^3\vec{k}_2}{m_\pi^2 + |\vec{k}_1 - \vec{k}_2|^2} .$$

First integrate over $\vec{k}_2$, taking the z-axis along $\vec{k}_1$.

$$\int d^3\vec{k}_2 \frac{1}{m_\pi^2 + |\vec{k}_1 - \vec{k}_2|^2} = 2\pi \int_0^{k_n} k_2^2 dk_2 \int_0^\pi \frac{\sin\theta d\theta}{m_\pi^2 + k_1^2 + k_2^2 - 2k_1 k_2 \cos\theta}$$

$$= 2\pi \int_0^{k_n} k_2^2 dk_2 \frac{\ln(m_\pi^2 + k_1^2 + k_2^2 - 2k_1 k_2 \cos\theta)}{2k_1 k_2} \Big|_0^\pi$$

$$= \pi \int_0^{k_n} \frac{k_2}{k_1} dk_2 \ln\left(\frac{m_\pi^2 + (k_1 + k_2)^2}{m_\pi^2 + (k_1 - k_2)^2} \right)$$

We now integrate over the direction of $\vec{k}_1$, giving a factor of 4π, and then give the expression for the integral:

$$\frac{\delta E_{PV}}{V} = \frac{f_\pi^2}{16\pi^4}\int_0^{k_p}\int_0^{k_n} dk_2 dk_1 k_1 k_2 \ln(\frac{m_\pi^2 + (k_1 + k_2)^2}{m_\pi^2 + (k_1 - k_2)^2})$$

$$= \frac{f_\pi^2}{16\pi^4}\{[-\tfrac{1}{8}(k_p^2 - k_n^2)^2 + \tfrac{1}{4}m_\pi^2(k_p^2 + k_n^2) + \frac{m_\pi^4}{24}]\ln(\frac{m_\pi^2 + (k_1 + k_2)^2}{m_\pi^2 + (k_1 - k_2)^2})$$

$$- \frac{2m_\pi}{3}(k_p^3 + k_n^3)\arctan\frac{k_p + k_n}{m_\pi} + \frac{2m_\pi}{3}(k_p^3 - k_n^3)\arctan\frac{k_p - k_n}{m_\pi}$$

$$- \frac{m_\pi^2 k_p k_n}{6} + \tfrac{1}{2}k_p k_n(k_p^2 + k_n^2)\}$$

The integral is evaluated by repeated integrations by parts.

We would now like to evaluate this expression as a function of x = Z/A. The volume of a nucleus is proportional to A; that is, each nucleon occupies a fixed volume. The volume is given by $\frac{4}{3}\pi r_0^3 A$ where $r_0 = 1.2$ fm[xxvii]. As usual, the Fermi momenta are given by $k_p = (3\pi^2 n_p)^{1/3}$ where n_p is the proton number density, so $k_p = \frac{1}{r_0}\sqrt[3]{\frac{9\pi}{4}x} = 320\sqrt[3]{x}\,MeV$ and similarly $k_n = 320\sqrt[3]{1-x}\,MeV$. Furthermore, the mass of a nucleus is roughly Am_N, so

$$\frac{\delta E_{PV}}{M} = \frac{V}{Am_N}\frac{\delta E_{PV}}{V} = \frac{\frac{4}{3}\pi r_0^3}{m_N}\frac{\delta E_{PV}}{V} = (1.0\times 10^{-9}\,MeV^{-4})\frac{\delta E_{PV}}{V}.$$ (Notice that our estimates, for x = 1/2, give a Fermi momentum of 250 MeV, which is somewhat small compared to the nucleon mass, so our nonrelativistic approximations (in particular, neglecting the time-like component of q in the derivation of the effective interaction) seem reasonable.)

The following figure shows $\frac{\delta E_{PV}}{M}$ as a function of x; it is on the order of 10^{-16} and is almost exactly equal to $\frac{\delta E_{PV}}{M} = 9x(1-x)\times 10^{-16}$, which is much easier to interpret than the formula given above; for a contact force, the number of interactions occurring in the nucleus is proportional to the product of the densities, which is proportional to x(1-x). (The suggested derivation of this formula—assume the mass of the pion is very large and replace the interaction by a contact interaction—gives an incorrect answer, $30x(1-x)\times 10^{-16}$. The mass of the pion is not large enough to regard V_{PV} as a contact interaction.)

$$\frac{\delta E_{PV}}{M} \times 10^{-16}$$

X
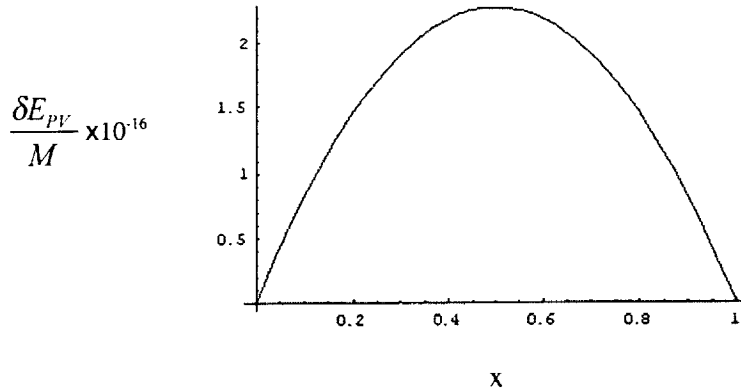
The fraction we have just calculated is very small, and (since we can only compare different nuclei) its variation from nucleus to nucleus is even less--2×10^{-17}, if x varies from 1/2 to 1/3. There are similar smooth empirical formulae for the total mass of a nucleus, but the mass differences are somewhat larger from nucleus to nucleus because the mass depends in a more jagged way on the atomic number. Thus, the plane wave description of the protons and neutrons cannot suggest which nuclei have unusually large or unusually small contributions from the weak force. There are many other contributions to the parity violating energy as well—for example, the interaction V_{PCPV} produces an energy shift at second order in perturbation theory. This can occur only at second order because $<i|\ V_{PCPV}|i>$ vanishes—after all, $|i>$ is a parity eigenstate since the strong forces which determine the structure of the unperturbed nucleus are parity conserving. However, by introducing an intermediate state of opposite parity and very similar energy, one can hope to obtain the largest possible weak parity violating contribution to the energy. For ^{19}F, Ref [xxviii] estimates $\frac{\delta E_{PV}}{M}$ =7×10^{-17}, which is very similar to what we obtained above. Ref. xxviii did not calculate the matrix elements from the theoretical formula for V_{PCPV} but from an experiment mentioned in Ref xxv. The latter reference also calculated the matrix element from a theory based on exchange of pions and other particles, giving a value which was off by only 20%.)

Ref xxviii's calculation did not take the direct exchange of single pions in which both the emitted and absorbed pion have parity violating interactions, leading to an impression that only nuclei with narrowly separated partners of opposite parity have large values of $\frac{\delta E_{PV}}{M}$. However it leads to a very clear case in which one expects a jump in the parity violating energy—choose a nucleus $|i>$ which is close in energy to another nucleus $|i'>$ with the opposite parity. Fluorine is not the only choice. If one were to calculate the matrix element of V_{PCPV} between these states theoretically (the calculation would be similar to the above), one would find that $<i'\ |V_{PCPV}\ |i> \propto volume \propto M$. Thus,

$$\frac{\delta E_{PV}}{M} = \frac{1}{M}\frac{|<i'|V_{PCPV}|i>|^2}{M_i - M_{i'}} \propto \frac{M}{M_i - M_{i'}}$$, where the denominator here is just the energy

denominator (with energy replaced by mass). (M is either of the two masses.) So we expect an especially large parity violating energy if the mass difference of the nucleus and its excited state is small compared to the mass of the nucleus.

Finally, Ref. [xxix] calculates the weak-force self-energy of a proton or neutron and finds that its fractional contribution to the mass of a nucleus is 10 times larger than the energy from the interactions of different protons and neutrons in the nucleus calculated in Ref. xxiv. Most likely, the parity violating self-energy of the protons and neutrons is more significant than anything we have already calculated. This returns to one of the most obvious models for equivalence principle violations—assume that gravity couples differently to protons and neutrons. This gives gravitational mass differences which are linear in x (just as we found in the model of a long range force coupled to the total number of baryons in a nucleus). So a simple approach is to choose nuclei with the largest and smallest possible values of x. (Hydrogen and Uranium are suggested in Ref. [xxx]!)

There are three reasons why it is unlikely that gravity couples differently to the "parity violating part of the weak force." First, this depends on whether one uses the fundamental Lagrangian or the current-current Lagrangian as discussed above. In practice, the definition of the parity violating and parity conserving energies is very technical—a summary of the definition we used is "it is the part of the weak force which is second order in perturbation theory." Second, in the electroweak theory, photons are linear combinations of a W particle and another gauge particle, so if gravity couples differently to the W particles, it probably couples differently to the photon as well. Third, all self-energies are infinite in any case. This is why the self-energy of the protons and neutrons calculated in Ref. xxix is much larger than the energies of the nuclei calculated in Ref. xxiv. The interactions of the quarks inside the protons and neutrons are larger than the interaction energies of different protons and neutrons because the quarks are closer together. If the quarks are point particles, then they contribute infinite self-energies due to the weak force besides these other energies. Fourth, energy cannot be separated into different forms of energies. For example, the energy we calculated above includes the mass of the virtual pions, which is due to the strong force.

KEY AREAS TO BE ANALYZED

Critical issues to be addressed during the next year research activity are as follows:

Detector rotational dynamics after release:

- evaluate effects of rotational acceleration for axis of rotation skewed with respect to the symmetry axis of the sensing masses;

80

- include the effects of gravity gradient field inside capsule and Earth's gravity gradients in the external force model;

- derive dynamics-related requirements for capsule leveling mechanism, release mechanism and centering of sensing masses.

Higher-order mass moments:

- evaluate effects of higher order mass moments due to nearby masses either concentrated or distributed;

- estimate safe distances from non-corotating masses;

- derive requirements on cylindrical symmetry of sensing masses.

Magnetic disturbances:

- revisit the early estimates of magnetic disturbances as a result of changed configuration of instrument package;

- derive requirements of magnetic cleanliness for typical levels of ferromagnetic impurities in the sensing masses.

Thermal analysis:

- evaluate the temperature drifts of sensor and attached equipment before release (when attached to the cryostat);

- refine estimates of temperature variations after release (during the measurement phase) for inter-connected sensor, preamplifier and electronic boxes;

- refine thermal design based on new results;

- derive requirements on optical properties, thermal conductivity, and tolerable energy dissipations and power duty cycle during calibration of detector, preamplifier and electronic units.

Cryostat preliminary design:

- evaluate (through Janis Research) mass properties and cost of large cryostat;

- address issue of Helium containment in zero g;

- refine analyses of gravity gradients if mass distribution of cryostat is substantially different from current estimates.

Sensor release mechanism and capsule leveling mechanism:

- assess requirements resulting from dynamics and gravity gradients analyses and define separate sets of requirements for the release and leveling mechanisms;

- work on conceptual design of sensor release mechanism;

- work on conceptual design of capsule leveling mechanism.

Detector requirements:

- continue working in cooperation with our non-US partners on the definition of detector requirements;

- define, in cooperation with our partners, those laboratory measurements/tests that need to be conducted for completing the set of requirements.

REFERENCES

[i] R.V. EÖTVÖS, Math. u. Naturw. Ber. aus Ungarn Vol. 8, 65 (1890).

[ii] R.V. EÖTVÖS, V. PEKAR AND E. FETEKE, "Beitrage zum Gesetze der Proportionalität von Trägheit und Gravität," *Annalen der Physik*, Vol. 68, 11-66 (1922).

[iii] P.G. ROLL, R. KROTKOV AND R.H. DICKE, *Annals of Physics*, Vol. 26, 442 (1964).

[iv] I.I. SHAPIRO, C.C. COUNSELMAN AND R.W. KING, *Phys. Rev. Lett.* Vol. 36, 555 (1976).

[v] J.G. WILLIAMS ET AL., *Phys. Rev. Lett.* Vol. 36(11), 551 (1976).

[vi] Williams, J.G., X.X. Newhall and J.O. Dickey (1996), Relativity parameters determined from lunar laser ranging, *Phys. Rev. D*, 53, 6730.

[vii] Baessler S., Heckel B., Adelberger, E. Gundlack J., Schmidt U. and Swanson E. (1 Nov. 1999), *Phys Rev Lett.*, Vol. 83.

[viii] Touboul P.,"µScope, Satellite á trainéé Compenséé pour l'Observation du Principe d'Equivalence." ESA-CERN Workshop – Fundamental Physics in Space and Related Topics, 5-7 April 2000.

[ix] Nobili, A.M. et al., "*Galileo Galilei* Flight Experiment on the Equivalence Principle with Field Emission Electric Propulsion." *Journal of the Astronautical Sciences*, Vol. 43, No. 3, 219-242, 1995.

[x] STEP team, "STEP Satellite test of the equivalence principle report on the Phase A study." ESA SCI(96) 5, 1994.

[xi] Lorenzini, E.C., M.L. Cosmo, M.D. Grossi and T. Rothman, "A method for testing the principle of equivalence with improved accuracy." Smithsonian Astrophysical Observatory, Technical Note TP91-001, Cambridge, Massachusetts, 1991.

[xii] Dittus, H., et al., "Testing the weak equivalence principle at the Bremen drop tower: report on recent developments." *Classical And Quantum Gravity*, Vol. 13, No. 11, A43-A51, 1996.

[xiii] Gullahorn, G.E., F. Fuligni and M.D. Grossi, "Gravity gradiometry from the tethered satellite system." *IEEE Trans. On Geoscience and Remote Sensing*, Vol. GE-23, 531-540, 1985.

[xiv] Lockerbie, N.A., X. Xu, A. Veryaskin, "Spherical harmonic representation of the gravitational coupling between a truncated sector of a hollow cylinder and an arbitrary gravitational source: Relevance to the STEP experiment." *Classical and Quantum Gravity*, Vol. 27, No. 11, 1215-1229, 1995.

[xv] Lazarevich, A. et al., "Balloon-borne, high altitude gravimetry: the flight of Ducky Ia." Report AFGL-TR-0342, Air Force Geophysics Laboratory, Hanscom AFB, MA, 1985.

[xvi] Lorenzini, E.C., I.I. Shapiro, F. Fuligni, V. Iafolla, M.L. Cosmo, M.D. Grossi, P.N. Cheimets and J.B. Zielinski, "Test of the Weak-Equivalence Principle in an Einstein Elevator." Il Nuovo Cimento, Vol. 109B, No. 11, 1994.

[xvii] Kretzschmar, Mikroba unpublished acceleration data, 1999.

[xviii] Staff of John Hopkins University APL and Staff of Stanford University, "A Satellite Freed of all but Gravitational Forces: "TRIAD I". J. Spacecraft, Vol. 11, No.9, (1974).

[xix] Braginsky, V.B. and A.B. Manukin, "Measurement of Weak Forces in Physics Experiments." The University of Chicago Press, p. 7, 1974,.

[xx] Giffard, R.P., *Phys. Rev. D* 14, 2478, 1976.

[xxi] Iafolla, V., A. Mandiello and S. Nozzoli, "The High Sensitivity Italian Spring Accelerometer (ISA) for Fundamental Physics in Space" Advances in Space Research, Vol. 25, No. 6, 1241-1244, 2000.

[xxii] P.W. WORDEN JR, C.W.F. EVERITT AND M. BYE, "Satellite Test of the Equivalence Principle." Stanford University Report (Palo Alto, California, 1990).

[xxiii] F.J. LAVOIE (Editor), "Materials Engineering: *Materials Selector 1987*." Penton Publication, p. 72 (1986).

[xxiv] Haugan, Mark P. and Clifford M. Will. "Weak Interactions and Eötvös Experiments," Phys. Rev. Lett. 37, 1 (1976).

[xxv] Adelberger, E.G. and W.C. Haxton. "Parity Violation in the Nucleon-Nucleon Interaction," Ann. Rev. Nucl. Part. Sci. 35 (1985).

[xxvi] Desplanques, B., J. F. Donoghue, B.R. Holstein. Ann. Phys. 124, 449 (1980).

[xxvii] Bethe, H.A. and P. Morrison. Elementary Nuclear Theory, New York: Wiley (1956).

[xxviii] Haugan, Mark P., Ephraim Fischbach, and Dubravko Tadic. "The Equivalence Principle and Weak Interactions," 1993 STEP symposium.

[xxix] Chamoun, N. and H. Vucetich, "Weak Interactions Effect on the P-N Mass Splitting and the Principle of Equivalence," hep-ph/9909384.

[xxx] Damour, T. and A.M. Polyakov, "The String Dilaton and a Least Coupling Principle," Nuclear Phys. B423 (1994).